TÉCNICO LISBOA

Radiation sensors based on GaN microwires

Dirkjan Verheij

Thesis to obtain the Master of Science Degree in

Engineering Physics

Supervisors: Dr. Katharina Lorenz
Prof. Dr. Susana Isabel Pinheiro Cardoso de Freitas

Examination Committee

Chairperson: Prof. Dr. Pedro Miguel Félix Brogueira
Supervisor: Dr. Katharina Lorenz
Members of the Committee: Dr. Marco António Baptista Peres

November 2017

Acknowledgments

I want to thank everyone that contributed to this investigation. The process engineers at INESC-MN for their availability and patience to assist me with the fabrication process, Dr. Joël Eymery, who kindly offered me the microwires that were used in this work, Prof. Teresa Monteiro and Dr. Nabiha Ben Sedrine who shared their SEM and PLE data with me and finally Dr. Luís Cerqueira Alves for greatly helping me with the irradiation of the devices and providing valuable suggestions.

A big thank you goes out to all the people from the Physics building at CTN who were always very kind to me and make working there an honest pleasure. An honourable mention is in place for the lunch crew.

I also want to thank Professor Susana Freitas, firstly for raising my interest in Nanotechnology through the various courses she gave me during my degree and, secondly, for the opportunity she provided for me to work in this area.

These acknowledgements would certainly not be complete without mentioning my parents, brothers and sisters. Thank you for being such an amazing family. Regarding the unofficial family, I would just like to say that, wherever the future leads each one of us, I am certain that "*O turno*" will never cease to exist. Thank you for making the last five years unforgettable.

Finally, I am especially grateful towards Dr. Katharina Lorenz and Dr. Marco Peres, without whom the conclusion of this thesis would not have been possible. Thank you for all your knowledge, suggestions, fruitful discussions, motivation and overall help during the last year. I truly consider myself a lucky person for having the opportunity to work under your guidance.

I would also like to gratefully acknowledge the financial support given by FCT Portugal and IPFN (UID/FIS/50010/2013).

Resumo

Microfios de GaN, crescidos por deposição de organometálicos em fase de vapor por processo químico (MOCVD), com diâmetros entre 1 e 2 μm, foram usados para desenvolver sensores de radiação através da deposição de contactos metálicos nas suas extremidades por fotolitografia. Os parâmetros chave para analisar são o ganho, o tempo de resposta e o tempo de decaimento dos sensores. Como o GaN tem um hiato energético de 3.4 eV, espera-se um ganho baixo para radiação com $\lambda > 365$nm e um ganho alto para radiação mais energética. Neste sentido, o comportamento da fotocorrente foi estudada sobre iluminação vísivel e ultravioleta e sobre irradiação com protões. Os dispositivos fabricados demonstraram deteção de luz ultravioleta e tempos de decaimento inferiores a 10 segundos foram obtidos. No entanto, o ganho obtido para a fotocorrente foi baixo ($<$20%). A irradiação com protões causou uma significante degradação dos dispositivos mas os resultados confirmaram o seu potencial como detector de protões. Comparativamente aos resultados obtidos com excitação ultravioleta, valores semelhantes para o tempo de decaimento e superiores para o ganho foram obtidos. Medidas de fotocondutividade após a irradiação revelaram, em geral, uma melhoria nas capacidades de deteção de luz ultravioleta por parte dos sensores. Os factores de ganho aumentaram para cerca de duas vezes o valor obtido antes da irradiação e alguma mitigaçao da fotocorrente persistente foi observada. Os resultados indicam a possibilidade de aplicar microfios de GaN não só em detectores de radiação ultravioleta, mas também em detectores de partículas.

Palavras-chave

GaN; Microfios; Sensores de radiação; Fotocondutividade; Irradiação com protões

Abstract

GaN microwires, grown by Metal Organic Chemical Vapour Deposition (MOCVD) and with diameters between 1 and 2 μm, were used to fabricate radiation sensors by electrically connecting their extremities using photolithography. The most important parameters to analyse are the gain, the response time and decay time of the sensors. As GaN has a bandgap of 3.4 eV a very low gain for radiation with $\lambda > 365$ nm is expected and a high gain for more energetic radiation. The photocurrent behaviour of single wire sensors were studied under visible and UV illumination and under irradiation with protons. The fabricated devices demonstrated proper UV detection and decay times below 10 seconds were measured. However underwhelming photocurrent gain factors ($<$20%) were achieved. The irradiation with protons caused a significant degradation of the devices but the results confirmed their potential as particle detectors, as similar decay times and higher gain factors were achieved in comparison with the UV detection. Photoconductivity measurements after the irradiation resulted in an overall improvement of the devices regarding their response to UV radiation. The photocurrent gain factors increased to approximately twice the value that was obtained prior to the irradiation and some quenching of the persistent photocurrent, *i.e.*, improved decay times, was observed. The results indicate the possibility of using GaN microwires not only as UV detectors, but also as a particle detectors.

Keywords

GaN; Microwires; Radiation sensors; Photoconductivity; Proton irradiation

Contents

1 Introduction **1**

1.1 Motivation and Background . . . 3

1.2 Objectives . . . 6

1.3 Outline . . . 6

2 Theoretical Background **7**

2.1 Gallium Nitride properties . . . 9

2.2 Metal-semiconductor-Metal configuration . . . 11

2.2.1 Metal-semiconductor junction . . . 11

2.2.2 Back-to-back Schottky contacts . . . 14

2.2.3 MSM photodetectors . . . 18

2.3 Effects of ionising radiation on GaN . . . 19

3 Growth and fabrication process **23**

3.1 Microwire growth . . . 25

3.2 Fabrication . . . 28

3.3 Characterization methods . . . 35

3.4 Proton-irradiation . . . 39

4 Experimental Results **43**

4.1 Electrical characterization . . . 45

4.2 Photoconductivity . . . 49

4.2.1 Spectroscopy (PCS) . . . 49

4.2.2 I-V characterization . . . 52

4.2.3 Transient I-V characterization . . . 55

4.3 Proton-irradiation . . . 57

4.3.1 Proton-irradiation effects on photoconductivity . . . 62

5 Conclusion **67**

A Runsheet **83**

B Summary of the results for samples 210U, 216U and 229U 89

List of Figures

2.1 Band (right) and crystal (left) structure for Wurtzite GaN. The subscripts in the left graphic denote the two non-equivalent positions for each site. [32, 36] 10

2.2 Energy band diagrams of an individual metal and semiconductor and of the possible junctions. $q\phi_m$, $q\phi_{sc}$, $q\chi$, $q\phi_n$ represent respectively the metal work function, the semiconductor work function, the electron affinity and the difference between the conduction band and the Fermi energy. After contact, $q\phi_{b0}$ is the Schottky barrier height, V_{bi} the built-in voltage and W the depletion width. 11

2.3 Energy band diagram for a metal-semiconductor junction with n^+ doping 14

2.4 Energy band diagrams for a typical MSM structure under zero bias (left) and with a positive bias applied on the right contact (right) 15

2.5 Equivalent circuit of an MSM photodetector 16

2.6 Different transport mechanisms that can occur at a metal-semiconductor contact; The left diagram corresponds to forward bias and the right diagram corresponds to reverse bias [49] 17

3.1 SEM images obtained at two different amplification with a substrate tilt of 47°; The amplification on the left hand side is 500× and the amplification on the right hand side is 2830× 27

3.2 X-ray diffraction data for bulk GaN (blue line) and GaN microwires (orange line) with the standard θ-2θ geometry; The left graph corresponds to the 002 reflection, the middle graph to the 004 reflection and the right graph to the 006 reflection 27

3.3 Schematic of the fabrication process of the radiation sensors. The dimension are not scaled and the figures are only an indication of the structure. 29

3.4 AutoCAD drawing for the definition of the microscaled grid 31

3.5 The grid viewed in an optical miscroscope with an 20× amplification. The dimensions of the sides of each square as well as the spaces between each square are 10 μm 32

3.6 Resultant microwire deposition done mechanically (left photo) and by chemical dispersion (right photo) 33

3.7 AutoCAD drawing for the definition of the contact paths 34

3.8 Optical microscopy images of devices after the lift-off processes. In some cases the fabrication process was successful (left image) while in others, the wire got removed by the ultrasound treatment (middle image) or the contacts are slightly misaligned (right images). 35

3.9 The final device integrated on a chip after dicing and wire bonding. 36

3.10 The initial current peak that appears when initializing an I-V measurement for the 210U (left), the 216U (center) and the 229U (right) devices. It takes approximately two minutes for the current to stabilize. 38

3.11 PIXE elemental maps for Au (left and center) and Ga (right). The alignment of the beam can be done by locating the microwires and selecting the area, represented by the green rectangle, that we want to irradiate. 40

3.12 The obtained results for a SRIM simulation with 2 MeV H^+ protons hitting a planar GaN target of thickness equal to 50 μm. The top left graph shows the path for a number of protons that enter the GaN. The top right graph plots the concentration of hydrogen atoms versus the target depth. The bottom left graph shows the energy loss due to ionization versus the target depth. The bottom right graph shows how many displacements occur versus target depth. 41

4.1 Experimental I-V characteristics obtained when applying a bias from -5V to 5V with a current compliance of 500 μA. The blue circles correspond to the experimental data and the red lines correspond to the fit results. 46

4.2 Voltage drops at the lower Schottky barrier (V_1), the higher Schottky barrier (V_2) and the microwire (V_{mw}) as calculated by the program (right graph) for the fit corresponding to sample 216U (left graph). As can be seen, for positive and high bias, the voltage drop in the microwire dominates and is approximately linear, which tells us that it is mostly dependent on R_{mw} 48

4.3 The photoconductivity spectrum obtained with a 4V bias for the 111U device. The red dotted line represents the fit of the linear region in the absorption and the black dotted line represents the reported bandgap of 3.4 eV The spectrum has not been corrected. 49

4.4 The photoconductivity spectrum obtained with a 2V bias for the 105U device. The magent and blue line represent a PC measurement under the same conditions, we can see that there is good coherence between both. The red and green line represent the corresponding Tauc plots and the vertical line marks the GaN bandgap of 3.4 eV. The spectrum has not been corrected. 50

4.5 The normalized photoconductivity (blue) spectrum and photoluminescence excitation spectrum (green) . . . 51

4.6 IV characteristics for three devices, 210U (top), 216U (middle) and 229U (bottom), under dark (black curve) conditions, when irradiated with visible light (red curve) and when irradiated with two different UV sources, the Deuterium lamp(magenta curve) the high-power and UV led (purple curve) on the left hand side; On the right hand side the respective gain factor between the dark current and the photocurrent obtained with the high power LED is plotted. . . . 53

4.7 Transient IV curves measured with device 229U: the light was turned on and off only once on the left graph to calculate the decay time and turned on and off several times on the right to calculate the rise times. The blue line corresponds to the experimental data and the red line is the fit for the decay time . . . 55

4.8 The obtained I-V curves when performing electrical measurements during proton irradiation;(left) ionoresponse of the wire when beam sweeps over the device;(right) Comparison of the I-V curve obtained under dark conditions and under continuous proton exposure. . 58

4.9 Gain ratio between I_{rad} and I_{dark}. . . . 59

4.10 The decay conductivity of the 110U device while being exposed to ionizing irradiation; On the left side the I-V curves over the full bias are shown where the legend indicates how long the device is exposed to the irradation; The right graph shows the current decay at fixed bias . . . 59

4.11 The resistance increase as calculated from the I-V curves measured while irradiating the sensors with protons. The graph on the left corresponds to the 105U device and the graph on the right corresponds to the 110U. The irradiation was carried on until the device was disrupted. . . . 60

4.12 Sensor degradation while exposing them to ionizing irradiation with an applied bias and without applying bias . . . 60

4.13 Transient I-V measurements relative to the device response to ionizing radiation; On the left side the decay time after a short pulse was measured (the pulse is represented in more detail in the inset) and on the right side the decay time after a pulse of 25 seconds was measured. The blue line corresponds to the experimental data and the red line corresponds to the fit result . . . 61

4.14 The I-V measurements after each annealing step for the 229U device . . . 63

4.15 I-V characteristics of three devices, 210U (top), 216U (middle) and 229U (bottom), after irradiation dark environment and under exposure of the UV led source. On the left hand side the I-V curves are shown, the black curve corresponds to I_{dark} and the magenta curve to I_{uv}; on the right hand side the gain ratio of the respective curves is plotted 64
4.16 Transient IV chracteristics for the 216U device. In the left graph, the bias was fixed at 3 volts and in the right graph at -3 volts. Since the decay time for negative bias is fast, the UV light was turned on and off several times. The blue dots correspond to the experimental data and the red lines to the respective fits. 65

List of Tables

1.1 Summary of the different investigations done by groups of researchers on GaN nanowire based UV radiation sensors 5

2.1 The most important properties of wurtzite-GaN at room temperature [32] 10

3.1 N7000 deposition conditions for the TiW layer 30

3.2 Photolithography parameters used in 1^{st} lithography 31

3.3 N3600 etching parameters 31

3.4 Alcatel SCM 450 deposition parameters 32

3.5 Photolithography parameters used in 1^{st} lithography 33

3.6 Alcatel SCM 450 deposition parameters for Cr/Au contacts 34

4.1 Fit parameters obtained from the data curves shown in fig.4.1 48

4.2 Experimental parameters used for the PCS measurement shown in fig.4.3 49

4.3 The resistance extracted from the I-V curves under different lighting conditions for three devices: 210U, 216U and 229U. 54

4.4 Results of the fit parameters of the decay and rise time 56

4.5 Results of the fit parameters for the decay time after a short pulse with the proton beam and after a longer pulse, $\sim$ 25 sec, on the 229U device. 61

4.6 The resistance extracted from the I-V curves under different lighting conditions for three devices: 210U, 216U and 229U. 63

4.7 Results of the fit parameters for the decay time at a positive bias of 3 Volts and a negative bias of -3 volts, regarding two devices, 210U and 216U, after they were exposed to ionizing radiation. 65

B.1 Obtained resistances and current gain factors for three devices (210U, 216U and 229U) under different irradiation situations. Note that, for sample 216U, the excitation before and after the irradiation was done with the UV led source, while during the irradiation the protons are responsible for the generation of excess electrons. $R_{UV_{led}}$ corresponds thus to the former two while R_{rad} corresponds to the latter. 90

B.2 Obtained fit parameters from transient I-V measurements for three devices (210U, 216U and 229U) under different irradiation situations. Note that, for sample 229U, the excitation source before the irradiation is the UV led while during the irradiation the protons are responsible for the generation of excess electrons. I_{uv} corresponds thus to the former while I_{rad} corresponds to the latter. 90

Acronyms

UV	ultraviolet
EBL	electron beam lithography
MOCVD	metalorganic chemical vapour deposition
MSM	metal-semiconductor-metal
TE	thermionic emission
TFE	thermionic field emission
FE	field emission
PPC	persistent photocurrent
SBB	surface band bending
XRD	X-ray diffraction
PR	photoresist
RF	radio-frequency
SVG	Silicon Valley Group
DWL	direct write laser
IPA	isopropyl alcohol
SMUs	source measuring units
I-V	current-voltage
SSPC	steady-state photoconductivity
TPC	transient photoconductivity

PCS photoconductivity spectroscopy

SRIM stopping and range of ions in matter

RTA rapid thermal annealing

PLE photoluminescence excitation

BME Burstein-Moss effect

BGR bandgap renormalization

1

Introduction

Contents

1.1 Motivation and Background 3

1.2 Objectives 6

1.3 Outline 6

1.1 Motivation and Background

The continuous downscaling in size of what we can build and produce with micro- and nanotechnology has fomented an incredibly big amount of research that tries to connect things we barely see with microscopes to real life applications. A large branch of this research is dedicated to nanostructures based on wire-like geometries, with diameter and height in the nano and micrometer range. Nano and microwires are so popular because they are excellent building blocks for bottom-up approaches, where functional structures are conceived by controlled placement of single structures. In comparison to the traditional top-down approach, the bottom-up approach has the capability to yield a completely different type of devices due to the fact that the nanometer-scale metrics are not defined by lithography, but rather by synthesis and assembly [1].

Regarding the materials used to conceive high quality semiconducting wires, gallium nitride (GaN) has been one of the most popular used compounds for many years already. GaN is a III-V compound semiconductor, more specifically part of the group III nitrides. These are known to be very interesting in device applications for light emitters and detectors in the visible and ultraviolet (UV) portions of the optical spectrum and high-power amplifiers. Major breakthroughs and developments in the field of GaN have taken place since the 1990s, including the discovery of efficient blue light-emitting diodes by Akasaki, Amano and Nakamura [2], which was awarded with the Nobel prize for Physics in 2014. The main properties that distinguish GaN from other semiconductors are its wide and direct bandgap, its thermal and chemical stability, the ability to support heterostructure technology and its high radiation hardness. The fact that it has such a wide bandgap allows for shorter wavelength emissions and increases the breakdown field, furthermore, it also makes GaN insensitive to any radiation in the visible range.

On the other hand, micro- and nanowires have recently come up as novel building blocks for bottom-up fabrication techniques. They are so widely investigated nowadays because typically, they present a very good crystalline quality. Additionally, the large surface-to-volume ratio associated with these structures make them excellent building blocks for UV photodetectors and radiation sensors [3, 4].

In comparison to their bulk counterparts, GaN nanowire-based photodetectors have achieved higher photoconductive gain and greater sensitivity. Nonetheless, these devices also present several limitations such as large decay times and the existence of a persistent photocurrent. Furthermore, when assembling a device, special care must be taken when depositing the contacts as typically it will modify surface state properties, which can harm the reproducibility characteristics of the radiation sensor [5]. In addition, two very important parameters to create commercially interesting sensors are gain and response time. In general, in nanowire sensors there has been a fundamental trade-off between the photoconductive gain and speed of photodetectors, as the increase of one of those parameters usually decreases the other [3].

So far, the potential of GaN nanowire-based photodetectors has already been demonstrated, how-

ever, very little investigation has been done on the sensing capabilities of GaN nanowires to heavy particles such as protons, neutrons and ions. Consequently, the assembly of a radiation sensor which can detect heavy particles can potentially fill this gap. If the detection of heavy particles, in this work protons, is achieved, the possibility to fabricate detectors that can work under several extreme environments becomes plausible.

The key breakthrough for GaN-devices is generally attributed to the discovery of a two-step growth for the heteroepitaxy of GaN on c-plane sapphire [6] and the first reports on GaN photodetectors started arising in the beginning of the 90s. Khan *et al.* were the first group to successfully fabricate photoconductive ultraviolet sensors based on single-crystal GaN. The epilayer structure consisted of a 0.8 μm thick layer of insulating GaN deposited over a 0.1 μm thick AlN buffer layer on top of a sapphire substrate. Although the responsivity was good, the response time of the devices was not yet fast enough to make them interesting for applications [7]. This problem was suppressed when the fabrication evolved from devices with interdigitated electrodes to devices containing a vertical geometry, transparent Schottky barrier. The obtained responsivity of the devices decreased significantly but they had very fast response times, down to 118 ns [8]. The investigations on GaN photodetectors received an enormous boost from the positive results obtained and various different types of structures were tested, such as p-n junction [9], p-i-n [10] and p-π-n [11] configurations. Nonetheless, when stable processes to grow nanowires were defined, the focus shifted towards geometries based on single or multi wires devices. In comparison to layered devices, the wire structures present a much larger surface to volume ratio, which is advantageous in detection applications.

Two main approaches can be used to fabricate radiation detectors based on semiconducting wires contacted by two terminals at their extremities. One approach is to deposit contacts by lithography and lift-off techniques on previously dispersed wires. For the lithography step it is possible to use electron beam lithography (EBL) as well as optical lithography. The former has the advantage that it is a powerful tool which can create paths with precision below 10 nm, nonetheless, it can only create a low number of devices per EBL run [12]. The latter method is quite fast but has the drawback that it usually relies on the random deposition of contacts on the wires, making it more suitable for multiple wire devices. The other approach consists on creating the contacts first and afterwards disperse nanowires on top of them. Although it is usually a fast and efficient method it is also more suitable for multiple wire devices [13]. So far, mainly the EBL methodology has been applied as it is better to create single wire devices, more suitable for the study of the electrical and optoelectrical characteristics of the GaN nanowires.

The integration of the wires in electric circuits is not an easy task. First and foremost, their small dimensions and high aspect ratio make them hard to handle but size is not the only issue. Electrical integration of the nanowires is an especially difficult task because it is hard to achieve good reproducibility regarding the contacts between the metal and the nanowires. Furthermore, there are a lot of factors

that influence the resistivity of the wire such as crystalline structure, defect density, surface morphology, surface states, etc. Therefore, a thorough understanding of the relevant physical properties, such as surface and interface relaxation and carrier confinement are required [14]. Through the past decade, several groups successfully assembled UV radiation sensors and performed electrical measurements using nanowires. Typically, the electrodes consist of Ti/Al/Ti/Au [15], Ti/Au [16, 17], Ni/Al [18] or even Ag [19]. In table 1.1 some devices and respective researchers are indicated.

Researchers	**Growth Mechanism**	**Device Substrate**	**Contact material**	**Contact fabrication**
R. Callarco et al. [16]	Plasma assisted MBE	SiO_2	Ti/Au (100/10 nm)	EBL (after wire dispersion)
E. Stern et al. [18]	Hot-wall CVD	SiO_2	Ni/Au (200/50 nm)	Photolithography (after wire dispersion)
R. S. Chen et al. [20]	Vapor-liquid-solid CVD	SiN_x	Ti/Au(30/150 nm)	Shadow mask and e-beam evaporation (after wire dispersion)
J. Lee et al. [17]	Vapor-liquid-solid CVD	SiO_2	Ti/Au (20/130 nm)	Photolithography (before wire dispersion)
H. Chen et al. [21]	Vapor-liquid-solid CVD	SiN_3	Ti/Au (30/150 nm)	EBL (after wire dispersion)
F. González-Posada et al. [15]	Plasma assisted MBE	SiO_2	Ti/Al/Ti/Au (5/25/15/100 nm)	EBL (after wire dispersion)
X. Wang et al. [19]	MOCVD	SiO_2	Ag(200 nm)	grid mask with e-beam evaporation (after wire dispersion)

Table 1.1: Summary of the different investigations done by groups of researchers on GaN nanowire based UV radiation sensors

Only very few investigations have been done on nanowire based radiation sensors while irradiating them with heavier particles. Ayres *et al.* [22] studied the behaviour of GaN nanowire FET designs while striking them with a primary beam of ^{78}Kr at 140.32 MeV per nucleon. I-V characteristics were taken before, during and after the irradiation. Normal real-time and post-radiation electric function was observed. Furthermore, when analysing seven irradiated samples, only two presented areas that were significantly damaged. As far as bulk GaN-based particle detectors go, several successful attempts have been made. Vaitkus *et al.* [23] developed a thin film detector and realized α-particle detection using a double-Schottky structure. The detection was done using 5.48 MeV α-particles emitted from an ^{241}Am source. Other structures fabricated on bulk GaN also successfully detected α-particles [24, 25]. The ion induced conductivity characteristics of Zinc Oxide, a semiconductor with a similar crystal structure and bandgap to GaN, nanowire FETs treated with proton or ion irradiation have been analysed. Johannes *et al.* [26] used ion beams to generate electron-hole pairs in vapor-liquid-solid grown ZnO nanowires, contacted with Ti/Au (50/50 nm) electrodes. The devices were irradiated with a wide range of energies, ion-currents and total fluxes while measuring the conductance. Beside a remarkable increase of the current also a strong persistent ion-beam current was observed. Choe *et al.* [27] used accelerated proton beams, generated using an MC-50 cyclotron, with a beam energy of 10 MeV, to irradiate ZnO

wires grown by chemical vapour deposition. The electrical properties were systematically characterized before and after the proton irradiation.

1.2 Objectives

The main objective of this investigation consists in achieving a reproducible fabrication method to build GaN microwire based radiation sensors and analyse them in terms of their electrical and optical properties. Although the big majority of reports so far are relative to structures based on nanowires, we chose to use microwires instead because their larger volume makes them better suited for high energy particles and X-rays. In this way, the idea is to settle a compromise between the better crystalline quality associated to wire-based GaN and the larger volume of bulk GaN. On the other hand, the fact that microwires are larger, makes the fabrication process more straight forward. Thus, to reach the defined goal, metalorganic chemical vapour deposition (MOCVD) grown microwires are dispersed on a substrate and optical lithography and lift-off techniques are used to fabricate devices. The fabrication of the devices is done at the facilities of INESC-MN. Electrical measurements are done under dark environment, with UV lighting and with proton irradiation striking the device. The current response during UV and proton irradiation are analysed and discussed considering the induced defects, including the consequences of these created defects by the proton irradiation on the operation of the device are extensively investigated. As indicated, although the concept of GaN sensors based on wired arrays has been proven, there are still issues and inconsistencies and with this research we want to take a step in the direction of a more generalized procedure and propose methodologies to solve some of the inherent problems. If the mechanisms are well understood and controllable, we will be able to use the device for many applications including proton (and other heavy particles) and photon detection, countable ion implantation and in environments that are characterized by its extreme conditions, like space, nuclear reactors and so on.

1.3 Outline

This thesis is divided in 5 chapters. In chapter two a brief theoretical description will be given regarding the processes of interest for the device characterization and subsequent analysis. Chapter 3 consists of a recapitulation of the microwire growth process, the sensor fabrication methodology and a description of the electrical and optical characterization procedures as well as the irradiation facilities. The resultant data of the experimental work will be described and treated in chapter 4. Finally, in the last chapter the most important results and conclusions are summarized and some indications of future work will be given.

2

Theoretical Background

Contents

2.1 Gallium Nitride properties 9

2.2 Metal-semiconductor-Metal configuration 11

2.3 Effects of ionising radiation on GaN 19

In the following chapter a brief description of the theoretical background of interest for this work will be given. The properties, such as the band structure, the crystallographic information and electrical and optical characteristics of GaN will be addressed. Then, the important physics concerning the metal-semiconductor interfaces, such as the junction and surface dynamics, transport mechanism and application for photodetectors will be explained. Finally, the effects that ionizing, and other types of radiation, have on GaN will be covered.

2.1 Gallium Nitride properties

In terms of the crystal structure of this material, the stable phase at ambient temperature is wurtzite, as is shown in figure 2.1. This structure has a hexagonal unit cell with two lattice parameters *a* and *c* of which the ideal ratio is $c/a = \sqrt{8/3} = 1.633$. The structure is composed of two interpenetrating sublattices which include four atoms per unit cell, where every atom of one kind is surrounded by four atoms of the other kind, or vice versa. The most relevant properties of GaN are summarized in table 2.1. The reported lattice parameters are $a = 3.190$ Å and $c = 5.189$ Å [28]. However, these values can vary slightly under the influence of a higher or lower free-electron concentration. In fact, measurements on wurtzite GaN with an electron concentration of 5×10^{19} cm^{-3} indicated lattice parameters of $a = 3.189$ Å and $c = 5.186$ Å [29]. The way the free-electron concentration acts on the crystal structure is through the deformation potential of a conduction-band minimum occupied by these electrons. As said, the bandgap of GaN is wide, the reported value for the energy between the highest occupied state in the valence band and the lowest unoccupied state in the conduction band is 3.39 eV at room temperature [30]. This corresponds to a wavelength of approximately 365 nm and consequently radiation with higher wavelengths will not be absorbed if there are no defect states within the bandgap. Regarding the effective density of states in the conduction and valence band, they can be evaluated by applying the following equations [31].

$$N_c = 2\left(\frac{2\pi m_n^* kT}{h^2}\right) \tag{2.1}$$

$$N_v = 2\left(\frac{2\pi m_p^* kT}{h^2}\right) \tag{2.2}$$

where m_n^* and m_p^* are the effective electron and hole mass, respectively, k the Boltzmann constant, T the temperature and h the Planck constant.

Using the parameters at $T = 300K$ indicated in table 2.1, we achieve a value of $N_c = 2.24 \times 10^{18}$ cm^{-3}. For the valence band, spin-orbit splitting occurs. In the vicinity of the valence band maximum, spin-orbit interactions and crystal splitting cause threefold splitting of the top of the valence band. The resulting bands are identified as the heavy band, the light band and the split-off band [33]. Their respective effective density of states are $N_v = 4.15 \times 10^{19}$ cm^{-3}, $N_v = 4.11 \times 10^{18}$ cm^{-3} and $N_v = 1.16 \times 10^{19}$ cm^{-3}.

Density	6.15 g/cm^3
Dielectric constant	8.9
Effective electron mass	$0.20m_0$
Effective hole masses	
heavy	$1.4m_0$
light	$0.3m_0$
split-off band	$0.6m_0$
Effective density of states in the conduction band	2.24×10^{18} cm^{-3}
Effective density of states in the valence band	
heavy	4.15×10^{19} cm^{-3}
light	4.11×10^{18} cm^{-3}
split-off band	1.16×10^{19} cm^{-3}
Electron affinity	4.1 eV
Breakdown field	$\sim 5 \times 10^6$ V/cm
Mobility	
electrons	≤ 1100 cm^2/Vs
holes	≤ 200 cm^2/Vs

Table 2.1: The most important properties of wurtzite-GaN at room temperature [32]

The full band structure, with corresponding transition energies is depicted in figure 2.1.

Regarding the mechanical properties, GaN can be considered as a hard and incompressible material family member and its elastic and bulk moduli are of the same order of magnitude as those of diamond [34]. Furthermore, GaN and other group III nitrides semiconductors present a high thermal conductivity. Scanning thermal microscopy measurements done on GaN reported maximum values in the 2.0-2.1 W/cmK range [34], and also revealed a correlation between the doping level and the thermal conductivity as the data showed a linear decrease of the former with $\log n$, where n is the electron concentration [35]. The fact that GaN presents such good thermal dissipation is not only a useful characteristic in optoelectronic devices but also makes it very interesting for high-power/high-temperature applications. The electron mobility in GaN is one of the most important parameters associated with the material and has great impact on devices. Early reports indicated values of 600 cm^2/Vs for an electron concentration

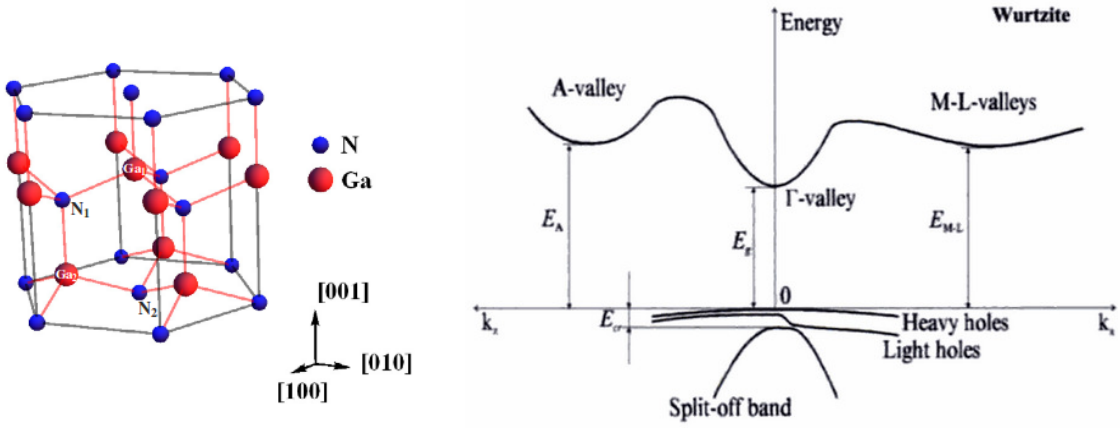

Figure 2.1: Band (right) and crystal (left) structure for Wurtzite GaN. The subscripts in the left graphic denote the two non-equivalent positions for each site. [32, 36]

of $\sim 3 \times 10^{16}$ cm^{-3} and 100 cm^2/Vs for an electron concentration of $\sim 3 \times 10^{18}$ cm^{-3} [37]. However, as the fabrication processes were optimized and the crystalline quality increased, the measured mobilities also presented a significant improvement and values upto 1100 cm^2/Vs at room temperature were reported [38]. Additionally, as mentioned, associated with the wide bandgap, are high breakdown voltages, the ability to sustain large electric fields and lower noise generation.

2.2 Metal-semiconductor-Metal configuration

2.2.1 Metal-semiconductor junction

The metal-semiconductor-metal (MSM) configuration is made out of two back-to-back junctions between a metal and a semiconductor that form contacts. In a first analysis, we will look solely at a single contact. In the ideal case, the type of contact that is formed at the junction depends on the voltage differences between the electron affinity, $q\chi$, of the semiconductor and the work function, $q\phi_m$ of the metal. In figure 2.2, the energy-band diagrams of a metal and an n-type semiconductor before contact(2.2(a)), and after creating the junction for $\phi_m > \phi_{sc}$(2.2(b)) and for $\phi_m < \phi_{sc}$(2.2(c)) are represented. In this thesis we will use n-type GaN and therefore we will only discuss this case. Before contact, as there does not exist any potential between the metal surface and the semiconductor surface, the Fermi energy levels, E_f, are intrinsic to the materials. In the metal, E_f is equal to the work function and corresponds to the difference between the vacuum level and the highest occupied states in the conduction band. For the n-type semiconductor, the Fermi level lies in the vicinities of the conduction band. The exact location depends on the concentration of donors. After contact, as we can see, the diagrams are quite different depending on the work functions of the materials, and so is the current-voltage behaviour.

Starting with the former condition, $\phi_m > \phi_{sc}$, this type of contact is called a Schottky or rectifying

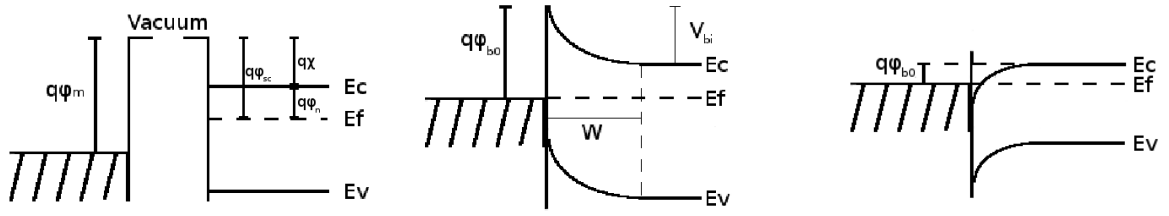

(a) Metal and semiconductor before contact

(b) Schottky contact

(c) Ohmic contact

Figure 2.2: Energy band diagrams of an individual metal and semiconductor and of the possible junctions. $q\phi_m$, $q\phi_{sc}$, $q\chi$, $q\phi_n$ represent respectively the metal work function, the semiconductor work function, the electron affinity and the difference between the conduction band and the Fermi energy. After contact, $q\phi_{b0}$ is the Schottky barrier height, V_{bi} the built-in voltage and W the depletion width.

contact. In order to achieve a constant Fermi level, electrons from the semiconductor flow into the lower energy states of the metal. The donor atoms that supplied these electrons, become positively charged and a depletion region is formed. The electrons in the metal that try to move into the semiconductor encounter a potential barrier ϕ_{B0}, known as the Schottky barrier. In the ideal case the height of this barrier is given by the potential difference between $q\phi_m$ and $q\chi$. Furthermore, the electrons in the conduction band that try to move into the metal also encounter an obstacle potential, called the built-in potential barrier, V_{bi}. This potential is given by the difference between ϕ_{B0} and ϕ_n, the latter is the energy difference between the Fermi and the conduction band level. In case we apply a positive voltage on the metal relative to the semiconductor, although the Schottky barrier height remains constant, the built-in voltage decreases according to $V_{bi_f} = V_{bi} - V$, where V is the applied bias. The electrons flow with more ease into the metal and this bias condition is called forward bias. On the other hand, if a positive voltage is applied to the semiconductor, the situation is inverted and V_{bi} increases to $V_{bi_r} = V_{bi} + V$, making it harder for the electrons to flow into the metal. This situation is called reverse bias. If ρ is the charge density, E the electric field, x the distance from the junction and W the width of the depletion region and we make the n-type semiconductor approximation, neglecting the hole concentration, we can say that $\rho = qN_d$ for $x < W$ and that $\rho \approx 0$ and $E \approx 0$ for $x > W$. If we now solve the Poisson equation with these boundary conditions we obtain the following expression for the depletion width [39]

$$W = \sqrt{\frac{2\varepsilon_s}{qN_d}\left(V_{bi} - V - \frac{kT}{q}\right)} \tag{2.3}$$

where V_{bi} is the built-in voltage, ε_s is the relative permittivity, N_d the donor concentration, k the Boltzmann constant, T the temperature, q the magnitude of electronic charge and V the applied voltage.

In the case of the inverse condition, $\phi_m < \phi_s$, to balance the Fermi level electrons will flow from the metal into the semiconductor, making the surface more n-type. If now a positive voltage is applied on the metal, there is no barrier and electrons flow freely into the semiconductor. If the voltage condition is inverted, the effective barrier for electrons will be $\phi_{B0} = \phi_n$ which is fairly small for a moderately to heavily doped semiconductor. Subsequently, in this case the electrons will also easily flow from the semiconductor into the metal. This description essentially covers the so called Ohmic, or nonrectifying, contacts [39].

As said, these descriptions correspond to the ideal case, and, what happens in most cases is that reality is far from ideal. Considering the properties and configuration of the materials that will be used to conceptualize the radiation sensors, it is important to take into account the surface state density, Schottky effect and the doping concentration, which will be explained next.

Surface states The surface states can have a big influence on the actual Schottky barrier height, even more when we are dealing with wires that have a large surface-to-volume ratio. In an semiconductor crystal, the periodic nature of the crystalline structure is disturbed at the surface, which gives rise to a large number of permitted states in the bandgap of the semiconductor near the surface. These states are commonly called surface traps, since they capture electrons if they are below the Fermi level. These electrons form a negative surface charge, which on its own creates a depletion zone in the semiconductor and a subsequent band bending. Additionally, typically an insulating layer of atomic dimensions forms between the metal and the semiconductor, when depositing contacts. This layer will be transparent to electrons but can withstand potential across it. What happens when a semiconductor containing a large density of filled acceptor traps makes contact with a metal is that, to achieve the alignment of the Fermi levels, electrons will flow from the traps into the metal instead of what would happen in the ideal case. The influence of the alignment of the Fermi levels on the potential barrier height will therefore be negligible, as instead it will depend solely on the surface states potential [40]. In most semiconductors, the surface state density is moderate such that the height of the Schottky barrier is both influenced by the difference between the metal work function and the electron affinity of the semiconductor, and the surface potential. However, for III-V compounds, including GaN, reports have indicated that the Schottky barrier formation is mostly influenced by the defects generated near the interface due to the deposition of the metal, making it essentially independent of the metal work function [41, 42].

Schottky effect In the ideal case, the barrier height is constant, independent of the applied voltage, however, in reality minor variations can occur. These variations are a consequence of a mirror charge produced in the metal by electrons in the semiconductor. According to electrostatics, an electron at a distance x from a "perfect" conductor will create an electric field. The field lines must be perpendicular to the metal surface and will be the same as if a mirror charge of same magnitude but opposite sign is created inside the metal at a depth equal to x. As a consequence, the charge is attracted by the metal, and in the case of the metal-semiconductor contact, the potential barrier is lowered. The attraction can be quantified by considering a Coulomb attraction between the electron and the mirror charge, separated by a distance $2x$. To obtain the total potential energy of the electron, $PE(x)$, we add the potential energy due to the Coulomb interaction to the potential energy inside the semiconductor, originated in the depletion region. By solving $dPE(x)/dx = 0$, we can calculate the distance at which this potential is maximum and subsequently, the effective lowering of the potential barrier, which constitutes the Schottky effect [43]

$$\Delta\phi_B = \left(\frac{q^3 N_d}{8\pi^2 \varepsilon_s^3}\left(V_{bi} - V\right)\right)^{1/4}. \tag{2.4}$$

We can thus write the resulting potential barrier height as $\phi_B = \phi_{B0} - \Delta\phi_B$.

Although the Schottky barrier lowering typically seems a small value, one must not forget that the

barrier height will appear in exponential terms in the current density, as will be shown in the following section. Therefore, a small change in the barrier height can have a significant effect on the current density.

Doping concentration It is also possible to obtain an ohmic like contact when creating a junction between a metal and a semiconductor that would, under normal conditions, create a Schottky contact. If the doping concentration in the semiconductor is high enough, the thickness of the depletion width will decrease to values through which the electrons can easily tunnel since $W \propto N_d^{-1/2}$ (see eq.2.3). Consequently, a current density similar to that of a low-resistance ohmic contact will exist. In fact, ohmic contacts between a metal and the terminals of semiconductor devices are typically made on heavily doped areas. An example of the energy band in such a configuration can be seen in figure 2.3.

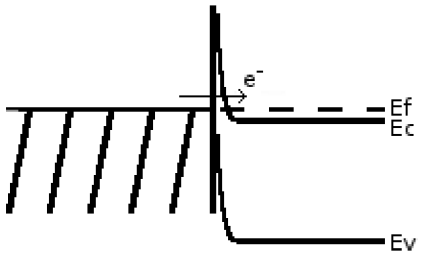

Figure 2.3: Energy band diagram for a metal-semiconductor junction with n^+ doping

2.2.2 Back-to-back Schottky contacts

As is obvious, to create a functioning device, not one but two contacts must be fabricated. Thus, we will have in fact two separate back-to-back metal-semiconductor junctions. The properties of both contacts are not necessarily the same though. For example, to create a simple Schottky diode, one needs to deposit one Schottky contact and one Ohmic contact. Like this, the low resistivity of the Ohmic contact does not interfere significantly and, in the ideal case, pure Schottky-type behaviour is observed. In this work, both contacts will be fabricated in the same way using chromium and gold. The work functions of these metals are higher than the electron affinity of GaN so, ideally, we should obtain back-to-back Schottky contacts. However, the aforementioned effects on the barrier height do strongly affect the actual behaviour of the obtained contacts. Especially the surface states, due to the large surface-to-volume ratio and the doping concentration, which, as is explained in more depth in the following chapters, is high. Nonetheless, our measurements show rectifying behaviour and therefore the electron transport mechanisms of back-to-back Schottky contacts will be adressed.

Typical band diagrams under zero bias, and negative and positive bias for a back-to-back Schottky configuration are depicted in figure 2.4. In this case, whether we apply a positive or a negative bias,

there will always be one contact in reverse bias and the other in forward bias. For example, if we apply a positive bias on the right metal contact, the barrier is reduced and electrons flow easily from the semiconductor into the metal. At the left metal contact, the Schottky barrier, ϕ_{b1} that exists at the junction will stop a big part of the electrons. Consequently, in most Schottky based MSM devices a nonlinear I-V behaviour is observed.

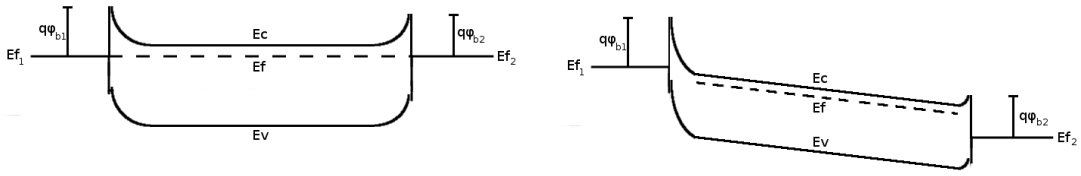

Figure 2.4: Energy band diagrams for a typical MSM structure under zero bias (left) and with a positive bias applied on the right contact (right)

Current density model Figure 2.5 represents the equivalent circuit corresponding to a radiation sensor as is fabricated in the scope of this investigation. The back-to-back Schottky diodes are separated by a semiconducting GaN wire and V_1, V_2 and V are the respective voltage drops at each section. Regarding the electron transport mechanism that governs the I-V characteristic of a typical Schottky diode, the thermionic emission (TE) model is frequently used to explain it. However, under certain conditions, this model does not suffice to explain observed results and thermionic field emission (TFE) or field emission (FE) must be considered.

Thermionic emission was discovered in the late fifties and can be described, in a simple fashion, by the emission of electrons when a conducting body is heated to a sufficiently high temperature [44]. It can be compared to the photoelectric effect, but instead of photons, heat causes the emission. When we apply TE to a metal-semiconductor interface, it can be seen as the electrons overcoming the depletion region by going over the created Schottky barrier. For this to happen, the electrons need to have high enough kinetic energy. The TE characteristics can be derived by assuming that the barrier height is much larger than k_bT, so that the Maxwell-Boltzmann approximation applies and that thermal equilibrium is not affected by this process [45]. According to the theory, the current density is given by [43],

$$J_{TE}(V,\phi_B) = A^*T^2 \exp\left(-\frac{\phi_b}{kT}\right) \exp\left(\frac{qV}{nkT}\right)\left[1-\exp\left(-\frac{qV}{kT}\right)\right] \tag{2.5}$$

Where $A^* = 4\pi m_n^* qk^2/h^3$ is the Richardson constant, ϕ_b the effective barrier height, k the Boltzmann constant, q the magnitude of electronic charge, T the temperature and n the ideality factor that describes the deviation from an ideal Schottky diode. This model was applied when analysing I-V curves of GaN

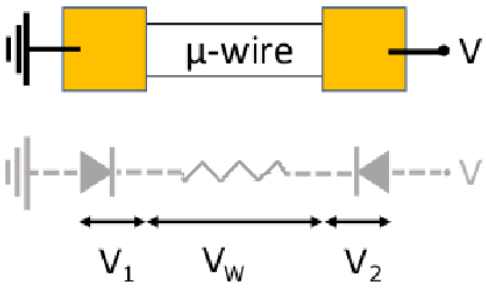

Figure 2.5: Equivalent circuit of an MSM photodetector

nanowires by Kim *et al.* [46] and temperature dependent measurements were performed. It was seen that, at high temperatures, when kT is comparable or larger than the barrier height, TE is in fact the dominant current transport mechanism. However, at low temperatures the current is underestimated. This indicates that other current transport mechanism also play a role; the most important is the tunneling current.

As said, to explain the main component that is responsible for the appearance of a current when the system is in reverse bias, one needs to take into account quantum mechanical tunnelling. This yields a more general emission theory that goes by the name of thermionic field emission. In fact, tunnelling becomes especially important when dealing with barriers that are relatively low and/or when the a semiconductor is moderately to heavily doped [39]. Furthermore, it has been reported that low dimensional systems also promote tunnelling [47]. In 1966, Padovani and Stratton published a paper in which they defined a model for TFE [48] and, based on this model, an expression for the current density can be derived. The following expression has been simplified by considering an n-type semiconductor for which we can neglect the hole current [49].

$$J_{TFE}(V,\phi_B) = J_{sr}(V,\phi_B)\exp\left[V\left(\frac{q}{kT}-\frac{1}{E_0}\right)\right] \tag{2.6}$$

where J_{sr} is a slowly varying function of applied bias,

$$J_{sr} = \frac{A^*T\sqrt{\pi qE_{00}}}{k}\exp\left(-\frac{\phi_b}{qE_0}\right)\sqrt{q\left(V-\phi_n\right)+\frac{\phi_b}{\cosh^2(qE_{00}/kT)}} \tag{2.7}$$

Regarding the parameters E_0 and E_{00}, they are given by

$$E_0 = E_{00}\coth\left(\frac{qE_{00}}{kT}\right) \tag{2.8}$$

and

$$E_{00} = \frac{\hbar}{2}\sqrt{\frac{N_d}{m_n^*\varepsilon_s\varepsilon_0}}, \tag{2.9}$$

where N_d is the donor density at the metal-semiconductor interface and m_n^* and ε_s respectively the effective electron mass and relative permittivity of the material, in this case GaN. E_{00} is a fundamental parameter as it is the diffusion potential of a Schottky Barrier such that, the transmission probability for an electron whose energy coincides with the bottom of the conduction band at the edge of the depletion region, is equal to $1/e$ [43]. Typically, when $kT/E_{00} \gg 1$ the current flow can be purely described by TE while, when E_{00} is of the order of kT, TFE must be considered [50].

However, the previous two models do not cover the current behaviour for $kT/E_{00} \ll 1$. This typically occurs for heavily doped semiconductors, when they become degenerate. When this is the case the Fermi level lies above the bottom of the conduction band and the contacts start to present a non-rectifying behaviour, as mentioned before. The reason this happens is that, because of heavy doping, the thickness of the depletion region becomes very thin and electrons with energy close to the Fermi level can tunnel from the semiconductor into the metal, or vice-versa [45]. In fact, if we apply the expression for the depletion width (eq.2.3) for wurtzite GaN with $\varepsilon_s = 8.7$ and if we consider, for example, a doping concentration of $N_d = 10^{20}$ cm^{-3} and $V_{bi} - V$ between 0.1 and 1 volt, we can estimate that the width is in the $1 - 3$ nm range. This tunnelling process is known as field emission. The current density, as derived by Padovani and Stratton [48], can be described by the following relation

$$J_{FE}(\phi_b, V) = A^* \left(\frac{E_{00}}{k}\right)^2 \left(\frac{\phi_b + V}{\phi_b}\right) \exp\left(-\frac{2q\phi_b^{\frac{3}{2}}}{3E_{00}\sqrt{\phi_b + V}}\right) \tag{2.10}$$

In figure 2.6 [49], the energy band diagrams show the different electron transport mechanisms for a forward bias and a reverse bias contact. It is important to note that under forward bias the barrier, as seen by the electrons, is much smaller and therefore, thermionic emission is the preferable transport mechanism. Under reverse bias though, larger voltages are plausible in the current density expressions and tunnelling starts to matter.

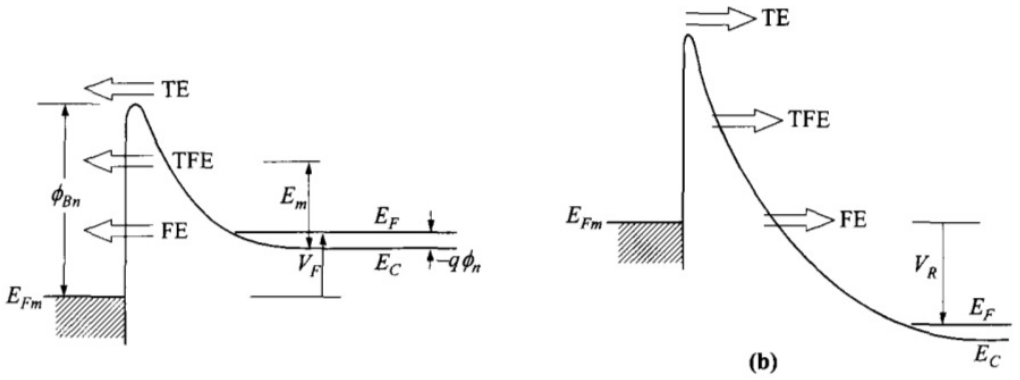

Figure 2.6: Different transport mechanisms that can occur at a metal-semiconductor contact; The left diagram corresponds to forward bias and the right diagram corresponds to reverse bias [49]

2.2.3 MSM photodetectors

The operation principle of an MSM photodetector is simple, if the device is illuminated with light that has a smaller wavelength than the cut-off wavelength, defined by the bandgap, electron-hole pairs are generated and a photocurrent appears. When such an excitation source is present, the excess electrons and holes are generated at a particular rate. Let g_n be the electron generation rate and g_p the hole generation rate. Since both are created in pairs, the equality $g_n = g_p$ must be sustained. If we consider an n-type semiconductor, the overall hole concentration can be neglected while the electron concentration becomes $n = n_0 + \Delta n$. If the source that is responsible for the $e^- - p^+$ generation is working in a steady-state, there will not be a continuous build-up of the carrier concentration. Instead, electrons in the conduction band will start to recombine with holes in the valence band. Similar to the generation rates, the recombination rates, R_n and R_p must be equal. If we consider direct band-to-band recombination, it will occur spontaneously and the probability of it occurring will be constant with time. Furthermore, the rate at which electrons recombine must be proportional to the electron concentration [39]. If an external bias is applied, the generated electrons and holes, as they have different charges, get pulled into opposite directions. The carriers are collected by the metal pads and the photocurrent is detected in the external circuit. Intuitively, the most favourable type of contacts for an MSM photodecetor are ohmic contacts. The low contact resistivities are very usefull since their interference can be easily described when studying the properties of the device.

Several groups achieved to successfully deposit Ohmic contacts on GaN nanowire based photodetectors and very high gain values have been achieved [20]. However, most of the times, a fundamental trade-off exists between the photoconductive gain and the speed of the devices, long carrier lifetimes enhance the photocurrent and gain but the response time will suffer and increase [21, 51]. Both the high gain and long response times can be seen as a consequence of a persistent photocurrent (PPC) mechanism. The effect of PPC in nanowires is generally associated to surface band bending (SBB) due to the pinning of the Fermi level at the surface of the semiconductor. When SBB occurs, a built-in electric field is generated that separates the photogenerated electrons and holes. Since the holes have a positive charge, they will tend to occupy the higher energy states in the Valence band and thus diffusive to the surface, where the band is bent upwards. On the contrary, the negatively charged electrons will tend to drift to the bulk region in order to occupy the lowest energy states available. This reduces the surface charge density and consequently decreases the amount of band bending [52]. The thickness of the space-charge region associated with the surface states also becomes smaller, which will lead to a wider conduction area yielding an extremely large photocurrent. When the excitation source is shut off however, the electrons in the conduction band will have to recombine with the holes that are trapped at the surface. The recombination occurs via thermionic emission and the associated recombination rate is quite slow, hence the appearance of PPC. Callarco *et al.* demonstrated that the SBB is strongly de-

pendent on the diameter of the nanowires. If the diameter is small enough, the semiconductor becomes fully depleted. Firstly, this makes them insulating in the dark and secondly, it reduces the bending of the valence and conduction band, decreasing the influence of PPC. For wires that are not completely depleted, high gain can still be achieved but due to the complete band bending, PPC is more significant [16]. The PPC effect was also extensively reported in bulk GaN [53, 54, 55]. The principle that significant band bending is responsible for the long decay times is maintained, however, in bulk GaN it is not solely a surface effect as Fermi level pinning also occurs in the bulk region. Although the origin of PPC in bulk GaN is still under discussion, in many cases it is attributed to metastable defects [56]. Additionally, grain boundaries [57] and charged dislocations [55] have also been reported as responsible for the long decay times after excitation. In fact, for GaN, it has been reported that the predicted results of the general theory behind carrier generation and recombination are in flagrant disagreement with experimental results, and this has been attributed to the aforementioned mechanisms [58]. The mechanisms do not only prolong the lifetime of the excess carriers, but are also responsible for non linearities in the gain dependence on the illumination power and absorption of photons with energy below the gap energy.

As said, typically Ohmic contacts are favoured over Schottky contacts as this allows to increase the photocurrent gain and sensitivity. However, it was shown that, in this case Schottky contacts can reduce the influence of PPC, since Schottky barriers can be used to confine the current when the excitation source is shut off [19]. When excess electrons are generated, the potential of the barrier in reverse bias at the metal-semiconductor interface will also separate the photogenerated electrons and holes. This will lead to a lowering of the respective barrier height and a subsequent increase in the current. When the excitation source is turned off, the barrier height of the reverse biased contact increases immediately, which results in a quick current loss. Although the recombination of the excess carriers is still a slow process, it will not induce a persistent current because the Schottky barriers drastically slow down the emission of electrons. Consequently, structures with back-to-back Schottky contacts have gained in popularity for the application in GaN nanowire photodetectors. Recently, Wang et al. [19] reported a sensitivity up to 10^4 AW^{-1} and rise and decay times below 26 ms with a GaN nanowire back-to-back Schottky pohotodetector. Such values have not been obtained for UV detectors based on bare nanowires without any surface or composition modification using ohmic contacts.

2.3 Effects of ionising radiation on GaN

Several reports on the high resistance of GaN to ionizing radiation, allow to conclude that GaN has a big potential to be used as material for radiation applications and devices [59]. However, it also has some serious disadvantages regarding the application to radiation detectors such as the wider bandgap,

that reduces the number of electron-hole pairs produced in a single event and, on the other hand, there is still a lack of high quality thick uniform bulk crystals or epitaxial layers. Therefore it is unlikely that GaN will replace the established materials in standard radiation spectrometry tasks. However, in specific environments where detectors with a high radiation resistance and temperature stability are required, like in space, it is a different story. Subsequently, it is important to study the effect irradiation has on the material, especially regarding the changes in the absorption spectrum, electrical properties and the position of the Fermi level.

The main reason the properties of a material are changed under the influence of energetic particle radiation is the production of defects. In GaN, independently of what kind of irradiation is used, *e.g*, electrons, protons or neutrons, the most basic primary defects created are Frenkel pairs in the Ga and N sublattices [59]. These pairs can be responsible for the introduction of donor levels through nitrogen vacancies and acceptor states associated with nitrogen interstitials [60]. Additionally, the gallium vacancies are also supposed to produce acceptor states while the gallium interstitials create another donor level [61, 62]. The generation of acceptor states has a direct influence on the carrier concentration in the semiconductor since they will trap excess electrons as soon as they are created. Clearly, this will also influence the position of the Fermi level. If, however, Frenkel pairs were produced by irradiation the decrease in carrier concentration should be equal to the production rate of the acceptor states, which is usually not observed in the measurements [63, 64]. The reason for this, is the clustering of the primary defects, which together form highly disordered regions. Besides the decrease in the carrier concentration, the lifetime of carriers is also reduced due to the production of carrier traps as a consequence of the irradiation [65]. Regarding irradiation of n-GaN ($n \sim 10^{17}$ cm^{-3}) with a 2 MeV proton beam, a carrier removal rate of 260 cm^{-1} was measured and three defect levels, at 0.13, 0.16 and 0.2 eV from the conduction band were observed. Uncertainty exists about the defect type of the former two while the latter is of acceptor type. What the energies of the defect levels thus indicate is that they are shallow levels, just beneath the conduction band [66]. To recover some of the induced defects by irradiation, thermal annealing can de done. It was found that the shallow radiation defects start to anneal at 540 K, but a temperature of 660 K is needed to remove the majority of the defects [66]. Another very important consequence of the irradiation is the consequential increase of the Schottky barrier height at the metal-semiconductor junction. The increase of the Schottky barrier was observed for exposure to both γ and proton beams. In the latter case, an increase of $\Delta\phi_b = 0.1$eV was observed at the Ni/GaN junction for a 1.8 MeV beam. [67]. As explained previously, this can drastically change the preferential mechanism of electron transport.

A model for the decrease in electrical conductivity in GaN due to exposure to proton irradiation was proposed by Titov, Karasev and Kucheyev [68]. Their assumptions are based upon the fact that the decrease in conductivity is mostly due to the increase of sheet resistance caused by the appearance of

the aforementioned defect levels in the bandgap. They also reckoned the decrease in mobility, however, reported Hall measurements on n-GaN irradiated with 0.6 MeV H^+ protons indicated a decrease of mobility of only one order of magnitude, whereas the conductivity decreased by five orders of magnitude [69]. With this knowledge, to build their model, they considered the formation of the simplest point defects of a single type, the trapping of these defects at unsaturable sinks with characteristic relaxation time τ and the interaction of these defects with the doping impurities. They concluded that the suggested model satisfactorily described the process of sheet resistance increase which is mainly related to the formation of complexes that efficiently capture the charge carriers.

3

Growth and fabrication process

Contents

3.1 Microwire growth 25
3.2 Fabrication 28
3.3 Characterization methods 35
3.4 Proton-irradiation 39

In this chapter a description of the growth process of the wires will be given, the fabrication steps followed to produce the radiation sensors will be addressed including a brief description of the used machines. At last, the electrical and optical characterization methodology, as well as to the irradiation setup will be explained.

3.1 Microwire growth

The GaN wires that were used for this investigation were grown by metal-organic chemical vapour deposition (MOCVD) at the CEA in Grenoble, France. A brief description of the growth process follows while a complete description can be found in reference [70]. MOCVD uses a combination of vapour phase precursors, in our case trimethyl gallium (TMGa) and ammonia (NH_3). These are thermally decomposed at elevated temperatures to form the desired non-volatile product that is deposited on the substrate while the volatile product is carried away to the exhaust. If we ignore any side reactions and intermediate steps we can write the reaction as follows [71],

$$(CH_3)_3Ga(v) + NH_3(v) \rightarrow GaN(s) + 3CH_4(v). \tag{3.1}$$

The methodology is highly reproducible and can be based on three main steps: the initial substrate treatment, the GaN seed nucleation and the vertical growth. In this case, the GaN wires are grown on a c-plane sapphire substrate, which is commonly used as substrate for GaN structures. Before exposing the substrate to the precursors, it is baked *in situ* under H_2 at $\sim$1000°C and nitrated with NH_3 to form a thin AlN surface layer. Then a layer of SiN_x is deposited by injecting simultaneously SiH_4 and NH_3 into the reactor. The duration of this deposition is a critical parameter for the wire growth as, contrary to what one might think, longer deposition times do not significantly increase the thickness of the SiN_x layer but rather increase the density related to the surface chemistry and surface roughness. Thus, by using the right deposition time, one can create a layer where the density and roughness change locally. This is fundamentally important for the next step - the GaN seed nucleation. As SiN_x is chemically inert with respect to gallium nitride compounds and is very stable at high temperatures, the weak points in the layer will give rise to the GaN seed formation. Consequently, by controlling the deposition time one can control the positioning and density of the wires since the seeds will act as corner stones for the wire growth. It was discovered that a deposition time of 100 seconds yielded the best results - hexagonal and vertically aligned wires.

After the surface treatment, the seed nucleation starts the actual growth process of the wires, and the duration has again a very important influence on the the size and crystalline quality. For longer nucleation times, the wire diameter increases and, on the other hand, the density of deposited wires decreases. Regarding the crystalline quality, it appears to worsen when applying longer nucleation

times. This is related with the fact that the GaN seeds start growing laterally. Since the substrate surface is not perfectly smooth but presents some local defects like pits emerging dislocations and surface kinks, it becomes more likely that the seeds encounter some of these defects as their size increases. If this happens, irregularities in the hexagonal shape of the wires can be induced. On the other hand, the larger the size of the seeds, the more probable it becomes that two or more seeds begin to merge, giving rise to grain boundaries which cannot be cured by a longer growth time. In the system used to grow the wires for this work, 10 seconds was defined as the optimal nucleation time to minimize the quantity of structural defects. For the final step, the vertical growth, also several key parameters exist and need to be controlled. A low V/III molar ratio favours the vertical growth and an optimal ratio in the range of 10 to 20 was found. Another key feature is an additional high flux silane flow. The silane causes the incorporation of Si donors into the wires, but, if no silane is used, the GaN forms islands that grow laterally with arbitrary shape and size. In this growth process, a flow of 45 sccm was used which corresponds to a doping level of about $10^{19} - 10^{20}$ carriers per cm^{-3} [70]. The reason the silane flow affects the growth quality is because it forms a thin SiN_x shell around the wire. As said, GaN is chemically inert with respect to SiN_x and consequently, the shell avoids lateral expansion of the wire. When the wires reach heights of about 7 μm, the silane flow can be turned off without further affecting the vertical growth for another ~ 15 μm. As a consequence of turning the silane flux off, the upper part of the wire will not be as heavily doped as the bottom part nor will it be covered by SiN_x. The doping concentration of the upper part of the wire lies in the $10^{17} - 10^{18}$ cm^{-3} range. As mentioned, the diameter depends on the nucleation time but it depends as well on the temperature. Measurements have indicated that it decreases when using higher temperatures, nonetheless, a significant decrease in crystalline quality also occurs. Consequently, the lowest achieved diameter is around 200 nm, for which a temperature of 970°C was set. Regarding the growth rate, this parameter can be controlled by the carrier gas flow. Higher flows correspond to a lower growth rate. Arguments in favour of this are the larger dwell time of materials and to lower dilution of the main reactants for a lower flow. Finally, the wires reach their maximum height when the top facet changes to a non c-plane orientation. For the microwires used to build the sensors, the parameters during the growth process were set such that the diameter of the wires lies between 1-2 μm and the length is approximately 20μm.

To verify the geometrical aspect of the microwires, scanning electron microscopy was done at the university of Aveiro. The resultant images can be viewed in figure 3.1. For the higher amplification, the hexagonal shape and the indicated sizes can be confirmed. Furthermore we can see that the density of wires on the substrate is very high and it should not be a problem to get a large enough array on a substrate to produce the sensors. The crystalline and structural quality also needs to be confirmed and subsequently X-ray diffraction (XRD) measurements were performed to analyse the crystal structure, chemical composition and physical properties of the material. In an XRD experiment the incident beam

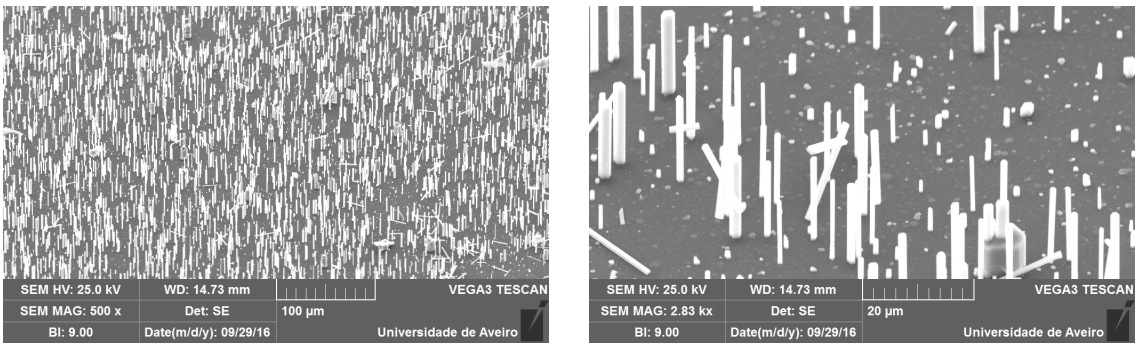

Figure 3.1: SEM images obtained at two different amplification with a substrate tilt of 47°; The amplification on the left hand side is 500× and the amplification on the right hand side is 2830×

with constant wavelength and phase reaches the sample and can be scattered by two different atomic planes within the crystal. Consequently, one scattered beam has to travel a longer path than the other and a phase shift between both is induced. Whether this phase shift is constructive or destructive depends on the distance between the planes and the scattering geometry. The deviation for which the constructive interference is at its strongest is called the Bragg condition. The XRD experiment allows thus the measurement of a scattered X-ray beam that hits the sample in function of the incident and scattered angle and wavelength. The XRD curves were acquired in a Bruker D8 Discover diffractometer

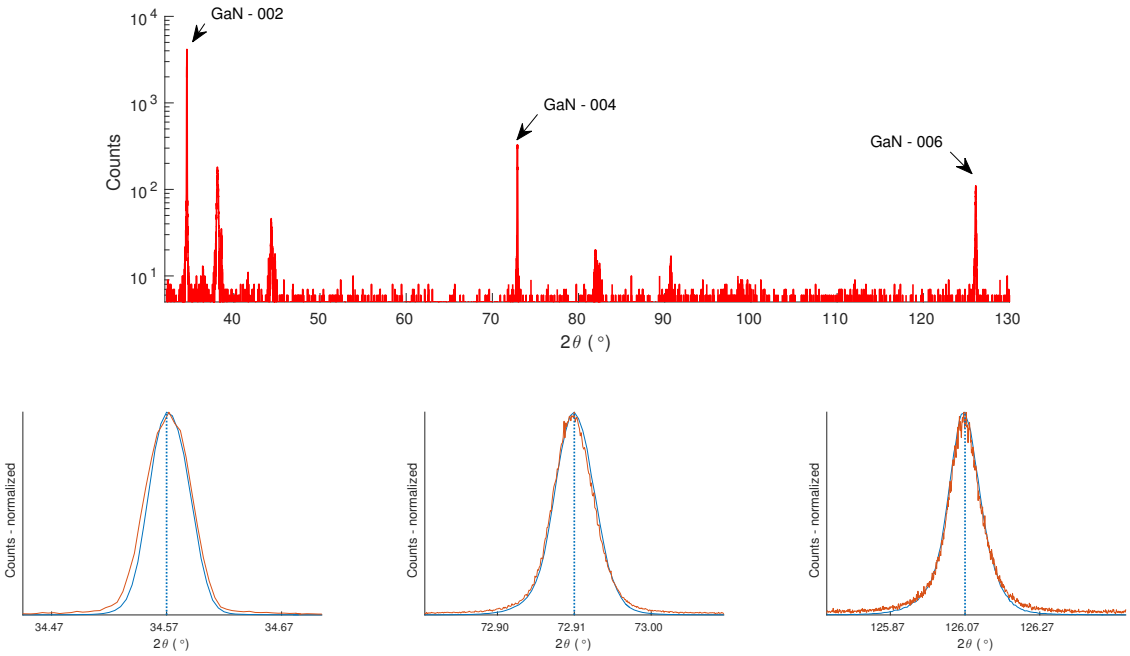

Figure 3.2: X-ray diffraction data for bulk GaN (blue line) and GaN microwires (orange line) with the standard θ-2θ geometry; The left graph corresponds to the 002 reflection, the middle graph to the 004 reflection and the right graph to the 006 reflection

equipped with a Göbel mirror and a (220) germanium monochromator. The radiation $K_{\alpha 1}$ of copper ($\lambda = 1.5405$ Å) is used with a vertical linear focus. Standard 2θ-θ scans aligned with the Bragg reflections were done. A full spectrum was measured as shown in figure 3.2. Since the experiment was aligned for GaN, we can clearly identify the peaks corresponding to the Bragg reflections of GaN to be the ones with the highest intensity. The [002] reflection occurs at $2\theta \sim 34°$, the [004] reflection at $2\theta \sim 73°$ and the [006] reflection at $2\theta \sim 126°$. Additionally, we can see some smaller intensity peaks, some of them correspond to sapphire substrate. For sake of comparison, measurements were also done on a high quality GaN layer. In figures 3.2 we compare the results. As is clear, the FWHM of the peaks are approximately equal for both the layer sample and the microwire sample. The presented measurements confirm that the GaN microwires grow with the typical wurtzite crystal structure. They furthermore reveal the vertical alignment of the microwires on the substrate.

3.2 Fabrication

In order to successfully build radiation sensors with the grown GaN μ-wires we can divide the fabrication process into four main phases: the definition of a grid on the Si substrate, the microwire dispersion, the contact definition and deposition and, finally, the integration of the sensors onto a chip. To achieve satisfactory results the following list of fabrication steps were followed. A schematic of the process can be found in figure 3.3 and the runsheet of these processes is presented in annex A.

1. TiW deposition on Si- 150 Å
2. 1st lithography - grid definition
3. Metal etching
4. Photoresist strip
5. SiO_2 deposition - 2000 Å
6. Microwire dispersion
7. 2nd lithography - contact path definition
8. Cr/Au deposition - 300/4000 Å
9. Metal lift-off
10. Chip dicing
11. Wire-bonding

TiW deposition The idea of creating a grid before proceeding to the actual device fabrication arose due to the difficulty of controlling the position of the deposited microwires, of which the process will be explained later. Therefore, the main function of the grid is to provide a consistent method to locate the wires in terms of coordinates, so it is possible to know exactly where to deposit the metal contacts. The shape of the grid consists of an array of 110μm$\times$110μm squares that, on its own, contain an array of 36 10μm$\times$10μm squares. To define the position of a single wire, a first set of coordinates is determined by the larger squares, and a second set of coordinates is determined by the smaller squares. To build the grid, a 150Å TiW layer was deposited on top of a silicon substrate (fig.3.3(a)) using the Nordiko 7000. This equipment is an ion beam milling system equipped with a radio-frequency (RF) excited ion source. The system consists of a loadlock, which is pumped by a turbo pump that reached pressures of 5×10^{-6} Torr. A mechanical arm transfers the substrate to the dealer chamber, which is surounded by several

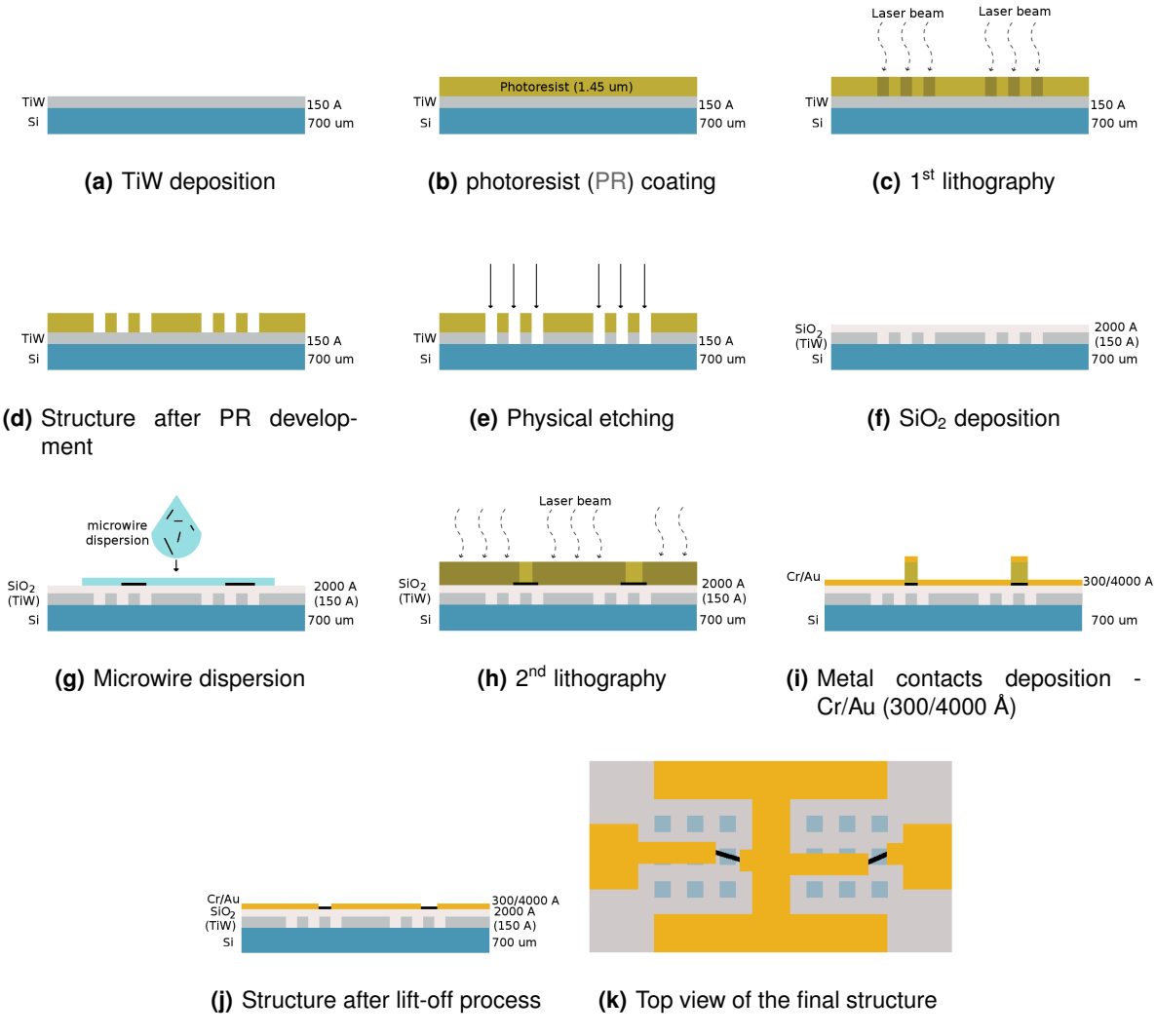

(a) TiW deposition

(b) photoresist (PR) coating

(c) 1st lithography

(d) Structure after PR development

(e) Physical etching

(f) SiO_2 deposition

(g) Microwire dispersion

(h) 2nd lithography

(i) Metal contacts deposition - Cr/Au (300/4000 Å)

(j) Structure after lift-off process

(k) Top view of the final structure

Figure 3.3: Schematic of the fabrication process of the radiation sensors. The dimension are not scaled and the figures are only an indication of the structure.

Module	Power	Voltage	Current	Ar/N_2 flux	Pressure	Dep. rate
3 - DC PVD	0.5 kW	418 V	1.2 A	50/10 sccm	3 mTorr	5.5 Å/s

Table 3.1: N7000 deposition conditions for the TiW layer

modules. Both the dealer chamber and the modules are pumped by cryogenic pumps that can reach pressures down to 5×10^{-9} Torr. The only module used for the metallization step was module 3, in which the TiW is deposited by magnetron sputtering. This process relies on a plasma to deposit material. A gas is injected into the chamber where it is ionized and accelerated towards a TiW target by RF power sources. When the ions hit the target they remove atoms which are directed towards the substrate. The deposition conditions can be found in table 3.1.

1st Photolithography The desired grid pattern was drawn by optical lithography. This is a microfabrication process that allows to transfer a desired pattern onto a substrate to selectively remove or deposit material. The first step in this process consist of coating the sample with a layer of photoresist, a polymer that changes its properties when exposed to light (fig.3.3(b)). Firstly, the substrate is exposed to a vapour prime procedure to improve the adhesion of the photoresist. This is performed in a vapour prime oven where the sample is heated at 130°C and sprayed with hexamethyldisilazane that turns the surface hydrophobic. Afterwards, the coating of photoresist is performed on a Silicon Valley Group (SVG) track. This track has 3 stages, first the photoresist is dispensed on the sample which is spinned at 800 rpm for 5 seconds. Then, the spin frequency is increased to 2500 rpm for 30 seconds in order to obtain the desired 1.5 μm thickness. The coating is finalized with a soft baking process at 85°C for 60 seconds to remove solvents and stress while promoting the adhesion.

With the photoresist in place, a previously designed mask on AutoCAD (see Fig.3.4) that consists of the desired grid pattern is uploaded into a Heidelberg direct write laser (DWL) 2.0 machine. This equipment has a 440 nm NeAr laser that exposes certain areas of the photoresist, according to the created pattern (fig.3.3(c)). The laser can define structures up to 0.8 μm and has an aligment precision of 0.1 μm, which is more than enough to define the 10×10 μm^2 squares. The two main parameters to tune the exposure are the laser's focus and energy. The former controls the distance at which the laser beam is focused relatively to the camera focus while the latter defines the percentage of the laser energy used in the exposure. The used parameters can be found in table 3.2.

At last, when the exposure is finished, a second track on the SVG equipment allows the development of the exposed areas. Firstly the sample is baked at 110°C for 60 seconds to cease any remaining photoresist reactions. Then the sample is cooled again for 30 seconds and development is performed during 60 seconds. As the used photoresist is positive, the areas affected by the light are removed while the unaffected regions remain firmly in place (fig.3.3(d)). If after developing there is still some exposed photoresist remaing the last step in this procedure can be repeated.

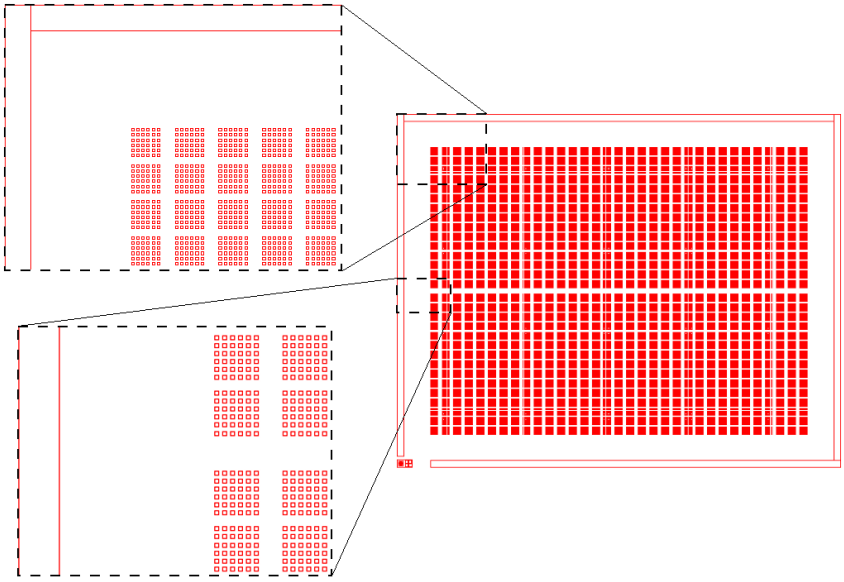

Figure 3.4: AutoCAD drawing for the definition of the microscaled grid

Energy	Laser power	Focus
60 %	90 mW	35

Table 3.2: Photolithography parameters used in 1st lithography

Physical etching With the pattern in place, the sample was placed inside the Nordiko 3600 machine, an ion miling system used, among other things, to perform physical etching (fig.3.3(e)). Just as in the Nordiko 7000, the etching process is done by an ion beam, however, in this case, the beam incites directly on the target removing material that is not covered by the photoresist. The equipment itself, consists of a loadlock, pumped by a mechanical pump, and a larger operation room, pumped by a cryogenic pump, that contains two ion sources, the deposition gun and the assist gun. As the goal is to etch, only the assist gun is activated. The plasma is created by ionizing an argon gas by applying a RF wave. Afterwards the ions are acellerated towards the sample by a set of grids. The etching parameters for this step can de found in table 3.3.

After the etching is done, the remaining photoresist has to be removed. Therefore, the substrate was immersed in a microstrip solution and placed, firstly inside a heatbath at 60°C for rougly 2 hours and, afterwards, in an ultrasound bath also at an temperature of 60°C for another 2 hours.

RF power	$Grid_1$ voltage	$Grid_1$ current	$Grid_2$ voltage	Ar flow	Etching time
192 W	724.3 V	104.3 mA	344.8 V	11.2 sccm	200 s

Table 3.3: N3600 etching parameters

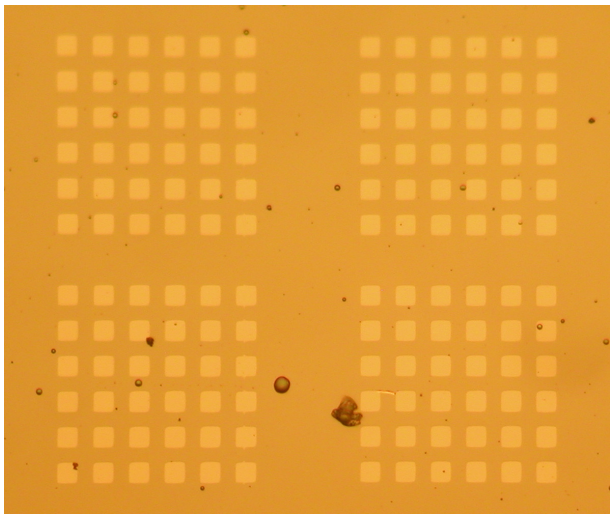

Figure 3.5: The grid viewed in an optical miscroscope with an 20$\times$ amplification. The dimensions of the sides of each square as well as the spaces between each square are 10 μm

RF power	Pressure	Ar flow	Deposition rate
190 W	4.0 mTorr	20 sccm	11.97 Å/min

Table 3.4: Alcatel SCM 450 deposition parameters

SiO_2 deposition To finalize the grid, an isolation layer must be deposited to avoid any contact between the metal and the GaN wires (fig.3.3(f)). A 2000 Å layer of silicon oxide was deposited in the Alcatel SCM 450 sputtering system. This machine is a commercial sputtering tool with one deposition chamber, equipped with three 4 inch diameter magnetron target slots, three shutters and a substrate table. The lack of a loadlock requires that, before each deposition process, the process chamber is pumped to the working pressure of 10^{-7} Torr which takes approximately 12 hours. The main functions of the machine is the deposition of SiO_2, metalization and oxidation. The deposition parameters for this step can be found in table 3.4 and an optical microscopy image of the final grid can be seen in figure 3.5.

Microwire dispersion Two methods have been tested to deposit the GaN microwires. The first, based on a mechanical procedure, consists of sliding a piece of sapphire with microwires grown on top over the substrate grid. The wires showed good adhesion to the SiO_2, however, large irregularities in the deposition existed. Some areas where completely covered with wires while others had none. The second method consists of placing a piece of sapphire with microwires in a isopropyl alcohol (IPA) solution and expose it to an ultrasound bath for 30 minutes. During this time, the microwires are removed from the sapphire substrate and the result is a dispersion of IPA and microwires. A couple of droplets are then extracted and deposited on the device substrate (fig.3.3(g)). Results showed again a good adhesion, but also a much better homogeneity of wires along the substrate. We can conclude therefore that the second method is better relative to the first and should be used in future work. Once the

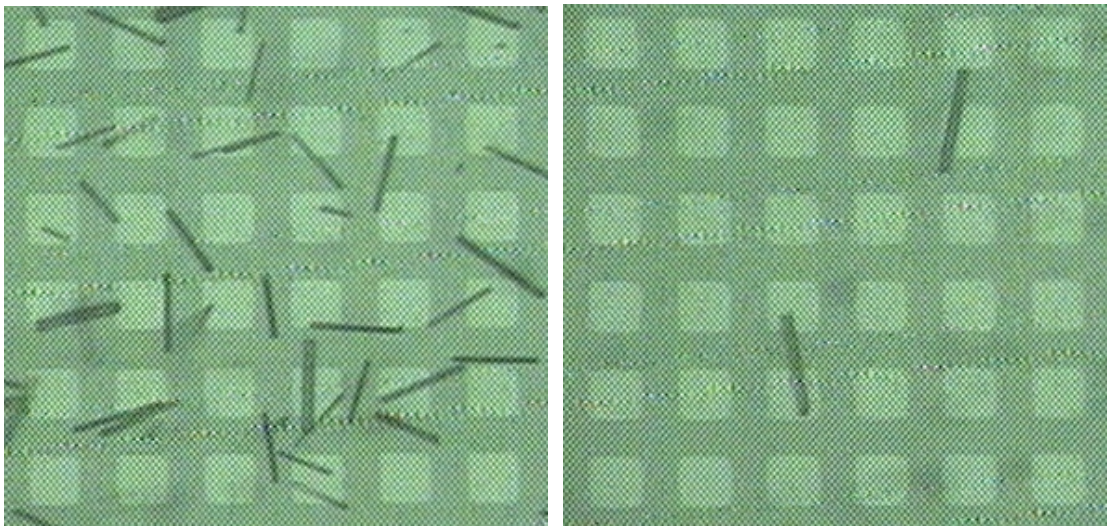

Figure 3.6: Resultant microwire deposition done mechanically (left photo) and by chemical dispersion (right photo)

microwires were dispersed on the substrate, the coordinates of those that had favourable positions were found using the grid, according to the aforementioned methodology.

2nd lithography (fig.3.3(h)) Once the position of the microwires was established, a second mask with the contacts paths was created using the AutoCAD software. For each device, a 60μm$\times$100μm rectangular pad and a central line, 30μm wide, were designed to respectively, apply a bias on and to act as ground. To connect the pad and central spine, 20μm wide paths were drawn. Each path contained a single GaN microwire somewhere in between. The steps followed while performing the 1st photolithography were repeated, however in this case instead of using an etching method to remove the excess of metal we want to use a lift-off process. Consequently a, pre-development step of 20 seconds was included before exposing the photoresist to the laser. This is done to facilitate the removal of the resist after the metalization step. The parameters for this lithography are given in table 3.5.

Metal contacts deposition The next phase of the fabrication process consisted in depositing the metal contacts on the sample (fig.3.3(i)). The materials that were used were chromium and gold. The metals were deposited using the Alcatel SCM 450 equipment, the thickness was defined to be 300 Å and a 4000 Å for Cr and Au, respectively. It is important that the gold layer is thick enough to completely cover the wire in an optimal way. If this is not the case, during the lift-off, all wires would be removed from the

Energy	Laser power	Focus
80 %	85 mW	70

Table 3.5: Photolithography parameters used in 1st lithography

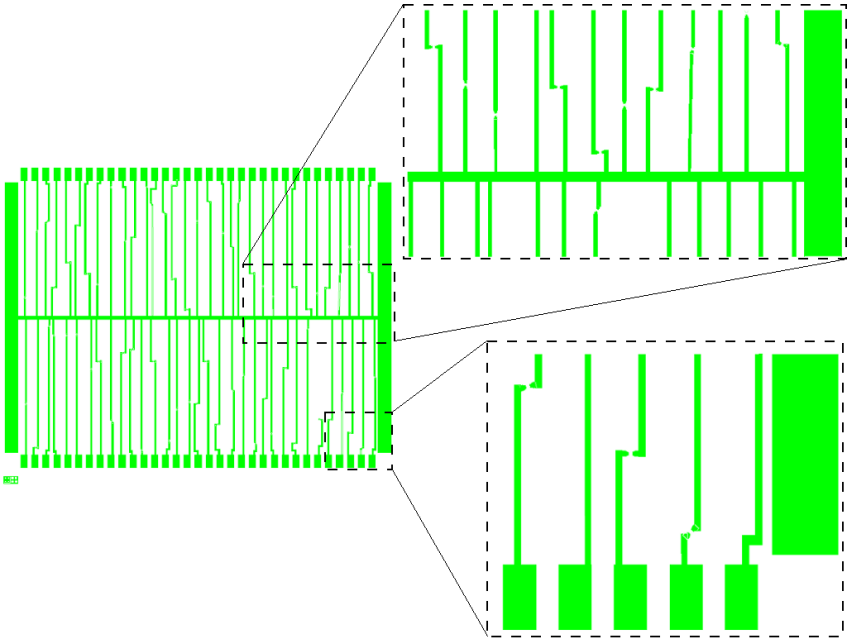

Figure 3.7: AutoCAD drawing for the definition of the contact paths

substrate due to the ultrasonic vibrations. The defined deposition parameters for this step can be found in table 3.6.

RF power	Pressure	Ar flow	Deposition rate
20 W	3.0 mTorr	20 sccm	55.6 Å/min

Table 3.6: Alcatel SCM 450 deposition parameters for Cr/Au contacts

Metal lift-off With the metal deposited, the final step of the contact definition consisted in a lift-off process (fig.3.3(j)). The same procedure as for the photoresist strip, done previously, was followed. The substrate was again immersed in a microstrip solution and placed in a heat bath at 60°C for 3 hours, followed by an ultrasound bath at 60°C during 1 hour and 30 minutes. Before proceeding, an optical inspection was done to see how many good devices were created. It was observed that from the 162 devices that were originally drawn on the CAD mask, more or less 25 showed good connection between the microwire and the metal contacts. In the other devices the contact paths were misaligned or the wires were removed from the substrate during the metal lift-off process. Examples of optical microscopy images of the devices are shwon in figure 3.8.

Integration of sensors on a chip To finalize the fabrication process the samples had to be integrated on a chip. This is not fundamentally needed to perform electrical characterization measurements, however it, is required to perform *in-situ* electrical measurements when exposing the sensors to proton

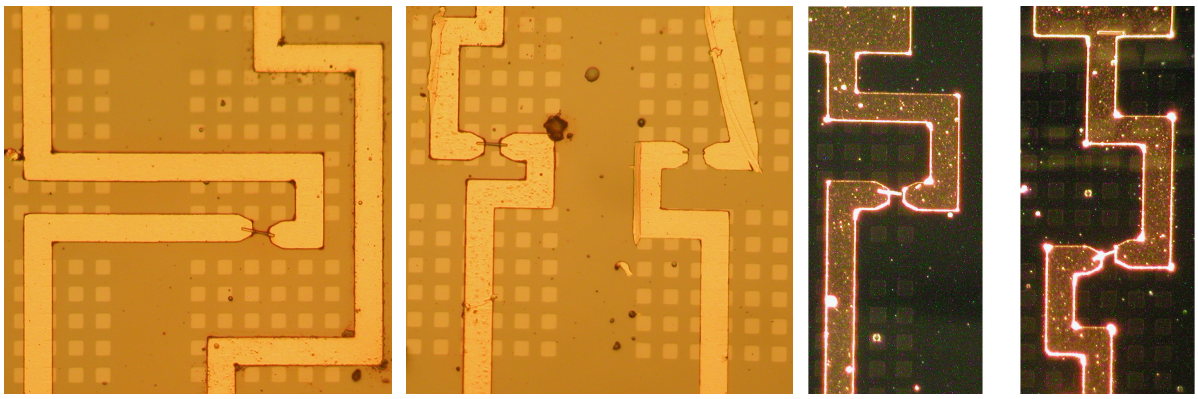

Figure 3.8: Optical microscopy images of devices after the lift-off processes. In some cases the fabrication process was successful (left image) while in others, the wire got removed by the ultrasound treatment (middle image) or the contacts are slightly misaligned (right images).

irradiation. As the samples contained two separate dies with functioning devices, the substrate was diced accordingly. This was done in the Disco DAD 321. To avoid any damage done to the sensors during this process they were firstly covered with a 1.5 μm layer of photoresist. Then, the substrate was mounted on a metallic frame with self-adhesive tape and placed inside the equipment. The Disco DAD 321 has a camera and microscope combination to align the sample, when this is done, the first cut is chosen by the user and the following ones are done automatically, according to the die size. The sample is rotated by 90° and the procedure is repeated. In the end, the protective layer of photoresist is removed with acetone. To integrate the diced dies in a chip a wire bonding process was performed. After being glued to the respective chip carriers, the metal pads as well as the ground line were connected to different pins with 45μm thick aluminum wire. This is done in the K&S 4526 Manual Bonding System, that uses force and ultrasonic vibrations to bond the wire to a surface, a process also known as wedge bonding. There are three parameters that need to be tuned to get proper wire bonds, power, time and force. The power is responsible for the energy of the ultrasonic vibrations, with more power corresponding to a higher frequency of vibrations. The setted time defines how long these vibrations continue and, at last, the force defines the amount of force applied to the bond. A photo of the final device is shown in figure 3.9.

3.3 Characterization methods

Electrical and optoelectrical characterization are fundamental to analyse the behaviour of the sensors and their response to changes in the environment, more specifically, the lighting and radiation conditions. To apply the bias and, simultaneously, measure the current going through the circuit a two-probe configuration is used. The probes are made of Tungsten, the tips and the shanks are 1 μm

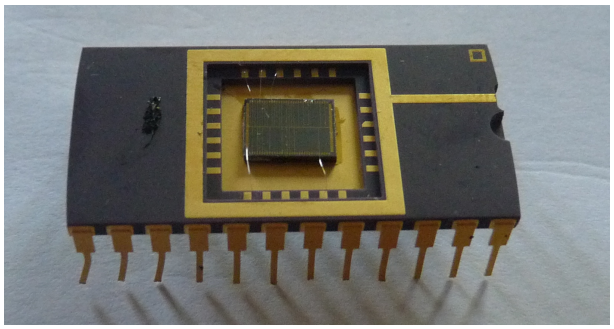

Figure 3.9: The final device integrated on a chip after dicing and wire bonding.

and 0.5 mm thick, respectively. Minor adjustments in their positioning can be made with the aid of two micropositioners. Through a triaxial cable, the probes are connected to Agilent B1511b source measuring units (SMUs). The SMUs are incorporated in an Agilent B1500A Semiconductor Device Analyser. This equipment allows, among others, current-voltage (I-V) measurements among a voltage range from 0.2μV to 200 V and a current range from 0.1 fA to 1 A, and transient IV measurements with a sample rate of 200 MSa/s [72]. To control the relevant parameters and analyse the obtained results the Agilent EasyEXPERT software is used. This setup allows us to perform I-V measurements, which have been a popular characterization method for many years and are perhaps the easiest and most routine measurements performed. Nonetheless, they can provide valuable information about the intrinsic properties of the wires and about the quality of the contacts between the GaN and the metal [73]. To extract quantitative information, the measured $I = I(V)$ will be treated according to the thermionic field emission model. Regarding the I-V experiments, we can perform static and transient I-V measurements. In the former, a bias that sweeps a predefined range is applied and at the same time the output current is measured. In the latter, the applied bias is fixed at a certain value and the output current is measured over time.

Photoconductivity For the photoconductivity measurements a 9 Watt Tungsten halogen lamp, a high brightness deuterium lamp and a high-power UV LED were used. The former two are integrated in the Hamamatsu L10290 and, together, cover a spectral range from 200 nm to 1600 nm. The latter has a dominant wavelength of 365 nm and has a typical power output of 360 mW. The UV LED is powered by a 180 Watt DC power supply. When performing these types of experiments, special care should be taken when aligning and focusing the light with regard to the microwire that is being irradiated, since small misalignments can induce deviations in the obtained results. To facilitate alignment and improve stability, a mechanism has been built to be able to control the light source in the x,y and z directions with a micropositioner.

The changes in the response of a semiconductor when irradiated with light typically consist in a variation of the conductivity and the current under the influence of a light source is called photocurrent. The basic processes that govern the magnitude of this current are the generation of free electrons

and holes through the absorption of incident photons, the transport of those free carriers through the material under influence of an electric field and the recombination of the photoexcited electrons and holes. Since there are three processes involved in the production of the photocurrent, a large set of data from different experiments is required to properly characterize the devices. Two types of experimental techniques are generally used, steady-state photoconductivity (SSPC) and transient photoconductivity (TPC). The former deals with stationary photocurrent levels while the latter studies the time evolution of the photocurrent [73]. In this work, the photoconductive properties of the GaN wires were analysed with two SSPC experimental techniques, photoconductivity spectroscopy and steady state I-V measurements and one TPC experimental technique, consisting of transient I-V measurements.

The photoconductivity spectroscopy (PCS) consists in measuring the dependence of the photoconductivity on the excitation energy. This experiment is very useful to analyse the bandgap structure and possible defect states in the forbidden region of a semiconductor. Since we want to measure the current dependence on the excitation wavelength, we want the largest possible spectral distribution, therefore both the halogen and deuterium lamp were used simultaneously. The input light goes through a monochromator, an optical device that transmits a narrow band of wavelengths chosen from a wider range of wavelengths available at the input. The input light firstly goes through an entrance slit and is aligned by a set of mirrors. Then it gets dispersed by a diffraction grating. This element has a surface specifically designed to disperse different wavelengths of light at slightly different angles. A second set of mirrors aligns the beam with another slit such that only a narrow band of wavelengths can go through, while the others get blocked. In this way, the output light can be attributed to a single wavelength.

Regarding the experimental conditions, all measurements were done at room temperature. Relative to experimental parameters, we can control the base time, wait time and the step in wavelength. The base time is the time the light source is off between subsequent measurements and the wait time is the time between the moment the light is turned on and the moment that the current measurement is done. The best setup would be to have the smallest possible step with the shortest times associated. However, it is important that two subsequent measurements are independent, *i.e*, that a measurement in current at λ_{n+1} is not affected by the measurement at λ_n. Therefore, a base time of the order of a minute is necessary. On the other hand, the time it takes the photocurrent to reach a stable magnitude is approximately 20 seconds, therefore when performing each measurement a wait time of at least 20 seconds is required and a measurement for a particular wavelength takes around 2 minutes. Consequently, for practical reasons the defined step size is typically between 2 and 0.5 nm, depending on the spectral range we want to measure.

To perform I-V measurements, the tungsten probes were positioned on the respective pads and the light source was placed above the sensors, at a height at which the focus was optimal. For the static IV measurements, the parameters that need to be set are the bias range and the current compliance.

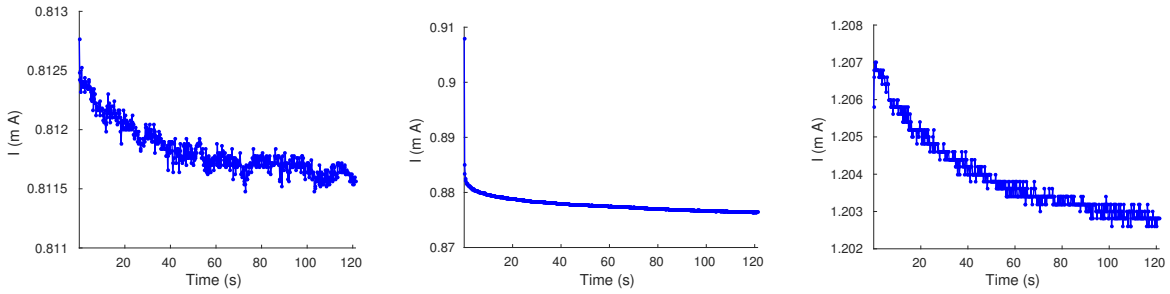

Figure 3.10: The initial current peak that appears when initializing an I-V measurement for the 210U (left), the 216U (center) and the 229U (right) devices. It takes approximately two minutes for the current to stabilize.

As we do not want to disrupt the sensors, the maximum values used where [-10 V,10 V] for the former and 2 mA for the latter. The number of points was fixed at 1001 for each IV curve, thus the bias step size changes according to the defined range. To obtain a large amount of data regarding the photoconductivity, measurements were done in dark environment and while illuminating the sensors with the different light sources. Special care should be taken when performing subsequent measurements as the devices take some time to recover their stable dark current. For example, if we want to measure the I-V characteristic of a device in the dark and with the three light sources, it is useful to perform the measurements from the least energetic and lowest power output source (IR), that yields the lowest current, to the most energetic and highest power output source (UV), that yields the highest current. Like this, the influence of the decay time of the photocurrent can be ignored. Finally, as can be seen in the shown transient I-V graphs in figure 3.10, when a bias is applied on the sensors a sudden initial increase or decrease in current occurs, followed by a more slowly decay or rise. As this instability is not consistent, a time interval between the application of the bias and the actual current measurement is needed to avoid unwanted errors.

Regarding the transient measurements, the only experimental parameter that needs to be set is the applied bias. The experiment itself consists in turning the light on and off during the measurement, to analyse the variation in current under different kinds of illumination. Two separate situations were tested, the first consists in turning on the light and leaving it on for some time before shutting it down so the photocurrent can reach stable values. After this time period we leave the experiment run for approximately 30 minutes in order to measure the decay time of the current with precision. In the second experiment, the light source is turned on and off several times. This allows the calculation of the rise time of the current and provides information on the reproducibility of the current behaviour.

The obvious difference between the turn-on and turn-off situation in a transient measurement is that the former reflects interplay between generation and recombination of carriers, while the latter only involves recombination. If the recombination only follows a unique path, the decay will be a simple exponential. Nonetheless, this is more often an exception rather than the rule as surface states and

deep traps create more possibilities for an electron and a hole to recombine [73]. The measurements will subsequently, in addition to the study of the photodectective capabilities of the sensors, allow more thorough analysis of the materials properties.

3.4 Proton-irradiation

One of the most important spearheads of this investigation is to study the response of the sensors when subjected to ionizing radiation. The experiments regarding this section were performed at the nuclear microprobe facilities at CTN (Campus Tecnológico Nuclear). The beam is generated in a 2.5 MV Van de Graaff accelerator and travels through a beam line that contain two stabilizing slits and a bending magnet before reaching the microprobe line. Two sets of micrometer driven slits are used to define the size of the object aperture and collimator. The object aperture has a steering magnet placed closely in front of it to optimise the flux of particles that reach the collimator. This slit will define the divergence of the beam into a high excitation magnetic quadropole triplet lens system, which will focus the beam. Focus down to an area of 3 $\times$ 4 μm^2 can be reached [74].

To perform the actual experiment, the samples to be irradiated were attached to a sample holder, which is placed in the microprobe chamber. A turbo pump then is turned on to create a vacuum inside the chamber, pressures down to $10^{-5} - 10^{-6}$ mbar are established. Once satisfactory pressure conditions are reached the beam alignment starts. As the samples did not show any visible luminescence the alignment was performed with the aid of PIXE maps. PIXE stands for proton-induced X-ray emission and is a technique used in the determination of the elemental make-up of a material or sample. It is a non-destructive technique based on the emission of X-rays resulting from the transition of outer shell electrons to inner shell vacancies, which appear when inner shell ionization of atoms occur due to irradiation. As each element emits X-rays of a characteristic energy, an elemental map can be drawn of the sample or device under analysis. Examples of PIXE maps obtained for the irradiation of the devices are shown in figure 3.11. The alignment of the beam can be done by simply selecting the area of interest on such a map. If, for example, we want to irradiate the wire, we select an area defined by the green rectangle and the beam gets focussed on that specific area. With all the experimental conditions properly set, the beam was directed towards the sample. The incidence area and current of the beam were set according to the type of measurements that were done. Typically, the beam current was set between 1 nA and 300 pA while the irradiated area ranged from 25 $\times$ 25 μm^2 to 15 $\times$ 15 μm^2. This corresponds to a fluence of $\sim 1 \times 10^{15}$ protons/cm^{2}s.

The main goals of the measurements are to analyse, as mentioned, how the wires react to the high energy radiation in terms of current but as well to see how the wires are affected in terms of defect creation. To get predictions on the irradiation depth, *i.e.*, how far the protons travel when entering the

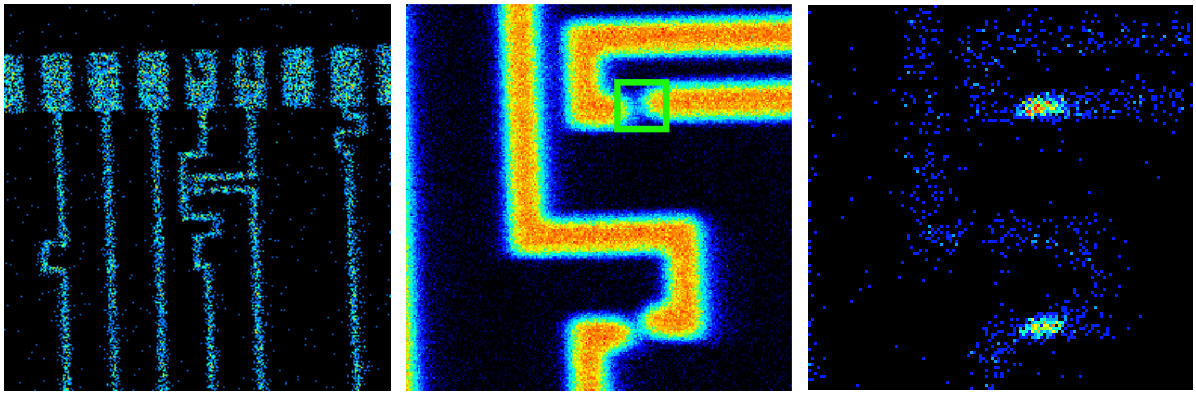

Figure 3.11: PIXE elemental maps for Au (left and center) and Ga (right). The alignment of the beam can be done by locating the microwires and selecting the area, represented by the green rectangle, that we want to irradiate.

GaN wires, and what kind of alterations they cause, a stopping and range of ions in matter (SRIM) Monte Carlo simulation was performed [75]. The simulation was done for 2 MeV H^+ protons and a planar target of GaN with a thickness of 50 μm. Although this does not reflect the 3D geometry of the wires it will give important estimations of ion range and ion-matter interactions in GaN. The obtained results are depicted in figure 3.12.

The depth profile and the ion distribution results indicate that, for an energy of 2 MeV, the protons easily go through the microwires. Most of the protons stop at approximately 25 μm into the target, which is much larger than the diameter of the wires and we can safely assume that no hydrogen implantation occurs. Furthermore, the ionization calculations indicate that for the first two 2 μm it can be considered constant. This allows us to conclude that, when we irradiate our wires with protons, the ionization profile will be constant across the entire microwire. Finally, the plot relative to the collision events, shows that there will be some damage creation, but since the protons cross the wires, the number of created defects will not be large.

Rapid Thermal Annealing As demonstrated, the ionizing radiation will induce defects in the material that affect the overall behaviour of the devices. A rapid thermal annealing (RTA) process can be applied to recover some of the created defects. The RTA machine available at CTN is a ANNEALSYS AS-One 100 rapid thermal annealing processor. Simply put, the system can be divided into two parts: the reactor and associated circuits, that includes among others the process chamber, furnace and cooling circuit, and the control rack which contains several control circuits. The heating is done by halogen lamps, installed above the process chamber. It heats the substrate through a quartz window mainly via infrared radiation. A thermocouple and an optical pyrometer measure and control the temperature inside the process chamber. The system is prepared to reach maximum temperatures of 1500°C for a period

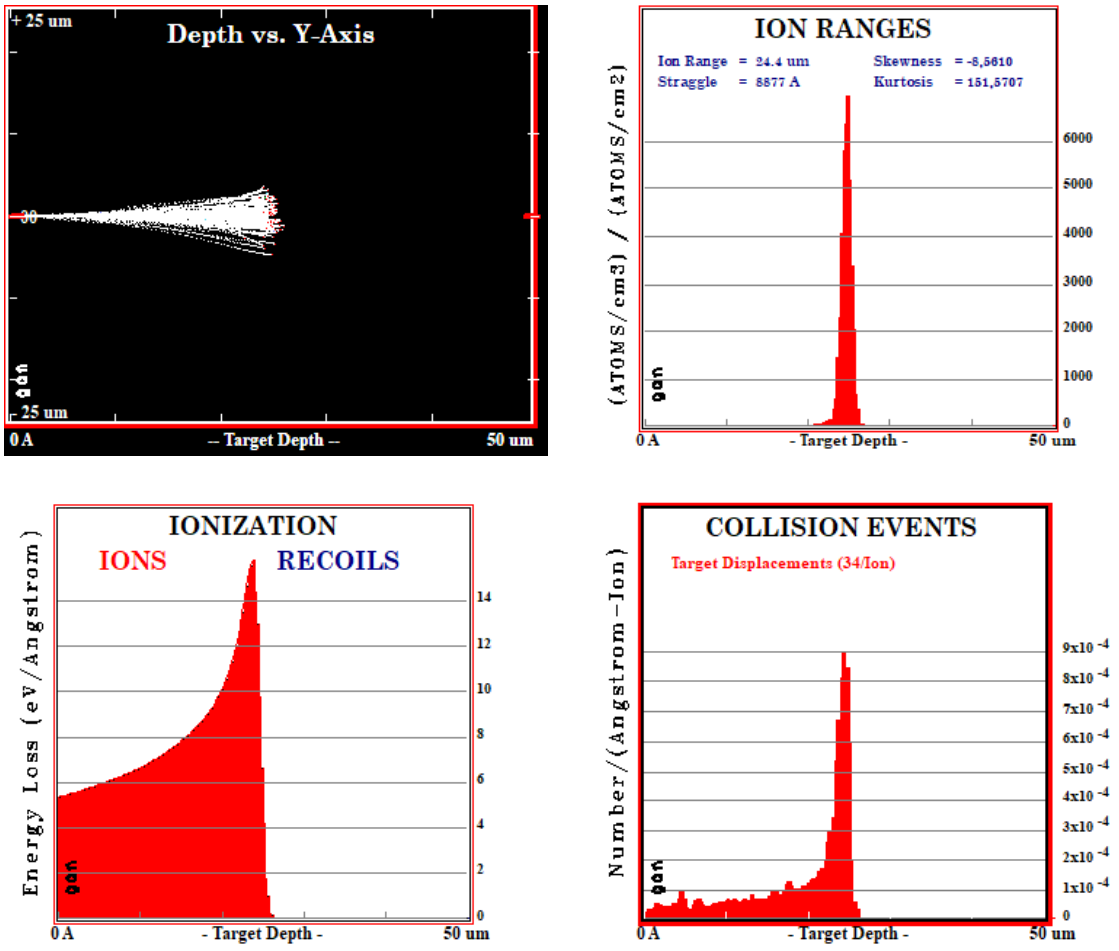

Figure 3.12: The obtained results for a SRIM simulation with 2 MeV H^+ protons hitting a planar GaN target of thickness equal to 50 μm. The top left graph shows the path for a number of protons that enter the GaN. The top right graph plots the concentration of hydrogen atoms versus the target depth. The bottom left graph shows the energy loss due to ionization versus the target depth. The bottom right graph shows how many displacements occur versus target depth.

of 30 seconds, it can hold lower temperatures for a longer time interval though. In the case of GaN however, it is not advisable to anneal at temperatures superior to 1000°C as the material will start to decompose. For the annealing of the irradiated wires, a recipe consisting of the following steps was elaborated. First, the process chamber gets pumped down to a pressure of 5×10^{-5} mbar to afterwards be filled with nitrogen. Then, the temperature gets increased at 100% power until it reaches 300°C, when this temperature is reached, the ramping increase starts with a rate of 30°C/s until the chosen maximum temperature is reached. This temperature is maintained for a chosen time interval and, finally, the power is shut off and the process chamber cools down to room temperature.

4

Experimental Results

Contents

4.1 Electrical characterization 45

4.2 Photoconductivity 49

4.3 Proton-irradiation 57

4.1 Electrical characterization

The first step in the experimental procedure consisted in verifying if and how the sensors responded when applying a bias. Therefore, simple I-V curves in a dark environment were taken using the Agilent analyser. The obtained results showed that not all fabricated devices yielded the same response curve. Simply put, we can divide the results into four types of curves: almost linear (fig.4.1(a)), almost symmetric(fig.4.1(b)), asymmetric(fig.4.1(c)) and rectifying(fig.4.1(d)). The most commonly obtained curves were almost symmetric or asymmetric. From the 23 working devices, 18 yielded one of these types of responses, 3 yielded linear responses and 2 yielded rectifying curves. This makes sense considering the inhomogeneous doping concentration along the microwire axis. Since the depletion region at a metal-semiconductor interface is proportional to the inverse square root of N_d (see eq.2.3), it will be smaller at the extremity of the wire that is heavily doped comparatively to the extremity of the wire that has a lower doping concentration. Thus, when the former Schottky contact is in reverse bias, the electron tunnelling probability will be higher than when the latter Schottky contact is in reverse bias, which yields an asymmetric I-V curve. Furthermore, the fact that we obtained different I-V characteristics for devices that were fabricated in exactly the same way, can be explained taking into account that, in general, the conductivity of an MSM circuit depends on various parameters which can not always be controlled during the growth and fabrication process. Some parameters that can vary are intrinsic to the wires, like the wire resistivity, geometry, doping concentration and carrier mobility. On the other hand, during the fabrication of the contacts, unavoidable processes occur when the metal-semiconductor interface is formed, like gas molecules absorbed at the wire surface and defects that produce disorder and localized charges. Additionally, due to the small size of the wires and the applied fabrication method, it is not possible to decently control the contact area. Consequently some junctions may have larger metal-semiconductor interfaces than others. If we add this all up together, devices that were build in the same batch can present different responses when applying a bias.

Just by looking at the overall response of the devices there are two statements we can make. Firstly, the devices present high dark conductivity and, secondly, the presence of a potential Schottky barrier at the big majority of the contacts prevents linear I-V curves. Regarding the former statement, most devices reach currents of 2 mA for a bias well below 5 Volts. This can be attributed to the partial high donor concentration in the microwires as a result of the growth process. As mentioned, the bottom section of the MOCVD grown wires have an N_d in the 10^{19} - 10^{20} cm^{-3} range and the upper section in the 10^{17} - 10^{18} cm^{-3} range. The Fermi energy of GaN for such donor concentrations should lie very close or even above the conduction band [70]. Microwires grown by an identical process, but with an homogeneous doping concentration ($N_d = 10^{20}$ cm^{-3}) along the wire axis were also studied by Tchoulfian *et al.* [76] and they also reported a very high conductivity. Their devices showed linear I-V curves however, whereas ours do not, as can be seen from the I-V characteristics. The metals that

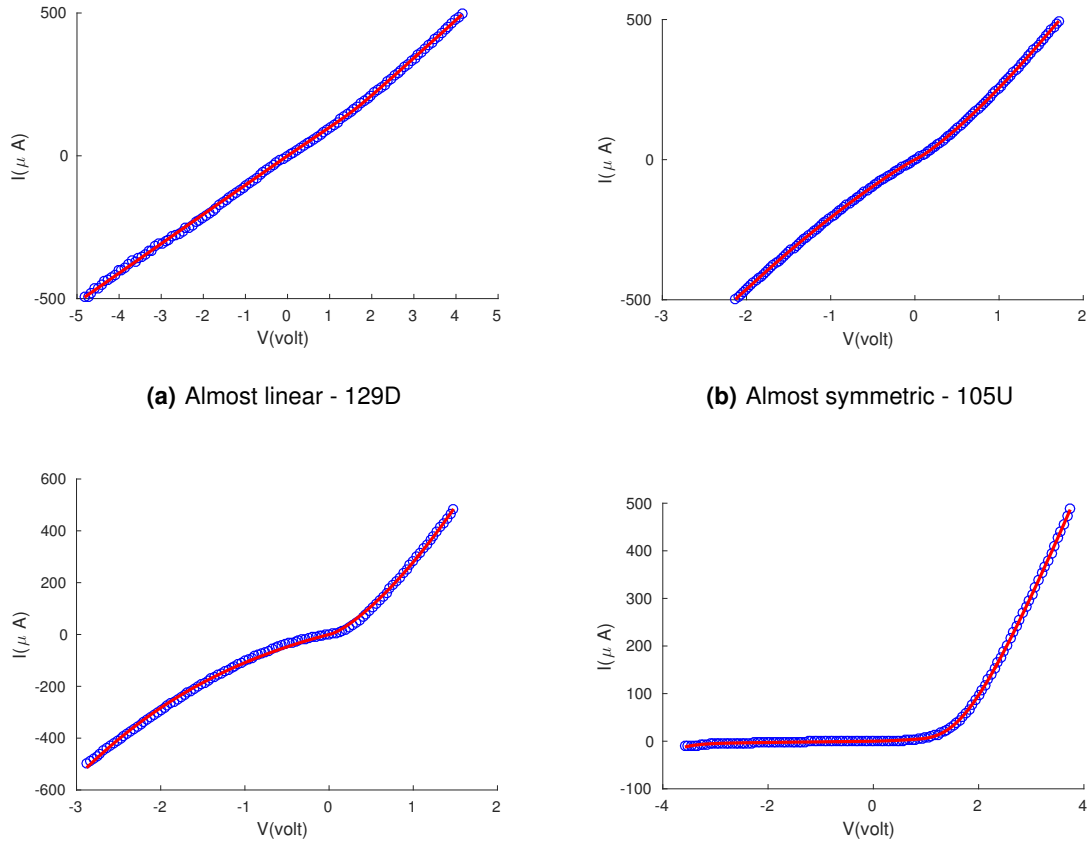

(a) Almost linear - 129D

(b) Almost symmetric - 105U

(c) Asymmetric - 216U

(d) Rectifying - 326D

Figure 4.1: Experimental I-V characteristics obtained when applying a bias from -5V to 5V with a current compliance of 500 μA. The blue circles correspond to the experimental data and the red lines correspond to the fit results.

were used for the contact deposition were Titanium and Aluminium of which the metal work functions are lower comparatively to Chromium and Gold. Nonetheless, this should not have a major influence as the barrier height between the metal and semiconductor is more likely to be defined by the surface states potential [41, 42]. In fact, a report on Cr/Au metal contacts on GaN showed that they can achieve very low contact resistance at a doping concentration of 10^{18} cm^{-3} [77]. Furthermore, the existence of an insulating layer involving the microwire is likely to influence the electric behaviour. In future work, an etching step can be included in the fabrication process before depositing the metal contacts, to remove this insulating layer. To try to obtain more reproducible I-V characteristics, RTA was performed at a temperature of 400° for 60 seconds. As a result most I-V curves that were almost symmetric became asymmetric as well.

As we have non linear contacts, we can assume a back-to-back Schottky configuration and since doping is significant, we suspect that the electron transport is done through a mix of field emission and

thermionic field emission. With this knowledge, we decided to treat the obtained data with a program developed by Liu *et al.* [78]. This program was specially developed to perform fits on I-V curves obtained from MSM nanostructure devices. From these fits, the Schottky barrier heights, the wire resistance, the carrier density and other defining parameters can be extracted. The model is based on the MSM structure as depicted in figure 2.5 and uses the current density equation of thermionic field emission to describe the current going through the reverse biased barrier, while applying the thermionic emission equation to describe the current that goes through the forward barrier. The strong point of the model is that its analysis of the current densities are based on the voltage drop in each segment. If we apply a voltage V on one contact and ground the other, we can write the following equation

$$V = V_1 + V_{mw} + V_2 \tag{4.1}$$

Where V_1 and V_2 represent the voltage drops on each contact V_{mw} the voltage drop in the MW. Assuming the Schottky barrier 2 is in forward bias and the Schottky barrier 1 in reverse bias, we can write

$$I_1 = A_1 J_{TFE}(V_1) + V_1/R_{sh_1} \tag{4.2}$$

$$I_2 = A_2 J_{TE}(V_2) + V_2/R_{sh_2} \tag{4.3}$$

Where J_{TE} and J_{TFE} are respectively given by eq.2.5 and eq.2.6, $A_{1,2}$ are the respective contact areas and $R_{sh_{1,2}}$ the shunt resistances associated with the Schottky barriers. We can also write the current that goes through the microwire as $I_{mw} = V_{mw}/R_{mw}$. As Kirchoff's current law states that the algebraic sum of currents in a network of conductors meeting at a point is zero, we have $I_1 = I_2 = I_W$. If we put this in a system we obtain

$$\begin{cases} A_1 J_{TFE}(V_1) + V_1/R_{sh_1} = (V - V_1 - V_2)/R_{mw} \\ A_2 J_{TE}(V_2) + V_2/R_{sh_2} = (V - V_1 - V_2)/R_{mw} \end{cases} \tag{4.4}$$

To extract the voltage distributions over V_1, V_2 and V_{mw}, the model solves this equation numerically applying Newton's method. A full description of the model can be found in the following references [78, 79].

The curves of figure 4.1 were fitted and the obtained results are shown in table 4.1. The model has proven to work for a different set of nanostructures and it properly fits our data. The obtained results for the barrier heights in the case of samples 105U, 216U and 326D are in agreement with the almost symmetric, asymmetric and rectifying curves that were obtained for each sample, respectively. Regarding the doping concentration, the model considers a constant and average value for the whole wire and the returned results are in line with the concentration of the moderately doped section. As mentioned, the model calculates the parameters by considering the voltage drops in each segment. If

Parameters	129D	105U	216U	326D
ϕ_1 (eV)	0.11 ± 0.05	0.2199 ± 0.0003	0.210 ± 0.001	0.436 ± 0.002
ϕ_2 (eV)	0.189 ± 0.005	0.2469 ± 0.0003	0.267 ± 0.03	0.794 ± 0.007
E_0 (meV)	26.3 ± 0.1	26.123 ± 0.001	26.23 ± 0.02	28.52 ± 0.05
E_{00} (meV)	5.7 ± 0.7	4.51 ± 0.01	5.4 ± 0.2	14.5 ± 0.1
R (kΩ)	8.5 ± 0.2	0.909 ± 0.001	0.94 ± 0.06	3.43 ± 0.01
N_d ($\times 10^{17}$ cm^{-3})	1.7 ± 0.4	1.050 ± 0.006	1.50 ± 0.09	10.9 ± 0.2
σ ($\times 10^4$ S/m)	0.313 ± 0.07	2.78 ± 0.04	2.9 ± 0.2	0.741 ± 0.03
μ ($\times 10^4$ cm^2/(V.s))	0.12 ± 0.03	1.66 ± 0.02	1.12 ± 0.09	0.426 ± 0.08

Table 4.1: Fit parameters obtained from the data curves shown in fig.4.1

we plot the voltage drops calculated by the program against the applied bias, presented in figure 4.2 for sample 216U, we clearly see that for negative bias, *i.e.* when the higher barrier contact is in reverse, the voltage drop at the Schottky barrier dominates. On the other hand, for positive bias, *i.e.* when the lower barrier contact is in reverse, the voltage drop due to the microwire resistance dominates for $V > 2$ volt.

However, despite the good qualitative agreement between the data and fit, the largely differing values for the parameters describing the wires suggests that the model may not properly distinguish between the different sections of the device. Although the differences may also be due to distinct properties of single wires, ambiguities of the fiting model were revealed when comparing I-V measurements done under different radiation conditions. Since the gain in current when the device is excited by photons or protons is relatively small, as will be shown in the next section, the model cannot distinguish if the variation is a result of a change in the resistance of the wire or the lowering of the Schottky barriers. To overcome this ambiguity, we decided to use the model solely to analyse the resistance of the wire which can be done by focusing on the linear segment of the I-V curve at high voltages. In this range the voltage drop at the microwire dominates, as can be seen in figure 4.2, making the effect of the Schottky junctions on the I-V characteristics relatively small. This might still give us incorrect values

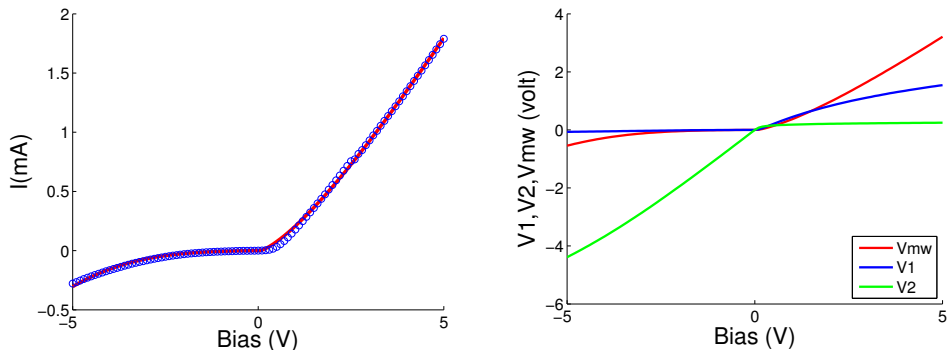

Figure 4.2: Voltage drops at the lower Schottky barrier (V_1), the higher Schottky barrier (V_2) and the microwire (V_{mw}) as calculated by the program (right graph) for the fit corresponding to sample 216U (left graph). As can be seen, for positive and high bias, the voltage drop in the microwire dominates and is approximately linear, which tells us that it is mostly dependent on R_{mw}

for the resistance in the microwire, but provides a consistent method to compare the information of the I-V characteristics obtained under different lighting or irradiation conditions. Note that in the forthcoming results, the measurements were done in such a way that the linear region, and thus the high conductivity regime, correspond at all times to the positive bias.

4.2 Photoconductivity

4.2.1 Spectroscopy (PCS)

As mentioned earlier, the principal objective of photoconductivity measurements is to evaluate the potential of the devices to detect light of different wavelengths and probe the different electronic transitions that contribute to the photocurrent. Several spectra were measured and Figure 4.3 shows an obtained spectrum using the experimental parameters presented in table 4.2.

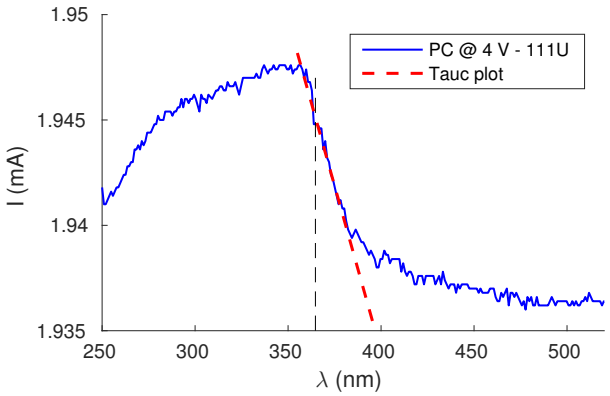

Figure 4.3: The photoconductivity spectrum obtained with a 4V bias for the 111U device. The red dotted line represents the fit of the linear region in the absorption and the black dotted line represents the reported bandgap of 3.4 eV The spectrum has not been corrected.

Initial λ	Final λ	Step	Base time	Wait time
600 nm	320 nm	1.5 nm	120 s	120 s

Table 4.2: Experimental parameters used for the PCS measurement shown in fig.4.3

If we take a look at the general shape of the PCS and analyse it qualitatively, we can see that it follows the expected behaviour. The photocurrent is low for excitation below the bandgap and absorption increases for wavelengths close to the bandgap. The physical explanation for these occurrences are straight forward, since the bandgap of GaN is wide, incident radiation with energy well below E_g will not generate any excess carriers as the electrons do not receive sufficient energy to make the transition from the valence to the conduction band. When the energy of the radiation increases to values closer to E_g, the higher energy states in the conduction band become available and electrons start to occupy them,

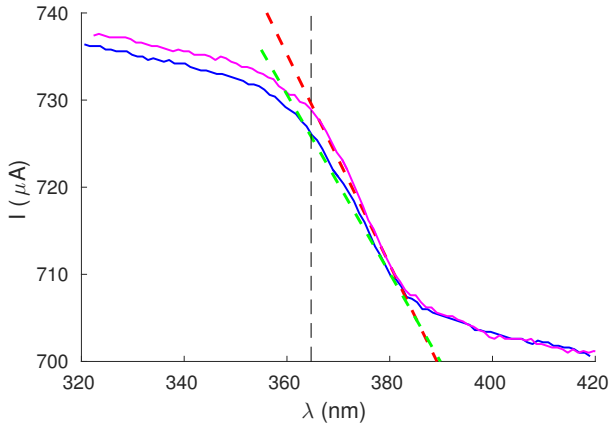

Figure 4.4: The photoconductivity spectrum obtained with a 2V bias for the 105U device. The magent and blue line represent a PC measurement under the same conditions, we can see that there is good coherence between both. The red and green line represent the corresponding Tauc plots and the vertical line marks the GaN bandgap of 3.4 eV. The spectrum has not been corrected.

creating an excess of electrons and, consequently, the current increases. Although these observations are obvious, they give strong evidence that, generally speaking, the devices work as expected regarding their absorption capacities. If we make a more quantitative evaluation, additional relevant information can be extracted. First of all, a slowly increasing sub bandgap tail is visible for wavelengths up to approximately 470 nm. At around 400 nm the current starts to increase more significantly, indicating that at this point the material becomes more sensitive to the incident photons. The maximum current is reached at a wavelength of 357 nm, which corresponds to an energy of 3.47 eV. If we perform a linear regression to the linear range of the spectrum, according to the Tauc method [80], we can estimate the initial wavelength at which the biggest portion of absorption occurs. The results yielded $\lambda = 395 \pm 13$nm which corresponds to an energy $E = 3.1 \pm 0.1$ eV, which is lower than the typical value of the GaN bandgap. If we subtract the wavelength at which the current saturates from this value, we can estimate the width of the absorption band to be of the order of hundred meV. We note that the obtained spectra were not corrected for the intensity of the exciting light.

In order to obtain a more detailed result in the defining region, *i.e.*, the range at which the main absorption occurs, two spectra with the 105U device were measured between 420 and 320 nm. Except for the range and wavelength step, the experimental conditions were kept constant. The curves are shown in figure 4.4. In this case a first small increase in the photocurrent, corresponding to the bandgap tail, occurs at a wavelength of 420 nm (2.92 eV). From the Tauc plots the values $\lambda = 388 \pm 8$ nm (3.20 ± 0.07) and $\lambda = 393 \pm 9$ nm (3.16 ± 0.07) were extracted regarding the blue and magenta curve respectively, as the wavelengths at which the band-to-band absorption begins. The wavelength at which the absorption saturates is approximately 352 nm (3.52 eV). This yields a bandwidth of $\Delta E = 0.33 \pm 0.07$ eV, and $\Delta E = 0.37 \pm 0.07$ eV, respectively. Note that the conversion from wavelength to energy

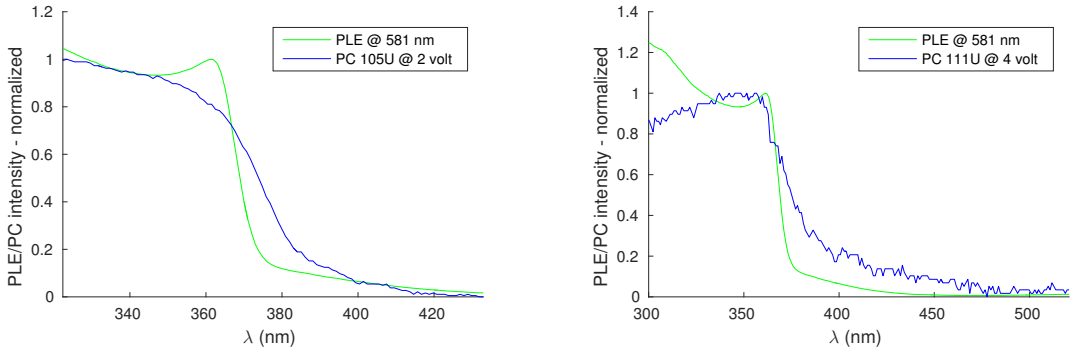

Figure 4.5: The normalized photoconductivity (blue) spectrum and photoluminescence excitation spectrum (green)

was done by applying $E(\text{eV}) = 1240/\lambda(\text{nm})$.

The measurements for the 105U sample were done consecutively, so the alignment of the beam was equal. The results obtained for the different devices indicate that, apart from minor shifts in the spectrum, there exists a good reproducibility and coherence between the data.

The obtained results are compared with a photoluminescence excitation (PLE) of an assemble of the same microwires before detaching them from the substrate, as can be seen in figure 4.5. The biggest difference between both curves is the width of the absorption region. In the case of the PLE spectrum the most significant absorption occurs between $\lambda = 372 \pm 9$ (3.33 ± 0.08), obtained by the Tauc fit and 361 nm, which correponds to the wavelength the absorption reaches its maximum value. This corresponds to $\Delta E = 0.10 \pm 0.08$ eV. The large relative error indicates that this value is merely an estimation but, nevertheless the bandwidth corresponds to only little more than a third of the ΔE obtained for the PCS measurements. A plausible reason for the deviations between PCS and PLE is that PLE was done on as-grown samples while the PCS measurements were done on wires that suffered a lot of processing steps. This likely created additional defects at the surface. On the other hand we are also dealing with different experiments. Whereas the photoconductivity is a direct result of the generation of electron-hole pairs due to absorption of an excitation beam at a given wavelength, PLE measures light emission at a singular wavelength, when the sample is excited by a spectrum of wavelengths and is thus dependent on the population mechanisms of optically active levels. In this sense, PCS measurements are sensitive to both radiative and non-radiative transitions whereas luminescence is only sensitive to radiative transitions [81]. In this case, the emission of the PLE was measured at a wavelength of 581 nm. This wavelength corresponds to the yellow band emission of GaN, which is correlated to a deep level located 2.3 eV below the conduction band [82]. We can see that in the case of PLE, the spectrum shows a well defined absorption edge, which indicates that there is a preferential excitation mechanism. On the other hand, the edge is not so well defined in the PCS spectra which tells us that there might be several excitation mechanisms. Nonetheless, the spectra also show similarities, like the absorption for energies below the

E_g which can be identified by the sub bandgap tail. The existence may reflect the typical Urbach edge which can be caused by perturbations due to defects [83]. When these defect levels contain trapped holes or electrons and are excited by photons, excess carriers can be generated. Since the levels are localized somewhere in between the valence and conduction band, the energy of excitation is lower than E_g [54]. The presence of defect states in GaN has been thoroughly studied, however, there are still discussions about which might contribute to the PC generation. Nonetheless, PCS measurements on GaN have indicated a strong influence of a deep acceptor level, located approximately 140 meV above the valence band, and a deep donor level located at about 1 eV below the conduction band. These deep levels can be correlated to gallium vacancies and interstitials respectively [55]. The importance of the defect states in the generation and recombination processes will be more extensively treated when analysing the PPC, since they are also closely correlated with this phenomenon.

Furthermore, if we take into account the high doping concentration we can predict the existence of the Burstein-Moss effect (BME) [84, 85] and bandgap renormalization (BGR) [86]. The BME effect is commonly observed in degenerate semiconductors and causes a blue-shift in the optical absorption edge and was readily observed during a low temperature cathodoluminescence study after the fabrication of the wires used in this work [70]. The BGR on the contrary causes a red-shift by lowering the energy difference between the bottom of the conduction band and the top of the valence band. The interplay between both mentioned effects has been reported previously for heavy doped GaN films [87] and nanowires [88] and their existence complicate the interpretation of our results. However, as we solely wanted to confirm the absorption of GaN in the UV range and the blindness to visible light no further measurements were done to quantify these effects.

4.2.2 I-V characterization

As follow up to the photoconductivity spectroscopy, an extensive analysis of the I-V characteristics of three selected devices, 210U, 216U and 229U, was performed. Measurements without lighting (dark), with visible light from the tungsten lamp and with both the deuterium and LED UV sources were done between -10 and 5 volts, using a current compliance of 2 mA. The obtained results are shown in figure 4.6. A response, although small, translated in an increase of the current can be observed, even for the tungsten lamp. This is not surprising though as the spectrum for a typical tungsten includes a small emission in the UV range. From the used light sources, the high-power LED yielded the largest photocurrent. This was expected as it is the highest intensity source in the UV range of the light spectrum. To get a better idea about how the dark current and the photocurrent obtained with the high-power LED compare for each device, their ratios, as calculated by equation 4.5, are plotted in the right column of figure 4.6. Using the aforementioned model, the resistance corresponding to each I-V curve was extracted and the obtained results are given in table 4.6.

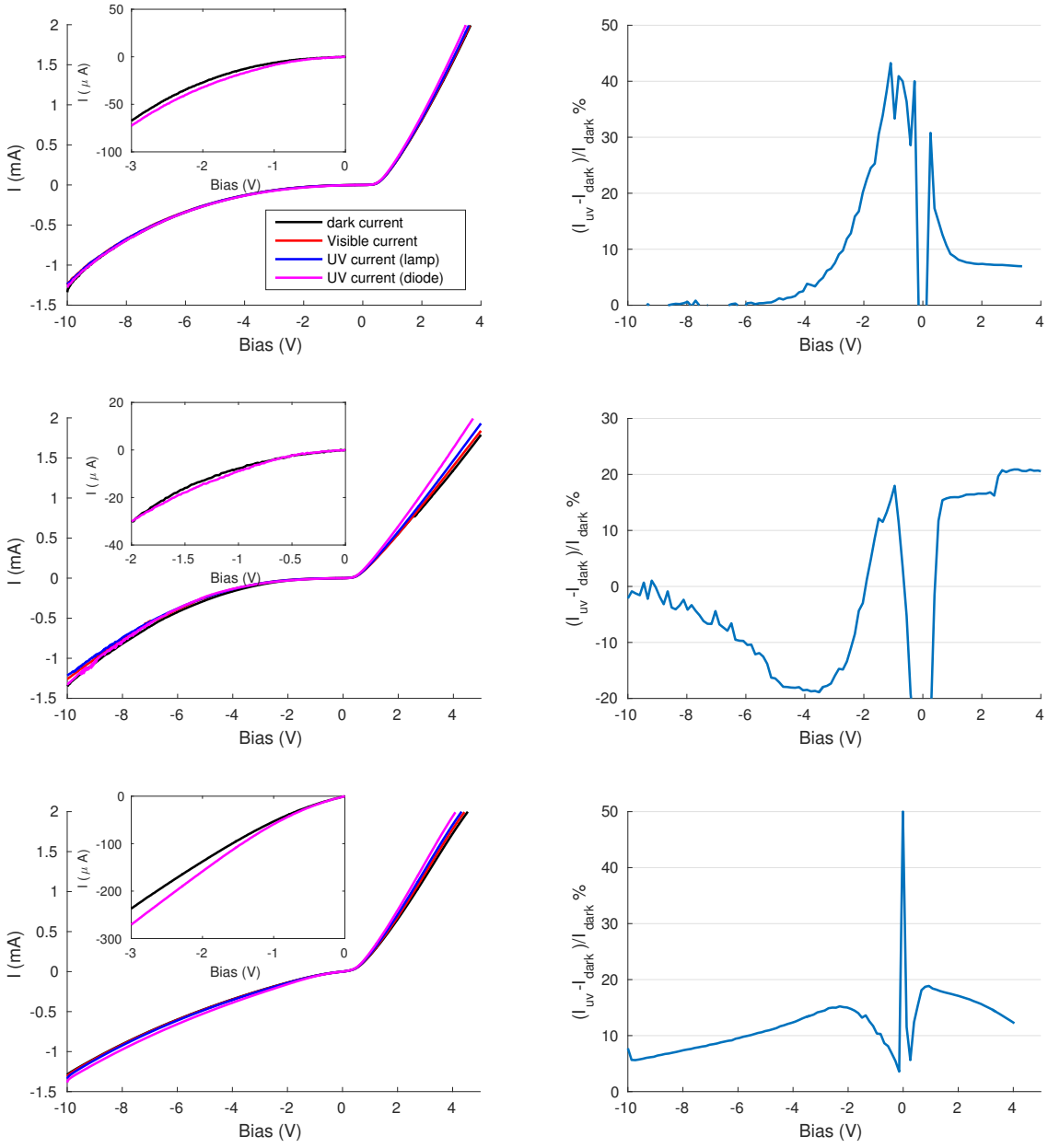

Figure 4.6: IV characteristics for three devices, 210U (top), 216U (middle) and 229U (bottom), under dark (black curve) conditions, when irradiated with visible light (red curve) and when irradiated with two different UV sources, the Deuterium lamp(magenta curve) the high-power and UV led (purple curve) on the left hand side; On the right hand side the respective gain factor between the dark current and the photocurrent obtained with the high power LED is plotted.

$$\Delta_I = \frac{I_{uv} - I_{dark}}{I_{dark}} \ . \tag{4.5}$$

As can be seen from the ratio plots, the gain factor lies in the 5% - 20% range at positive bias. At negative bias, the situation is different. In fact, above -2 volts, the dark current even exceeds the UV current for the 216U device due to instabilities in the current. At higher negative voltages the gain is approximately zero for 210U and 216U. For the 229U device there is some gain, but its magnitude is lower than at positive bias. At lower negative voltages however, peaks in the gain plot are visible. The insets in figure 4.6 show the corresponding I-V characteristics in this range in more detail. Although the difference in current seems negligible, the currents are also relatively low and the ratio reaches values up to 40% in the 210U device, 18% in the 216U device and 15% for the 229U sample. Additionally, we can see that for the 210U and 216U samples the gain factor is approximately constant for positive bias whereas for the 229U sample, after reaching its maximum value at around 1 volt, it decreases in a linear fashion. Regarding the peak at zero bias, it should be ignored as it is a consequence the current having values close to zero.

The fact that our devices present a relatively low gain factor is not surprising since low photocurrent gain for heavily doped GaN nanowires was already observed previously. [15, 89, 90]. A possible explanation for this is that heavy doping limits the depletion width in dark environment to already very small values. Consequently, irradiation with UV light will not drastically improve the electron transport through the wire as it does, for example, in fully depleted wires [15]. The origin of the photocurrent can therefore be attributed mostly to the generation of excess electrons by UV excitation, which only represents a small fraction of the electron concentration in the dark [90]. In fact, if we evaluate the resistance ratio of the microwires, calculated in the same way as the current ratio, between the dark resistance and UV resistance, we obtain ${}^{210U}\Delta_R = 6.1 \pm 0.3$ %, ${}^{216U}\Delta_R = 21.5 \pm 0.9$ % and ${}^{229U}\Delta_R = 10.0 \pm 0.5$ %. The ratios are thus comparable with Δ_I at V $\sim$ 4 V, this is an indication that the variation of the resistance describes the experimental data reasonably well. However, as said before, from this analysis we cannot, with certainty, conclude that the decrease of the microwire resistance dominates with respect to the variation of the other parameters.

Device	R (Ω)			
	Dark	Visible light	UV light (lamp)	UV light (LED)
210U	1261 ± 3	1249 ± 3	1234 ± 3	1189 ± 2
216U	2280 ± 12	2165 ± 4	2064 ± 5	1876 ± 5
229U	1689 ± 6	1639 ± 6	1615 ± 4	1535 ± 4

Table 4.3: The resistance extracted from the I-V curves under different lighting conditions for three devices: 210U, 216U and 229U.

4.2.3 Transient I-V characterization

Transient photoconductivity measurements were performed to analyse the rise and decay time of the devices, as well as the gain factor at a constant bias. Two types of experiments were done, with the high power UV LED as light source. Firstly the light source was turned on and off only once to study the decay time after excitation and secondly, the source was turned on and off several times during one run to analyse the response time. To extract the decay time, the curves were fitted to the following equation [91]

$$I = (I_{uv} - I_{dark}) \exp\left[-\left(\frac{t}{\tau_d}\right)^{\beta}\right] + I_{dark}, \tag{4.6}$$

where the decay time is given by τ_d and β represents the exponential stretching parameter. The rise time can be evaluated by

$$I = (I_{dark} - I_{uv}) \exp\left[-\left(\frac{t}{\tau_r}\right)^{\beta}\right] + I_{uv}. \tag{4.7}$$

Transient characteristics were measured for three different devices and at different bias. In figure 4.7 the data corresponding to the 229U device and respective fits are depicted. In table 4.4 the obtained results for the full set of measurements can be found.

Regarding the results obtained at positive bias, the decay times are of the order of a few seconds whereas the rise time is smaller, typically in the $10^{-3} - 10^{-2}$ seconds range. The exponential stretching parameter yields an average value of 0.19 ± 0.2 for the 210U sample, 0.18 ± 0.2 for the 216U sample and 0.19 ± 0.1 for the 229U sample. The obtained values for the stretching parameter using the equation that corresponds to the rise time yield 0.38 ± 0.4 for device 216U and 0.25 ± 0.3 for device 229U. The ratio between the dark and UV current tends to be larger for low bias, *i.e.*, between 1 and 2 volts, while it shows a small decrease for higher biases, which is consistent with the obtained results from the I-V measurements. The deviations observed in the ratios extracted from the rise time measurements are

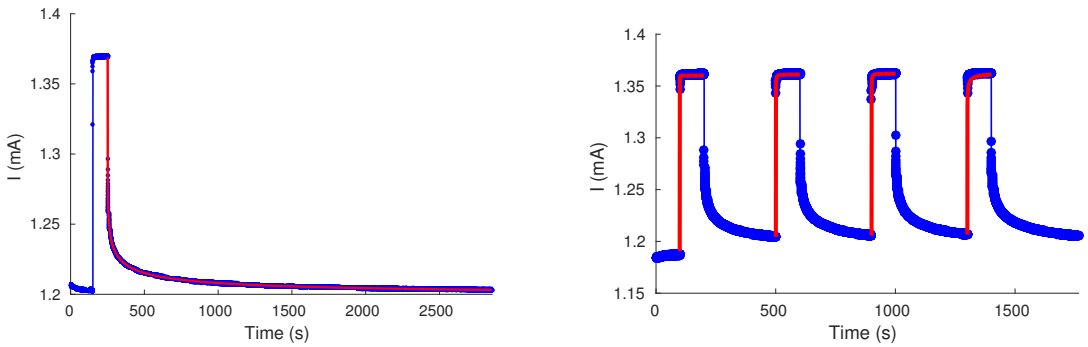

Figure 4.7: Transient IV curves measured with device 229U: the light was turned on and off only once on the left graph to calculate the decay time and turned on and off several times on the right to calculate the rise times. The blue line corresponds to the experimental data and the red line is the fit for the decay time

Decay time						
Device	Voltage	I_{dark} (μA)	I_{uv} (μA)	τ_D (s)	β	Δ_I (%)
210U	1 V	227.213 ± 0.003	245.7 ± 0.1	0.59 ± 0.02	0.222 ± 0.001	7.52 ± 0.04
	2 V	809.86 ± 0.02	872.1 ± 0.1	0.317 ± 0.005	0.1531 ± 0.0004	7.14 ± 0.01
	3 V	1497.23 ± 0.01	1601.8 ± 0.3	0.61 ± 0.01	0.1828 ± 0.0004	6.53 ± 0.02
216U	1 V	161.895 ± 0.007	204.2 ± 0.1	1.61 ± 0.02	0.2338 ± 0.0007	20.72 ± 0.04
	2 V	491.1 ± 0.1	644.7 ± 0.3	2.62 ± 0.04	0.1398 ± 0.0005	23.83 ± 0.04
	3 V	872.6 ± 0.1	1121.1 ± 0.5	0.88 ± 0.01	0.1510 ± 0.0004	22.17 ± 0.04
	4 V	1278.63 ± 0.01	1630.7 ± 0.6	1.047 ± 0.008	0.2113 ± 0.0003	21.59 ± 0.03
229U	1 V	209.57 ± 0.06	241.16 ± 0.07	5.24 ± 0.06	0.1859 ± 0.0005	13.10 ± 0.04
	2 V	665.03 ± 0.05	770.9 ± 0.2	7.38 ± 0.06	0.1689 ± 0.0004	13.73 ± 0.02
	3 V	1199.9 ± 0.1	1368.8 ± 0.2	3.97 ± 0.02	0.2117 ± 0.0002	12.34 ± 0.01
Rise time						
Device	Voltage	I_{dark} (μA)	I_{uv} (μA)	τ_D (s)	β	Δ_I (%)
216U	3 V	895.3 ± 0.4	1121.92 ± 0.02	0.02 ± 0.01	0.49 ± 0.08	20.20 ± 0.04
		895.7 ± 0.4	1121.54 ± 0.02	0.005 ± 0.002	0.35 ± 0.03	20.14 ± 0.04
		896.8 ± 0.3	1121.31 ± 0.02	0.004 ± 0.001	0.33 ± 0.03	20.02 ± 0.03
		896.9 ± 0.4	1121.05 ± 0.02	0.005 ± 0.002	0.35 ± 0.04	25.94 ± 0.03
229U	3 V	1190.0 ± 0.4	1360.02 ± 0.02	0.010 ± 0.001	0.32 ± 0.01	12.50 ± 0.03
		1204.4 ± 0.2	1361.74 ± 0.01	0.0062 ± 0.0002	0.220 ± 0.002	11.55 ± 0.01
		1205.8 ± 0.2	1361.86 ± 0.01	0.0148 ± 0.0004	0.247 ± 0.002	11.46 ± 0.01
		1206.6 ± 0.2	1362.27 ± 0.01	0.0056 ± 0.0002	0.208 ± 0.001	11.43 ± 0.01

Table 4.4: Results of the fit parameters of the decay and rise time

related with the fact that we did not wait long enough for the current to return to its dark value before turning the light source on again. Finally, the dynamic response of the devices is stable and reproducible when running several on/off cycles.

We can thus conclude that the response time of the devices to an excitation source is relatively fast while the decay times are quite large. This observation is not surprising as the effects of PPC have been widely reported in GaN thin film and nanowire devices. The reported results on decay times are however very dispersed. Very fast decay times, below 26 ms, for a-axial nanowires have been reported by Wang *et al.* [19] and Lee *et al.* demonstrated fast recovery time for c-axial nanowires [17]. On the other hand, decay times of ~ 140 [16,92] and even 13000 seconds [21] were obtained for wires with larger diameters. This can be explained by the fact that in GaN nanowires the PPC is strongly dependent on the diameter of the wire. Wires with diameters below a critical diameter, which is given by the following equation [16],

$$d_{crit} = \sqrt{\frac{16\varepsilon_s\varepsilon_0\phi}{eN_d}} \tag{4.8}$$

where ϕ is the surface barrier height, are fully depleted. The subsequent Fermi level pinning is weaker and recombination is faster. However, this is certainly not the case in our wires as their diameter is significantly larger than the critical diameter below which a wire is fully depleted. Especially because it is proportional to $N_d^{-1/2}$. Since N_d is also large in our wires, the critical diameter yields a value of 7 nm if we use $N_d = 10^{20}$ cm^{-3} and the reported value of $\phi = 0.55$ for MBE grown GaN [93]. Theoretically we should therefore expect long decay times. Nevertheless, they are smaller when comparing them to the mentioned values. This possibly suggests that the surface plays a minor role. Therefore, since the scale

of our wires lies in the micrometer range, it also makes sense to compare our results with results based on thin film detectors. Winnerl *et al.* obtained PC decay times of 830 seconds for an MOCVD grown sample with a carrier concentration of 1.4×10^{17} cm^{-3} and of 130 seconds for an MBE grown sample with a carrier concentration of 1.6×10^{19} cm^{-3} [53]. Time constants of the same order were obtained in other studies on GaN photodetectors based on thin films [56, 94, 95, 96]. Comparatively, our devices show thus much faster recombination. This might be due to the superior crystalline quality of microwires when compared to thin films. On the other hand, a relationship between the high doping concentration and faster decay times may exist as we can see when comparing the times obtained for the MOCVD and MBE sample by Winnerl *et al.*. Additionally, Ursaki *et al.* investigated the recovery time for GaN with different parameters and one of the lowest τ_d was obtained for the sample with highest carrier concentration [96] although an opposite results has been obtained by Chen *et al* [97]. Regarding the exponential stretching parameter β, our results are in agreement with some of the previous reported results [94, 96, 98, 99]. On the other hand, other studies have indicated larger values of, between 0.3 and 0.4 for bulk GaN [91] and for nanowires $\beta = 0.46$ and $\beta = 0.79$ [21] have been found corresponding to wires with diameters of 65 and 20 nm, respectively. It is important not to forget however, that although the stretched exponential is a convenient tool for analysis, it is also a very difficult tool to use for the determination of microscopic models as it is general enough to manifest several possible mechanisms. Consequently, the parameters τ and β, in the absence of other supporting evidence, cannot be associated with specific material parameters [99].

Regarding the origin of PPC, it has been extensively studied in III-V compounds and several models have been proposed to explain its existence. However, unfortunately, the nature of several defects and their influence on conductivity are still not well understood. Consequently, there has not been a specific defect associated with the PPC in GaN. In many cases, the PPC is related to the presence of defect states which are bistable between a shallow and a deep energy state [100]. The DX center is an example of such a defect which is originated when shallow donors undergo a lattice relaxation and convert into deep donors [101]. However, radiation with high enough energy can convert the deep donors back into the metastable shallow donor state. The difference in the lattice relaxation between both states creates a potential barrier that slows down the recapture of electrons, giving rise to PPC [102]. Random potential fluctuations due to non stoichiometry [99], defects at heterointerfaces [103] and unintentional incorporation of a cubic crystal phase in hexagonal GaN [104] are also attributed as possible causes.

4.3 Proton-irradiation

The following step in the study of the sensors consists in exposing them to proton irradiation to test their applicability as particle detectors. Therefore, the sensors were placed in the previously described

experimental setup for irradiation and the Agilent analyser was used to perform *in-situ* electrical measurements. After the beam was aligned, the first experiments consisted in measuring the change in current due to the ionizing irradiation. The exposed area and beam current were firstly set to 25×25 μm^2 and 1 nA respectively which corresponds to a total fluence of 1×10^{15} protons/cm^{2}s. The result obtained with device 216U is depicted in figure 4.8. In the I-V curve, sudden current peaks are visible. This is due to the fact that the beam was scanning over the area instead of irradiating everything at the same time. The current peaks appear when the protons go through the wires and disappear when no protons cause excitations. The fact that the current returns to its stable value rather quickly (the sample rate is 5 ms per step) is interesting and possibly indicates different recombination mechanisms than those present after excitation with a UV source. This will be further addressed when performing transient I-V measurements. To obtain a full I-V curve under exposure to protons, the beam area was set to 20×20 μm^2 and the current to 300 pA, which corresponds to a fluence of 5×10^{14} protons/cm^{2}s. The beam, instead of scanning the area, was set to irradiate the full area the entire time. In figure 4.8 the obtained I-V curve is compared with an I-V curve measured under dark conditions immediately before irradiation. The current gain ratio was also calculated and the respective plot can be consulted in figure 4.9. The obtained results are similar to those obtained with UV excitation although an overall larger current increase is visible. The gain plot also resembles the overall behaviour of the one obtained with UV excitation, however due to a higher ΔI, the magnitude of the gain is also higher. At positive bias, ΔI(%) reaches values up to 40% while the gain peak at a low negative bias exceeds 60%, whereas values of approximately 20% were obtained with UV excitation. This can be attributed, on one hand, to the higher excitation density and, on the other hand, to the higher excitation depth. Since the energies involved are much higher, each proton will generate more excess carriers than a photon during UV irradiation. Regarding the depth, as was extracted from the SRIM simulations, the protons cross the entire

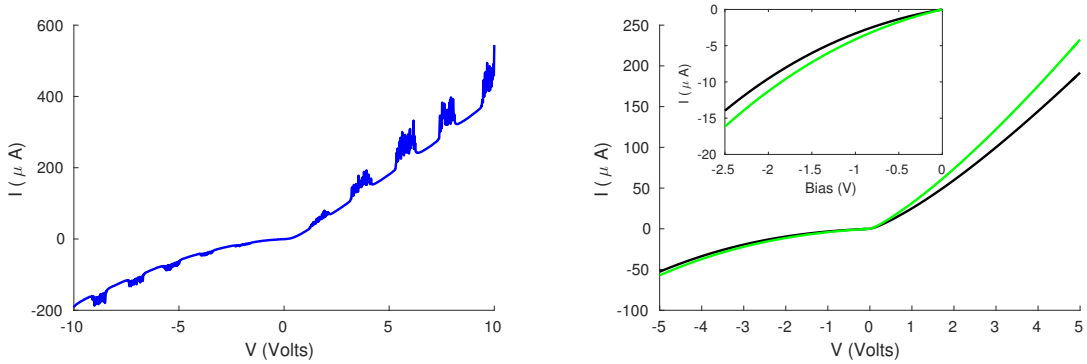

Figure 4.8: The obtained I-V curves when performing electrical measurements during proton irradiation;(left) ionoresponse of the wire when beam sweeps over the device;(right) Comparison of the I-V curve obtained under dark conditions and under continuous proton exposure.

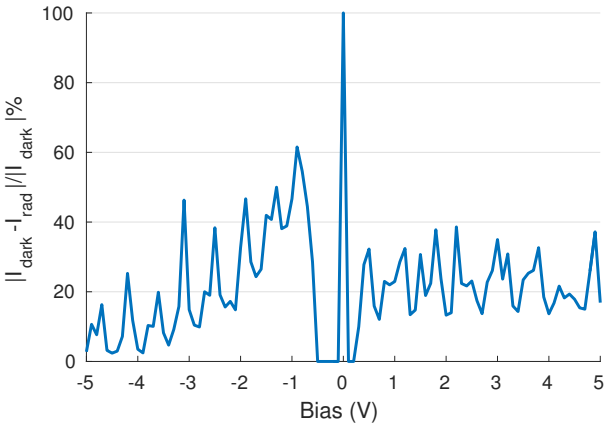

Figure 4.9: Gain ratio between I_{rad} and I_{dark}.

wire and excitation occurs both at the surface and in the bulk region whereas the UV radiation causes mostly excitations at the surface and it is not likely that it penetrates much deeper into the wire.

To verify the effects of the irradiation on the overall performance of the devices, these were continuously exposed to protons for a longer time interval. At the same time, their I-V characteristics were being measured. The experiment was carried on until the devices were disrupted and ceased to conduct. The obtained I-V curves for the 110U device are represented in figure 4.10. As expected, we observed a significant decrease in the conductivity of the devices. To get a better idea of the current evolution during the irradiation, information at constant bias was extracted from the I-V curves and is shown as well. Additionally, the change in resistance during the irradiation of the microwires of the 105U and 1110U device was evaluated for a large set of I-V curves and is represented in figure 4.11. As we can see, a slower increase of R_{mw} is followed by a more accentuated increase when the exposure time becomes longer. We do not see a saturation of the resistance though. This can be attributed to the fact that

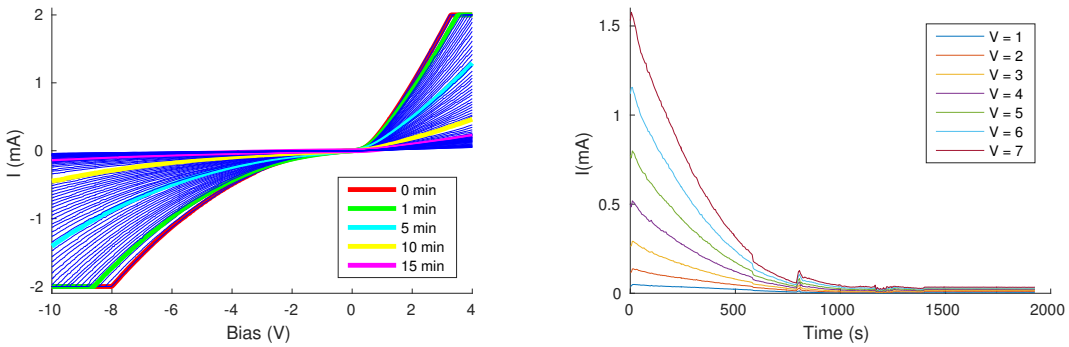

Figure 4.10: The decay conductivity of the 110U device while being exposed to ionizing irradiation; On the left side the I-V curves over the full bias are shown where the legend indicates how long the device is exposed to the irradation; The right graph shows the current decay at fixed bias

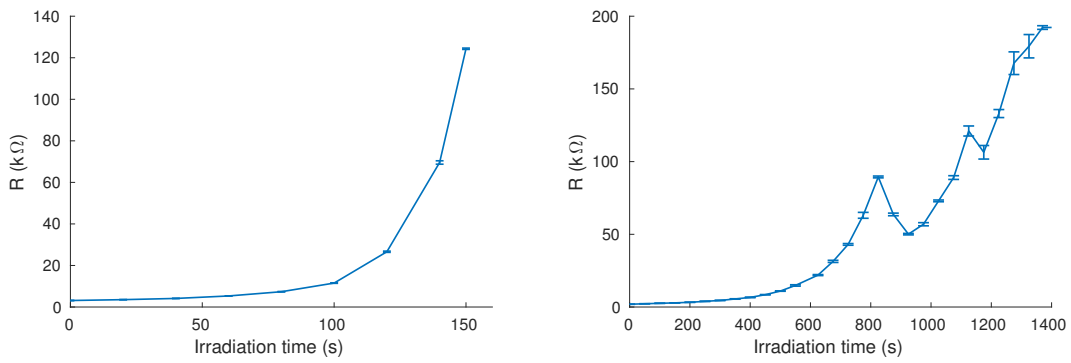

Figure 4.11: The resistance increase as calculated from the I-V curves measured while irradiating the sensors with protons. The graph on the left corresponds to the 105U device and the graph on the right corresponds to the 110U. The irradiation was carried on until the device was disrupted.

the devices are disrupted before this happens. It is also noticeable that the rate of resistance increase occurs in a more drastic fashion for the 105U device than for the 110U device. Consequently, the former is disrupted after approximately 150 seconds, while the latter lasted for over 20 minutes. No specific explanation can be given for this, it is possible that the beam was better aligned for the 105U device, as all other experimental conditions were maintained, or that nonhomogeneous irradiation, suggested by the discontinuities in the curve, led to this result. Finally, to assure that the decrease in conductivity was not related with the applied bias during the irradiation process, the current decay was analysed during the irradiation with a non zero bias and at zero bias. As can be seen in figure 4.12 the results showed no significant difference between both situations.

The decay in conductivity as a consequence of irradiation makes it harder to perform stable transient I-V measurements. However, since the response time of our devices is relatively fast, this could be overcome by only turning the beam on for a single instant, short enough to avoid significant defect cre-

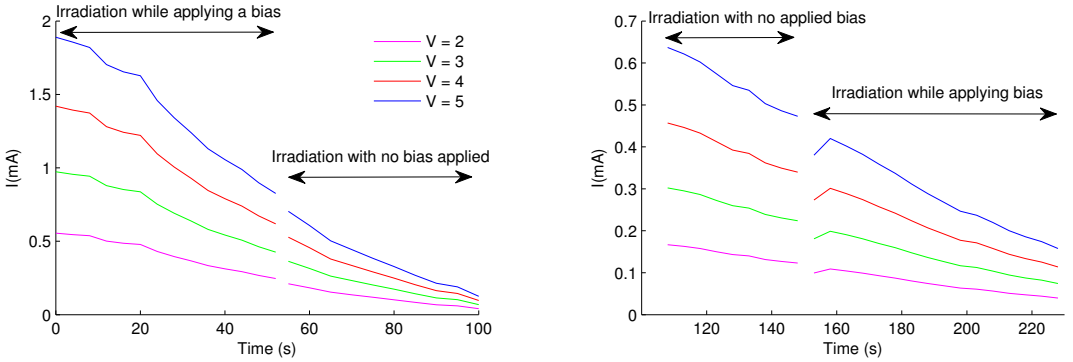

Figure 4.12: Sensor degradation while exposing them to ionizing irradiation with an applied bias and without applying bias

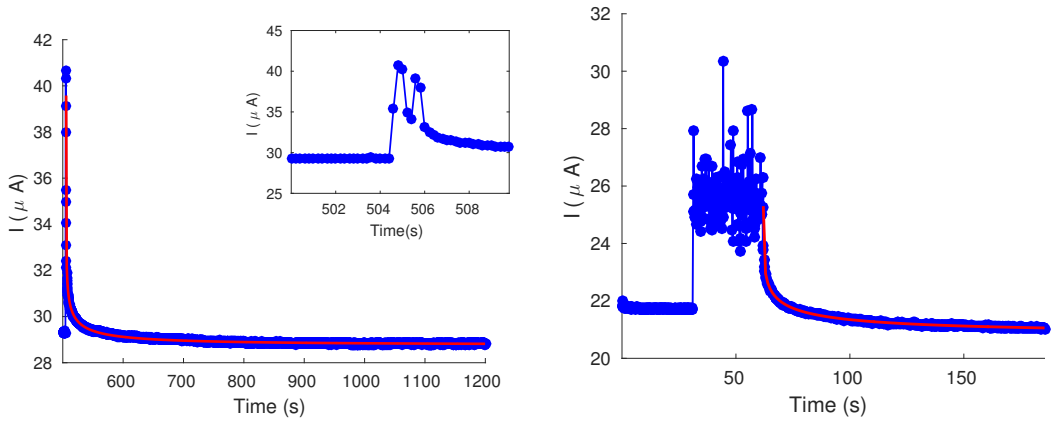

Figure 4.13: Transient I-V measurements relative to the device response to ionizing radiation; On the left side the decay time after a short pulse was measured (the pulse is represented in more detail in the inset) and on the right side the decay time after a pulse of 25 seconds was measured. The blue line corresponds to the experimental data and the red line corresponds to the fit result

ation and long enough to reach the saturation current. Additionally, as can be seen in the graphs of the conductivity decay at constant bias (fig.4.10, the decay rate decreases after some time. Consequently, we were able to perform transient measurements with a longer ON time (∼50 seconds) without a significant decrease in the current due to defect creation by the proton irradiation. The results are depicted in figure 4.13 and the full set of results for several measurements can be found in table 4.5. Note that, to fit the experimental data, the same equations were applied as during the optical characterization.

Regarding the detecting properties of the GaN microwires we already stated that the gain is larger when compared to the gain subsequent of UV irradiation. As explained, this can be related to the higher excitation density and depth. On the other hand, if we compare the decay times from the transient results with those obtained with UV excitation, we can see that they are one order of magnitude smaller when making comparison between equal devices. A larger quantity of data is necessary to confirm if this is a reproducible result and if it is related to the proton irradiation but it could indicate that recombination processes that are subsequent to excitation by protons differ from those subsequent to UV excitation.

Short Pulses				
I_{dark} (μA)	I_{uv} (μA)	τ_D (s)	β	Δ_I (%)
39.76 ± 0.03	30.451 ± 0.002	0.628 ± 0.009	0.2293 ± 0.0008	30.6 ± 0.1
39.58 ± 0.08	28.778 ± 0.003	0.52 ± 0.02	0.238 ± 0.002	37.5 ± 0.3
33.87 ± 0.02	28.075 ± 0.001	0.77 ± 0.01	0.279 ± 0.001	20.64 ± 0.07
27.25 ± 0.04	22.039 ± 0.006	1.45 ± 0.04	0.325 ± 0.004	23.6 ± 0.2
Long Pulse				
I_{dark} (μA)	I_{uv} (μA)	τ_D (s)	β	Δ_I (%)
25.30 ± 0.02	20.869 ± 0.006	2.55 ± 0.04	0.296 ± 0.002	21.2 ± 0.1

Table 4.5: Results of the fit parameters for the decay time after a short pulse with the proton beam and after a longer pulse, $\sim$ 25 sec, on the 229U device.

One possible explanation is that the higher penetration depth of the protons make the recombination less dependent on the surface when compared to UV excitation. The detection potential of GaN microwires or nanowires has not been explored before so we cannot compare our data with reported measurements. Nevertheless, the fact that similar results were obtained as in the case of UV excitation, confirms the potential of GaN microwire-based radiation detectors.

Relative to the study of the irradiation effects, the conventional techniques used in films, such as Hall measurements and deep-level transient spectroscopy, cannot be applied to microwires due to their particular geometry and size. Nonetheless, reports on the irradiation effects on GaN films are abundant and very similar results were obtained while irradiating GaN-based High Electron-Mobility Transistors with 1.8 MeV protons [105, 106]. The primary causes for the degradation of the current are the creation of charged defect centres by displacement of gallium atoms in the crystal lattice due to the proton radiation [107] and defects induced at the metal/semiconductor junction [67]. The former decreases the electron mobility through Coulomb interactions and induces carrier removal while the latter leads to changes in the Schottky barrier height and may cause increases in the contact resistance. Furthermore, Hu *et al.* [105, 106] concluded that significant degradation only starts after exposure to 1.8-MeV fluences of $\sim 10^{14}$ cm^{-2} which is consistent with our findings.

4.3.1 Proton-irradiation effects on photoconductivity

As observed, the ionizing radiation has severe consequences on the overall conductivity of the sensors. It is therefore fundamental to redo the optical measurements in order to see whether the response of the devices is maintained. In a first analysis, it was seen that the devices presented large instabilities during I-V measurements. This is most likely related to the induced damage by the protons. Therefore, a rapid thermal annealing (RTA) process was performed to recover some of the defects. The annealing was done in small steps of temperature and time and the devices started presenting a stable response after a RTA at 600°C for 120 s. Nonetheless, the stable response is only maintained in the range of -5 V to 5 V and annealing at higher temperatures did not increase this range. The effect of the annealing process is shown in figure 4.14. Note that not only the stability but also the conductivity of the devices is improved by the annealing treatment.

After the annealing process, the same experimental procedure performed before the irradiation to optically characterize the devices was followed and the I-V characteristics of the irradiated devices were measured under dark conditions and while being exposed to the UV LED source. The obtained results for the 210U, 216U and 229U devices are depicted in figure 4.15 with the corresponding gain plots. If we compare the responsivity of the devices to the UV light before and after the irradiation, we can immediately see that it has been improved for the latter case. This is most clear for the 216U device. Prior to the irradiation, the gain factor at negative bias was negligible whereas after irradiation the gain

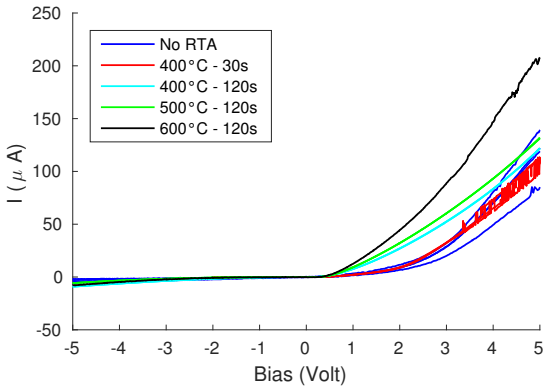

Figure 4.14: The I-V measurements after each annealing step for the 229U device

factor reaches 40% at a bias of -5 volt. For a positive bias, the gain also increased significantly, from around 20% to over 50%. Another interesting fact is that the gain at negative bias is not constant, but rather increases if we apply a larger bias. Although in a lesser extent, the behaviour of the 210U and 229U samples were also improved when comparing the results with those obtained before the irradiation. The 210U device presents a gain factor of 10% at a bias of -5 volt and for $V > 0$, the gain increased approximately by 10%. Relatively to the 229U device, the increase in ΔI(%) for $V > 0$ also increased about 10%. The results at negative bias for the 229U are slightly different however, as one of the contacts became completely rectifying, hence the very small current for $V < 0$. Interesting to see is that the shape of the gain plots is very similar to the ones obtained before irradiation. This is a good indication that the mechanisms behind the photocurrent generation are the same and that only the magnitude of the dark current increased. The comparatively larger increase in the photocurrent gain can be explained following the carrier removal due to the irradiation. As the amount of carriers in the dark case is now smaller, the amount of excess carriers generated when the excitation occurs, represent a bigger fraction, hence the increased gain factor.

Following the steady state I-V measurements, transient measurements were performed as well. While before irradiation, no transient measurements were done for the low conductivity side of the I-V curves, as the increase in current was practically non-existent, now we can perform them due to the improved photocurrent response. The obtained results are represented in figure 4.16 and the corresponding fit parameters are presented in table 4.7. The obtained results for 3 volts are similar to those

Device	R (kΩ)	
	Dark	UV light (LED)
210U	11.91 ± 0.06	10.14 ± 0.05
216U	22.1 ± 0.2	14.6 ± 0.2
229U	16.3 ± 0.4	15.3 ± 0.3

Table 4.6: The resistance extracted from the I-V curves under different lighting conditions for three devices: 210U, 216U and 229U.

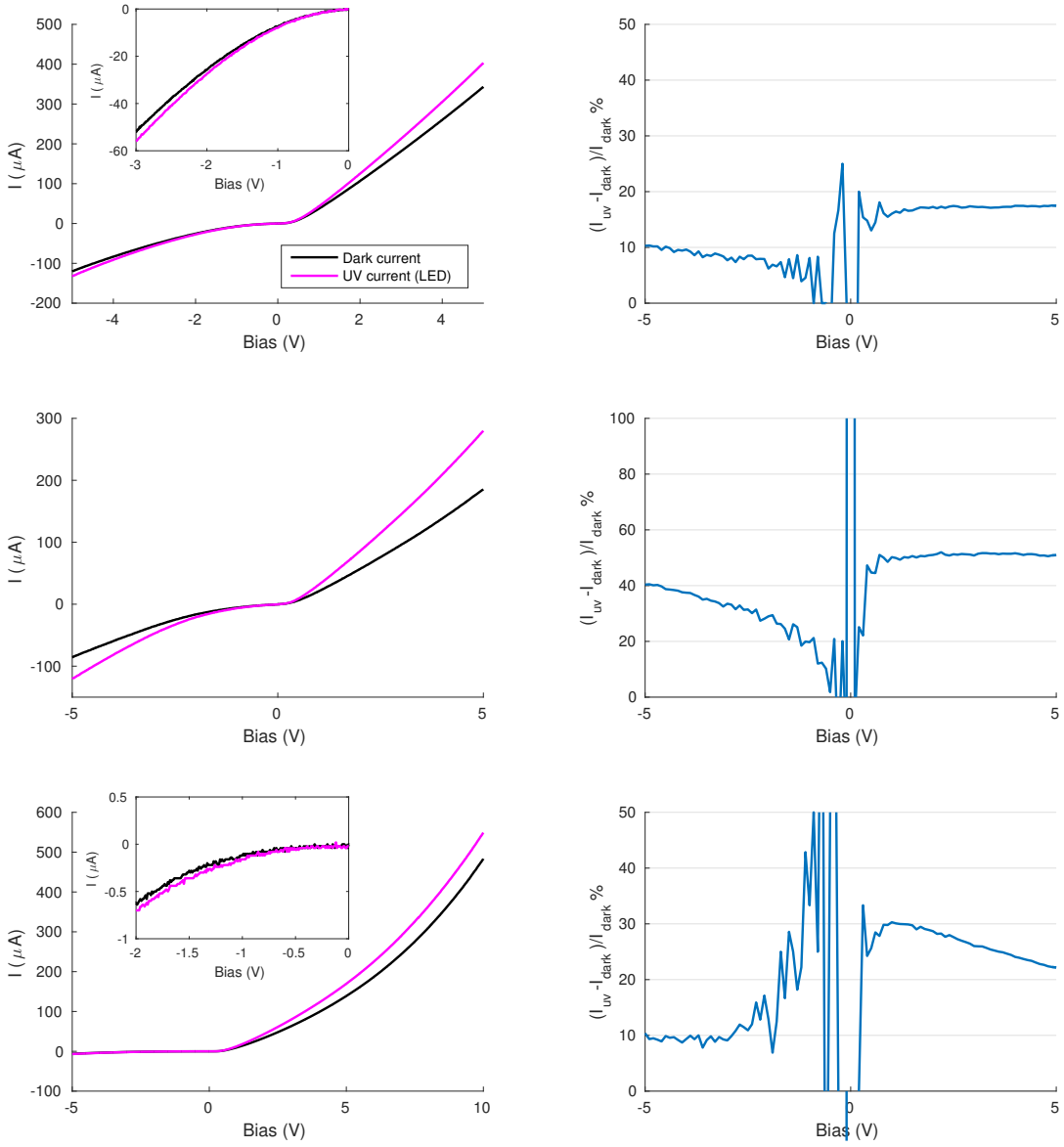

Figure 4.15: I-V characteristics of three devices, 210U (top), 216U (middle) and 229U (bottom), after irradiation dark environment and under exposure of the UV led source. On the left hand side the I-V curves are shown, the black curve corresponds to I_{dark} and the magenta curve to I_{uv}; on the right hand side the gain ratio of the respective curves is plotted

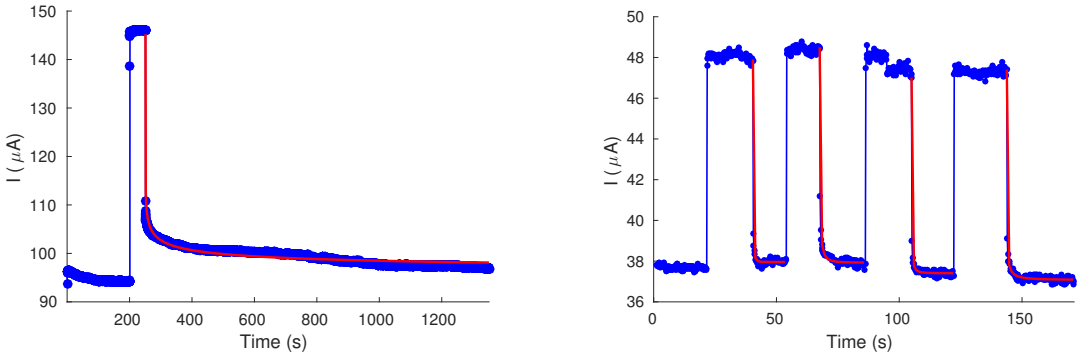

Figure 4.16: Transient IV chracteristics for the 216U device. In the left graph, the bias was fixed at 3 volts and in the right graph at -3 volts. Since the decay time for negative bias is fast, the UV light was turned on and off several times. The blue dots correspond to the experimental data and the red lines to the respective fits.

obtained prior to the irradiation. The 210U sample presents a slightly larger decay time but no conclusion can be made about the origin of this variation or whether it is consistent. Interestingly enough however, the decay time at negative bias is surprisingly fast, one to two orders of magnitude below the decay times at positive bias. As said, unfortunately no measurements at $V < 0$ were possible before the irradiation so we can not directly say that the fast decay times are a consequence of the irradiation. Nonetheless, the enhancement of the decay time after exposure to protons has been observed previously. The partial removal of the deep acceptor states by the proton irradiation was suggested as a possible cause because a quenching of the yellow band, typically associated to transitions between deep acceptor states and the conduction band was observed as well while performing PCS measurements after the irradiation [81]. The results that were obtained in the referred investigations saw the decay time decrease from 65 seconds to 0.5 seconds. This was paired with an increase of the exponential stretching parameter from 0.2 to 1.5. We only observed slightly higher values for β for the measurements with the 216U

Positive bias: 3V					
Device	I_{dark} (μA)	I_{uv} (μA)	τ_D (s)	β	Δ_I (%)
210U	31.59 ± 0.02	24.930 ± 0.002	6.6 ± 0.1	0.1515 ± 0.0004	26.71 ± 0.08
216U	145.23 ± 0.02	96.4 ± 0.3	0.55 ± 0.02	0.1591 ± 0.0009	50.7 ± 0.5
Negative bias: -3V					
Device	I_{dark} (μA)	I_{uv} (μA)	τ_D (s)	β	Δ_I (%)
210U	178.8 ± 0.3	156.87 ± 0.09	0.044 ± 0.008	0.24 ± 0.02	14.0 ± 0.2
	179.0 ± 0.7	156.4 ± 0.3	0.13 ± 0.03	0.25 ± 0.01	14.1 ± 0.5
	179.9 ± 0.2	154.9 ± 0.1	0.52 ± 0.04	0.211 ± 0.003	16.1 ± 0.1
216U	47.9 ± 0.1	37.96 ± 0.02	0.05 ± 0.01	0.46 ± 0.05	26.2 ± 0.3
	48.5 ± 0.1	37.93 ± 0.02	0.10 ± 0.01	0.40 ± 0.02	27.9 ± 0.3
	47.0 ± 0.1	37.41 ± 0.01	0.033 ± 0.007	0.35 ± 0.03	25.6 ± 0.3
	47.4 ± 0.1	37.08 ± 0.02	0.030 ± 0.007	0.28 ± 0.02	27.8 ± 0.3

Table 4.7: Results of the fit parameters for the decay time at a positive bias of 3 Volts and a negative bias of -3 volts, regarding two devices, 210U and 216U, after they were exposed to ionizing radiation.

device. Additionally, the reason why the decay times only improved for negative bias, is unclear. PCS measurements might shed a light on this matter, but unfortunately, it was not possible to perform these measurements since the responsivity of the wires to the Hamamatsu lamp was not significant enough to distinguish any transitions in the spectra.

5

Conclusion

The goal of this work was to develop radiation sensors based on GaN microwires, with special interest towards their capability to detect protons. The followed strategy consisted in isolating single wires, grown by MOCVD, on a substrate and deposit metal contacts on their extremities, in order to obtain rectifying Schottky contacts. Afterwards, several opto-electrical measurement techniques were used to characterize the intrinsic properties of the microwires and the mechanisms that contributed to their photoconductivity. The spearhead of this work consisted, however, in studying the potential of the GaN microwires regarding the detection of high energy particles, in this case 2 MeV protons.

The process of the contact deposition was successful in the sense that conducting devices were obtained. However, the rectifying nature was only partially achieved due to, on one hand, the high concentration of Si donors incorporated into the microwires during the growth process and, on the other hand, difficulties in controlling the surface processes during the deposition of the metals. In particular the presence of an insulating silicon nitride layer at the microwire surface can influence the contacts and in future work, an extra etching step should be introduced in the fabrication process before the contact deposition to avoid it.

The performed opto-electrical characterization measurements revealed that the bandgap of the GaN was well defined and no significant absorption in the visible spectrum was observed. The photocurrent gain of the fabricated photodectectors is however still to low to be interesting for application in actual devices. The main cause for this occurrence is again the high doping concentration, as this leads to a very large dark current, despite the presence of Schottky barrier at the metal-semiconductor interface. Despite the low gain factors we obtained, transient measurements revealed faster decay times in comparison to most reports on GaN nanowire or thin film based photodetectors. A possible cause for this observation is a compromise between the surface mechanism, that affect microwires in a lesser extent when compared to nanowires due to the smaller surface-to-volume ratio, and the higher crystalline quality of the microwires when compared to thin films.

Our findings based on the proton-irradiation studies with the detectors revealed promising results. Current gain factors of up to 40% between the radiation and dark case were obtained. After excitation, the time it took the devices to return to the stable dark current was comparable to those obtained after UV excitation. Thus, similar results were obtained for both UV and proton excitation, which indicates that GaN microwires have the potential to be applied in radiation detectors in the same way as they are already applied in UV photodetectors. In this work, the biggest setback was the fast degradation of the devices when exposed to the protons. However, a relatively high flux of $\sim 10^{15}$ protons/cm^{2}s was used and considering other works in the existent literature, the electrical performance of GaN starts to worsen at fluences of $\sim 10^{14}$ protons/cm^2 [105]. Therefore, by optimizing the experimental conditions this issue might be overcome. Finally, the irradiated devices were tested again regarding their UV detection potential. The results indicated overall improved responses and the photocurrent gain increased to

approximately twice the values obtained prior to the irradiation. The main factor here was the decrease of the dark current due to carrier loss after irradiation, which makes the relative increase of the current more significant. Promising results regarding faster decay times were also obtained, however, more investigation needs to be performed to reach solid conclusions on this matter.

One of the main conclusions of this investigation is however, that there exists a great potential to continue to develop this concept and a large amount of future work can be done. First of all, the fabrication process should be optimized in order to obtain a better quality and reproducibility concerning the contacts. Furthermore, in order to better understand the generation and recombination processes additional characterization should be performed. PCS after irradiation to different proton fluences may give information on deep levels formed during the proton bombardment. Temperature dependent measurements would furthermore allow to assess activation energies for certain processes. Four point measurements of the I-V characteristics could help to distinguish the role of the contacts from that of the microwire.

Finally, perhaps the largest setback in this work were the effects of the high doping concentration associated with the GaN microwires which leads to high dark currents and compromises the formation of good Schottky contacts. Consequently, in future work the use of these specific wires should be reviewed. Based on MOCVD wires it would be possible to grow a p-n junction which should serve as active zone of the device. Maintaining the simple MSM structure, a molecular beam epitaxy growth process would allow the growth of wires with much lower doping levels. However, the dimensions of MBE grown wires are typically much smaller than the present wires making their integration in the device a more difficult task. Finally, after these optimisation steps it would be interesting to test the devices for other kinds of radiation for example X-rays.

Bibliography

[1] C. M. Lieber and Z. L. Wang, "Functional nanowires," *MRS Bulletin*, vol. 32, no. 2, p. 99–108, 2007. [Online]. Available: http://dx.doi.org/10.1557/mrs2007.41

[2] I. Akasaki, "Fascinating journeys into blue light (nobel lecture)," *Annalen der Physik*, vol. 527, no. 5-6, pp. 311–326, 2015. [Online]. Available: http://dx.doi.org/10.1002/andp.201500803

[3] L. Rigutti and M. Tchernycheva, *GaN Nanowire-based Ultraviolet Photodetectors*. John Wiley & Sons, 2014, pp. 179–202.

[4] S. J. Pearton, F. Ren, E. Patrick, M. E. Law, and A. Y. Polyakov, "Review—ionizing radiation damage effects on GaN devices," *ECS Journal of Solid State Science and Technology*, vol. 5, no. 2, pp. Q35–Q60, 2016. [Online]. Available: https://doi.org/10.1149/2.0251602jss

[5] E. Schlenker, A. Bakin, T. Weimann, P. Hinze, D. H. Weber, A. Gölzhäuser, H.-H. Wehmann, and A. Waag, "On the difficulties in characterizing ZnO nanowires," *Nanotechnology*, vol. 19, no. 36, p. 365707, 2008. [Online]. Available: https://doi.org/10.1088/0957-4484/19/36/365707

[6] H. Amano, N. Sawaki, I. Akasaki, and Y. Toyoda, "Metalorganic vapor phase epitaxial growth of a high quality GaN film using an AlN buffer layer," *Applied Physics Letters*, vol. 48, no. 5, pp. 353–355, 1986. [Online]. Available: http://dx.doi.org/10.1063/1.96549

[7] M. A. Khan, J. N. Kuznia, D. T. Olson, J. M. V. Hove, M. Blasingame, and L. F. Reitz, "High-responsivity photoconductive ultraviolet sensors based on insulating single-crystal GaN epilayers," *Applied Physics Letters*, vol. 60, no. 23, pp. 2917–2919, 1992. [Online]. Available: http://dx.doi.org/10.1063/1.106819

[8] Q. Chen, J. W. Yang, A. Osinsky, S. Gangopadhyay, B. Lim, M. Z. Anwar, M. A. Khan, D. Kuksenkov, and H. Temkin, "Schottky barrier detectors on GaN for visible–blind ultraviolet detection," *Applied Physics Letters*, vol. 70, no. 17, pp. 2277–2279, 1997. [Online]. Available: http://dx.doi.org/10.1063/1.118837

[9] E. Monroy, E. Muñoz, F. J. Sánchez, F. Calle, E. Calleja, B. Beaumont, P. Gibart, J. A. Muñoz, and F. Cussó, "High-performance GaN p-n junction photodetectors for solar ultraviolet applications," *Semiconductor Science and Technology*, vol. 13, no. 9, p. 1042, 1998. [Online]. Available: https://doi.org/10.1088/0268-1242/13/9/013

[10] G. Parish, S. Keller, P. Kozodoy, J. P. Ibbetson, H. Marchand, P. T. Fini, S. B. Fleischer, S. P. DenBaars, U. K. Mishra, and E. J. Tarsa, "High-performance (Al,Ga)N-based solar-blind ultraviolet p–i–n detectors on laterally epitaxially overgrown GaN," *Applied Physics Letters*, vol. 75, no. 2, pp. 247–249, 1999. [Online]. Available: http://dx.doi.org/10.1063/1.124337

[11] A. Osinsky, S. Gangopadhyay, R. Gaska, B. Williams, M. A. Khan, D. Kuksenkov, and H. Temkin, "Low noise p-π-n GaN ultraviolet photodetectors," *Applied Physics Letters*, vol. 71, no. 16, pp. 2334–2336, 1997. [Online]. Available: http://dx.doi.org/10.1063/1.120023

[12] C. Vieu, F. Carcenac, A. Pépin, Y. Chen, M. Mejias, A. Lebib, L. Manin-Ferlazzo, L. Couraud, and H. Launois, "Electron beam lithography: resolution limits and applications," *Applied Surface Science*, vol. 164, no. 1, pp. 111 – 117, 2000. [Online]. Available: http://www.sciencedirect.com/science/article/pii/S0169433200003524

[13] S. Raychaudhuri, S. A. Dayeh, D. Wang, and E. T. Yu, "Precise semiconductor nanowire placement through dielectrophoresis," *Nano Letters*, vol. 9, no. 6, pp. 2260–2266, 2009, pMID: 19419157. [Online]. Available: http://dx.doi.org/10.1021/nl900423g

[14] C. Thelander, P. Agarwal, S. Brongersma, J. Eymery, L. Feiner, A. Forchel, M. Scheffler, W. Riess, B. Ohlsson, U. Gösele, and L. Samuelson, "Nanowire-based one-dimensional electronics," *Materials Today*, vol. 9, no. 10, pp. 28 – 35, 2006. [Online]. Available: http://dx.doi.org/10.1016/S1369-7021(06)71651-0

[15] F. González-Posada, R. Songmuang, M. Den Hertog, and E. Monroy, "Room-temperature photodetection dynamics of single GaN nanowires," *Nano Letters*, vol. 12, no. 1, pp. 172–176, 2012, pMID: 22142411. [Online]. Available: http://dx.doi.org/10.1021/nl2032684

[16] R. Calarco, M. Marso, T. Richter, A. I. Aykanat, R. Meijers, A. v.d. Hart, T. Stoica, and H. Lüth, "Size-dependent photoconductivity in MBE-grown GaN−nanowires," *Nano Letters*, vol. 5, no. 5, pp. 981–984, 2005, pMID: 15884906. [Online]. Available: http://dx.doi.org/10.1021/nl0500306

[17] J.-W. Lee, K.-J. Moon, M.-H. Ham, and J.-M. Myoung, "Dielectrophoretic assembly of GaN nanowires for UV sensor applications," *Solid State Communications*, vol. 148, no. 5, pp. 194 – 198, 2008. [Online]. Available: http://dx.doi.org/10.1016/j.ssc.2008.08.022

[18] E. Stern, G. Cheng, E. Cimpoiasu, R. Klie, S. Guthrie, J. Klemic, I. Kretzschmar, E. Steinlauf, D. Turner-Evans, E. Broomfield, J. Hyland, R. Koudelka, T. Boone, M. Young, A. Sanders, R. Munden, T. Lee, D. Routenberg, and M. A. Reed, "Electrical characterization of single GaN nanowires," *Nanotechnology*, vol. 16, no. 12, p. 2941, 2005. [Online]. Available: http://dx.doi.org/10.1088/0957-4484/16/12/037

[19] X. Wang, Y. Zhang, X. Chen, M. He, C. Liu, Y. Yin, X. Zou, and S. Li, "Ultrafast, superhigh gain visible-blind UV detector and optical logic gates based on nonpolar a-axial GaN nanowire," *Nanoscale*, vol. 6, pp. 12 009–12 017, 2014. [Online]. Available: http://dx.doi.org/10.1039/c4nr03581j

[20] R.-S. Chen, H.-Y. Chen, C.-Y. Lu, K.-H. Chen, C.-P. Chen, L.-C. Chen, and Y.-J. Yang, "Ultrahigh photocurrent gain in m-axial GaN nanowires," *Applied Physics Letters*, vol. 91, no. 22, p. 223106, 2007. [Online]. Available: http://dx.doi.org/10.1063/1.2817595

[21] H.-Y. Chen, R.-S. Chen, N. K. Rajan, F.-C. Chang, L.-C. Chen, K.-H. Chen, Y.-J. Yang, and M. A. Reed, "Size-dependent persistent photocurrent and surface band bending in m-axial GaN nanowires," *Phys. Rev. B*, vol. 84, p. 205443, Nov 2011. [Online]. Available: http://dx.doi.org/10.1103/PhysRevB.84.205443

[22] V. Ayres, B. Jacobs, M. Englund, E. Carey, M. Crimp, R. Ronningen, A. Zeller, J. Halpern, M.-Q. He, G. Harris, D. Liu, H. Shaw, and M. Petkov, "Investigations of heavy ion irradiation of gallium nitride nanowires and nanocircuits," *Diamond and Related Materials*, vol. 15, no. 4, pp. 1117 – 1121, 2006, diamond 2005. [Online]. Available: http://dx.doi.org/10.1016/j.diamond.2005.11.055

[23] J. Vaitkus, W. Cunningham, E. Gaubas, M. Rahman, S. Sakai, K. Smith, and T. Wang, "Semi-insulating GaN and its evaluation for α particle detection," *Nuclear Instruments and Methods in Physics Research Section A: Accelerators, Spectrometers, Detectors and Associated Equipment*, vol. 509, no. 1, pp. 60 – 64, 2003, proceedings of the 4th Internatonal Workshop on Radiation Imaging Detectors. [Online]. Available: http://dx.doi.org/10.1016/S0168-9002(03)01550-X

[24] A. Y. Polyakov, N. B. Smirnov, A. V. Govorkov, A. V. Markov, E. A. Kozhukhova, I. M. Gazizov, N. G. Kolin, D. I. Merkurisov, V. M. Boiko, A. V. Korulin, V. M. Zalyetin, S. J. Pearton, I.-H. Lee, A. M. Dabiran, and P. P. Chow, "Alpha particle detection with GaN schottky diodes," *Journal of Applied Physics*, vol. 106, no. 10, p. 103708, 2009. [Online]. Available: http://dx.doi.org/10.1063/1.3261806

[25] I.-H. Lee, A. Y. Polyakov, N. B. Smirnov, A. V. Govorkov, E. A. Kozhukhova, V. M. Zaletin, I. M. Gazizov, N. G. Kolin, and S. J. Pearton, "Electrical properties and radiation detector performance of free-standing bulk n-GaN," *Journal of Vacuum Science & Technology B, Nanotechnology*

and Microelectronics: Materials, Processing, Measurement, and Phenomena, vol. 30, no. 2, p. 021205, 2012. [Online]. Available: http://dx.doi.org/10.1116/1.3690644

[26] A. Johannes, R. Niepelt, M. Gnauck, and C. Ronning, "Persistent ion beam induced conductivity in zinc oxide nanowires," *Applied Physics Letters*, vol. 99, no. 25, p. 252105, 2011. [Online]. Available: http://dx.doi.org/10.1063/1.3671164

[27] M. Choe, W.-K. Hong, W. Park, J. Yoon, G. Jo, T. Kwon, M. E. Welland, and T. Lee, "UV photoconductivity characteristics of ZnO nanowire field effect transistor treated by proton irradiation," *Thin Solid Films*, vol. 520, no. 9, pp. 3624 – 3628, 2012. [Online]. Available: http://dx.doi.org/10.1016/j.tsf.2012.01.015

[28] H. Schulz and K. Thiemann, "Crystal structure refinement of AlN and GaN," *Solid State Communications*, vol. 23, no. 11, pp. 815 – 819, 1977. [Online]. Available: http://dx.doi.org/10.1016/0038-1098(77)90959-0

[29] M. Leszczynski, H. Teisseyre, T. Suski, I. Grzegory, M. Bockowski, J. Jun, S. Porowski, K. Pakula, J. M. Baranowski, C. T. Foxon, and T. S. Cheng, "Lattice parameters of gallium nitride," *Applied Physics Letters*, vol. 69, no. 1, pp. 73–75, 1996. [Online]. Available: http://dx.doi.org/10.1063/1.118123

[30] H. P. Maruska and J. J. Tietjen, "The preparation and properties of vapor deposited single crystalline GaN," *Applied Physics Letters*, vol. 15, no. 10, pp. 327–329, 1969. [Online]. Available: http://dx.doi.org/10.1063/1.1652845

[31] S. H. Simon, Ed., *The Oxford Solid State Basics*. Oxford: Oxford University Press, 2013.

[32] M. E. Levinshtein, S. L. Rumyantsev, and M. S. Shur, Eds., *Properties of Advanced Semiconductor Materials: GaN, AlN, InN, BN, SiC, SiGe*. United Kingdom: Wiley, 2001.

[33] M. Suzuki, T. Uenoyama, and A. Yanase, "First-principles calculations of effective-mass parameters of AlN and GaN," *Phys. Rev. B*, vol. 52, pp. 8132–8139, Sep 1995. [Online]. Available: https://doi.org/10.1103/PhysRevB.52.8132

[34] D. Kotchetkov, J. Zou, A. A. Balandin, D. I. Florescu, and F. H. Pollak, "Effect of dislocations on thermal conductivity of GaN layers," *Applied Physics Letters*, vol. 79, no. 26, pp. 4316–4318, 2001. [Online]. Available: http://dx.doi.org/10.1063/1.1427153

[35] J. Zou, D. Kotchetkov, A. A. Balandin, D. I. Florescu, and F. H. Pollak, "Thermal conductivity of GaN films: Effects of impurities and dislocations," *Journal of Applied Physics*, vol. 92, no. 5, pp. 2534–2539, 2002. [Online]. Available: http://dx.doi.org/10.1063/1.1497704

[36] K. O'Donnell and V. Dierolf, *Rare Earth Doped III-Nitrides for Optoelectronic and Spintronic Applications*. Springer, 2010.

[37] S. Nakamura, T. Mukai, and M. Senoh, "Si- and Ge-doped GaN films grown with GaN buffer layers," *Japanese Journal of Applied Physics*, vol. 31, no. 9R, p. 2883, 1992. [Online]. Available: http://dx.doi.org/10.1143/JJAP.31.2883

[38] G. Koblmüller, F. Wu, T. Mates, J. S. Speck, S. Fernández-Garrido, and E. Calleja, "High electron mobility GaN grown under N-rich conditions by plasma-assisted molecular beam epitaxy," *Applied Physics Letters*, vol. 91, no. 22, p. 221905, 2007. [Online]. Available: http://dx.doi.org/10.1063/1.2817597

[39] D. A. Neaman, Ed., *Semiconductor Physics and Devices*, 3rd ed. New York: McGraw-Hill, 2003.

[40] A. M. Cowley and S. M. Sze, "Surface states and barrier height of metal-semiconductor systems," *Journal of Applied Physics*, vol. 36, no. 10, pp. 3212–3220, 1965. [Online]. Available: http://dx.doi.org/10.1063/1.1702952

[41] W. E. Spicer, I. Lindau, J. N. Miller, D. T. Ling, P. Pianetta, P. W. Chye, and C. M. Garner, "Studies of surface electronic structure and surface chemistry using synchrotron radiation," *Physica Scripta*, vol. 16, no. 5-6, p. 388, 1977. [Online]. Available: http://dx.doi.org/10.1088/0031-8949/16/5-6/037

[42] W. E. Spicer, P. W. Chye, P. R. Skeath, C. Y. Su, and I. Lindau, *New and unified model for Schottky barrier and III-V insulator interface states formation*. Dordrecht: Springer Netherlands, 1990, pp. 142–152. [Online]. Available: https://doi.org/10.1007/978-94-009-0657-0_17

[43] E. H. Rhoderick and R. H. Williams, Eds., *Metal-semiconductor contacts*. Michigan: Clarendon Press, 1988.

[44] E. L. Murphy and R. H. Good, "Thermionic emission, field emission, and the transition region," *Phys. Rev.*, vol. 102, pp. 1464–1473, Jun 1956. [Online]. Available: https://dx.doi.org/10.1103/PhysRev.102.1464

[45] B. L. Sharma, Ed., *Metal-Semiconductor Schottky Barrier Junctions and Their Applications*. United States: Springer US, 1984.

[46] J.-R. Kim, H. M. So, J. W. Park, J.-J. Kim, J. Kim, C. J. Lee, and S. C. Lyu, "Electrical transport properties of individual gallium nitride nanowires synthesized by chemical-vapor-deposition," *Applied Physics Letters*, vol. 80, no. 19, pp. 3548–3550, 2002. [Online]. Available: http://dx.doi.org/10.1063/1.1478158

[47] J. Appenzeller, M. Radosavljević, J. Knoch, and P. Avouris, “Tunneling versus thermionic emission in one-dimensional semiconductors,” *Phys. Rev. Lett.*, vol. 92, p. 048301, Jan 2004. [Online]. Available: https://dx.doi.org/10.1103/PhysRevLett.92.048301

[48] F. Padovani and R. Stratton, “Field and thermionic-field emission in Schottky barriers,” *Solid-State Electronics*, vol. 9, no. 7, pp. 695 – 707, 1966. [Online]. Available: http://dx.doi.org/10.1016/0038-1101(66)90097-9

[49] S. M. Sze and K. N. Kwok, Eds., *Physics of Semiconductor Devices*, 3rd ed. New Jersey: John Whiley & Sons, 2007.

[50] C. Crowell and V. Rideout, “Normalized thermionic-field (T-F) emission in metal-semiconductor (Schottky) barriers,” *Solid-State Electronics*, vol. 12, no. 2, pp. 89 – 105, 1969. [Online]. Available: http://dx.doi.org/10.1016/0038-1101(69)90117-8

[51] L. Cao, J.-S. Park, P. Fan, B. Clemens, and M. L. Brongersma, “Resonant germanium nanoantenna photodetectors,” *Nano Letters*, vol. 10, no. 4, pp. 1229–1233, 2010, pMID: 20230043. [Online]. Available: http://dx.doi.org/10.1021/nl9037278

[52] E. Muñoz, E. Monroy, J. A. Garrido, I. Izpura, F. J. Sánchez, M. A. Sánchez-García, E. Calleja, B. Beaumont, and P. Gibart, “Photoconductor gain mechanisms in GaN ultraviolet detectors,” *Applied Physics Letters*, vol. 71, no. 7, pp. 870–872, 1997. [Online]. Available: http://dx.doi.org/10.1063/1.119673

[53] A. Winnerl, R. N. Pereira, and M. Stutzmann, “Kinetics of optically excited charge carriers at the GaN surface,” *Phys. Rev. B*, vol. 91, p. 075316, Feb 2015. [Online]. Available: https://doi.org/10.1103/PhysRevB.91.075316

[54] M. Salis, A. Anedda, F. Quarati, A. J. Blue, and W. Cunningham, “Photocurrent in epitaxial GaN,” *Journal of Applied Physics*, vol. 97, no. 3, p. 033709, 2005. [Online]. Available: http://dx.doi.org/10.1063/1.1848191

[55] B. Potì, A. Passaseo, M. Lomascolo, R. Cingolani, and M. D. Vittorio, “Persistent photocurrent spectroscopy of GaN metal–semiconductor–metal photodetectors on long time scale,” *Applied Physics Letters*, vol. 85, no. 25, pp. 6083–6085, 2004. [Online]. Available: http://dx.doi.org/10.1063/1.1840122

[56] M. T. Hirsch, J. A. Wolk, W. Walukiewicz, and E. E. Haller, “Persistent photoconductivity in n-type GaN,” *Applied Physics Letters*, vol. 71, no. 8, pp. 1098–1100, 1997. [Online]. Available: http://dx.doi.org/10.1063/1.119738

[57] I. Shalish, L. Kronik, G. Segal, Y. Shapira, S. Zamir, B. Meyler, and J. Salzman, "Grain-boundary-controlled transport in GaN layers," *Phys. Rev. B*, vol. 61, pp. 15 573–15 576, Jun 2000. [Online]. Available: https:doi.org/10.1103/PhysRevB.61.15573

[58] O. Katz, V. Garber, B. Meyler, G. Bahir, and J. Salzman, "Gain mechanism in GaN Schottky ultraviolet detectors," *Applied Physics Letters*, vol. 79, no. 10, pp. 1417–1419, 2001. [Online]. Available: http://dx.doi.org/10.1063/1.1394717

[59] A. Y. Polyakov, *Radiation Effects in GaN*. Heidelberg: Springer Heidelberg, 2012, pp. 251–294. [Online]. Available: https://doi.org/10.1007/978-3-642-23521-4_9

[60] D. C. Look, D. C. Reynolds, J. W. Hemsky, J. R. Sizelove, R. L. Jones, and R. J. Molnar, "Defect donor and acceptor in GaN," *Phys. Rev. Lett.*, vol. 79, pp. 2273–2276, Sep 1997. [Online]. Available: https://dx.doi.org/10.1103/PhysRevLett.79.2273

[61] J. Neugebauer and C. G. Van de Walle, "Atomic geometry and electronic structure of native defects in GaN," *Phys. Rev. B*, vol. 50, pp. 8067–8070, Sep 1994. [Online]. Available: https://dx.doi.org/10.1103/PhysRevB.50.8067

[62] P. Bogusl/awski, E. L. Briggs, and J. Bernholc, "Native defects in gallium nitride," *Phys. Rev. B*, vol. 51, pp. 17 255–17 258, Jun 1995. [Online]. Available: https://dx.doi.org/10.1103/PhysRevB.51.17255

[63] G. A. Umana-Membreno, J. M. Dell, G. Parish, B. D. Nener, L. Faraone, and U. K. Mishra, "^{60}Co gamma irradiation effects on n-GaN Schottky diodes," *IEEE Transactions on Electron Devices*, vol. 50, no. 12, pp. 2326–2334, 2003. [Online]. Available: https://dx.doi.org/10.1109/TED.2003.820122

[64] L. Polenta, Z.-Q. Fang, and D. C. Look, "On the main irradiation-induced defect in GaN," *Applied Physics Letters*, vol. 76, no. 15, pp. 2086–2088, 2000. [Online]. Available: http://dx.doi.org/10.1063/1.126263

[65] A. Polyakov, A. Usikov, B. Theys, N. Smirnov, A. Govorkov, F. Jomard, N. Shmidt, and W. Lundin, "Effects of proton implantation on electrical and recombination properties of n-GaN," *Solid-State Electronics*, vol. 44, no. 11, pp. 1971 – 1983, 2000. [Online]. Available: http://dx.doi.org/10.1016/S0038-1101(00)00159-3

[66] S. Goodman, F. Auret, F. Koschnick, J.-M. Spaeth, B. Beaumont, and P. Gibart, "Radiation induced defects in MOVPE grown n-GaN," *Materials Science and Engineering: B*, vol. 71, no. 1, pp. 100 – 103, 2000. [Online]. Available: http://dx.doi.org/10.1016/S0921-5107(99)00357-8

[67] B. D. White, M. Bataiev, S. H. Goss, X. Hu, A. Karmarkar, D. M. Fleetwood, R. D. Schrimpf, W. J. Schaff, and L. J. Brillson, "Electrical, spectral, and chemical properties of 1.8 MeV proton irradiated AlGaN/GaN HEMT structures as a function of proton fluence," *IEEE Transactions on Nuclear Science*, vol. 50, no. 6, pp. 1934–1941, 2003. [Online]. Available: http://dx.doi.org/10.1109/TNS.2003.821827

[68] A. I. Titov, P. A. Karasev, and S. O. Kucheyev, "A model of electrical isolation in GaN and ZnO bombarded with light ions," *Semiconductors*, vol. 38, no. 10, pp. 1179–1186, Oct 2004. [Online]. Available: https://doi.org/10.1134/1.1808825

[69] S. O. Kucheyev, H. Boudinov, J. S. Williams, C. Jagadish, and G. Li, "Effect of irradiation temperature and ion flux on electrical isolation of GaN," *Journal of Applied Physics*, vol. 91, no. 7, pp. 4117–4120, 2002. [Online]. Available: http://dx.doi.org/10.1063/1.1455154

[70] R. Koester, J. S. Hwang, C. Durand, D. L. S. Dang, and J. Eymery, "Self-assembled growth of catalyst-free GaN wires by metal–organic vapour phase epitaxy," *Nanotechnology*, vol. 21, no. 1, p. 015602, 2010. [Online]. Available: http://dx.doi.org/10.1088/0957-4484/21/1/015602

[71] J. L. Zilko, "4 - metal organic chemical vapor deposition: Technology and equipment," in *Handbook of Thin Film Deposition Processes and Techniques (Second Edition)*, second edition ed., K. Seshan, Ed. Norwich, NY: William Andrew Publishing, 2001, pp. 151 – 203. [Online]. Available: https://doi.org/10.1016/B978-081551442-8.50009-2

[72] *B1500A Semiconductor Device Analyzer*, Keysight Technologies, June 2017.

[73] M. Brinza, J. Willekens, M. Benkhedir, and G. Adriaenssens, *Photoconductivity in Materials Research*. Boston, MA: Springer US, 2007, pp. 137–146. [Online]. Available: https://doi.org/10.1007/978-0-387-29185-7_7

[74] L. Alves, M. Breese, E. Alves, A. Paúl, M. da Silva, M. da Silva, and J. Soares, "Micron-scale analysis of SiC/SiC_f composites using the new lisbon nuclear microprobe," *Nuclear Instruments and Methods in Physics Research Section B: Beam Interactions with Materials and Atoms*, vol. 161, pp. 334 – 338, 2000. [Online]. Available: http://dx.doi.org/10.1016/S0168-583X(99)00768-5

[75] J. F. Ziegler, J. P. Biersack, and U. Littmark, Eds., *The Stopping and Range of Ion in Solids*. New York: Pergamon, 1985.

[76] P. Tchoulfian, F. Donatini, F. Levy, B. Amstatt, P. Ferret, and J. Pernot, "High conductivity in Si-doped GaN wires," *Applied Physics Letters*, vol. 102, no. 12, p. 122116, 2013. [Online]. Available: http://dx.doi.org/10.1063/1.4799167

[77] T. Kim, M. C. Yoo, and T. Kim, “Cr/Ni/Au ohmic contacts to the moderately doped p- and n-GaN,” *MRS Proceedings*, vol. 449, 1996. [Online]. Available: https://doi.org/10.1557/PROC-449-1061

[78] Y. Liu, Z. Y. Zhang, Y. F. Hu, C. H. Jin, and L.-M. Peng, “Quantitative fitting of nonlinear Current-Voltage curves and parameter retrieval of semiconducting nanowire, nanotube and nanoribbon devices,” *Journal of Nanoscience and Nanotechnology*, vol. 8, no. 1, pp. 252–258, 2008. [Online]. Available: http://doi.org/10.1166/jnn.2008.N04

[79] Z. Zhang, K. Yao, Y. Liu, C. Jin, X. Liang, Q. Chen, and L.-M. Peng, “Quantitative analysis of Current–Voltage characteristics of semiconducting nanowires: Decoupling of contact effects,” *Advanced Functional Materials*, vol. 17, no. 14, pp. 2478–2489, 2007. [Online]. Available: http://dx.doi.org/10.1002/adfm.200600475

[80] J. Tauc, “Optical properties and electronic structure of amorphous Ge and Si,” *Materials Research Bulletin*, vol. 3, no. 1, pp. 37 – 46, 1968. [Online]. Available: http://doi.org/10.1016/0025-5408(68)90023-8

[81] A. Castaldini, A. Cavallini, and L. Polenta, “Radiation-induced effects in GaN by photoconductivity analysis,” *physica status solidi (a)*, vol. 202, no. 15, pp. 2912–2919, 2005. [Online]. Available: http://dx.doi.org/10.1002/pssa.200521110

[82] T. Suski, P. Perlin, H. Teisseyre, M. Leszczyński, I. Grzegory, J. Jun, M. Boćkowski, S. Porowski, and T. D. Moustakas, “Mechanism of yellow luminescence in GaN,” *Applied Physics Letters*, vol. 67, no. 15, pp. 2188–2190, 1995. [Online]. Available: http://dx.doi.org/10.1063/1.115098

[83] D. Redfield and M. A. Afromowitz, “The direct absorption edge in covalent solids,” *Applied Physics Letters*, vol. 11, no. 4, pp. 138–140, 1967. [Online]. Available: http://dx.doi.org/10.1063/1.1755067

[84] T. S. Moss, “The interpretation of the properties of indium antimonide,” *Proceedings of the Physical Society. Section B*, vol. 67, no. 10, p. 775, 1954. [Online]. Available: http://doi.org/10.1088/0370-1301/67/10/306

[85] E. Burstein, “Anomalous optical absorption limit in InSb,” *Phys. Rev.*, vol. 93, pp. 632–633, Feb 1954. [Online]. Available: https://doi.org/10.1103/PhysRev.93.632

[86] A. Walsh, J. L. F. Da Silva, and S.-H. Wei, “Origins of band-gap renormalization in degenerately doped semiconductors,” *Phys. Rev. B*, vol. 78, p. 075211, Aug 2008. [Online]. Available: https://doi.org/10.1103/PhysRevB.78.075211

[87] M. Feneberg, S. Osterburg, K. Lange, C. Lidig, B. Garke, R. Goldhahn, E. Richter, C. Netzel, M. D. Neumann, N. Esser, S. Fritze, H. Witte, J. Bläsing, A. Dadgar, and A. Krost,

"Band gap renormalization and Burstein-Moss effect in silicon- and germanium-doped wurtzite GaN up to $10^{20}\mathrm{cm}^{-3}$," *Phys. Rev. B*, vol. 90, p. 075203, Aug 2014. [Online]. Available: https://doi.org/10.1103/PhysRevB.90.075203

[88] J. Schörmann, P. Hille, M. Schäfer, J. Müßener, P. Becker, P. J. Klar, M. Kleine-Boymann, M. Rohnke, M. de la Mata, J. Arbiol, D. M. Hofmann, J. Teubert, and M. Eickhoff, "Germanium doping of self-assembled GaN nanowires grown by plasma-assisted molecular beam epitaxy," *Journal of Applied Physics*, vol. 114, no. 10, p. 103505, 2013. [Online]. Available: http://dx.doi.org/10.1063/1.4820264

[89] T. Richter, H. L. R. Meijers, R. Calarco, and M. Marso, "Doping concentration of GaN nanowires determined by opto-electrical measurements," *Nano Letters*, vol. 8, no. 9, pp. 3056–3059, 2008, pMID: 18687013. [Online]. Available: http://dx.doi.org/10.1021/nl8014395

[90] L. Rigutti, M. Tchernycheva, A. De Luna Bugallo, G. Jacopin, F. H. Julien, L. F. Zagonel, K. March, O. Stephan, M. Kociak, and R. Songmuang, "Ultraviolet photodetector based on GaN/AlN quantum disks in a single nanowire," *Nano Letters*, vol. 10, no. 8, pp. 2939–2943, 2010, pMID: 20617803. [Online]. Available: http://dx.doi.org/10.1021/nl1010977

[91] C. H. Qiu and J. I. Pankove, "Deep levels and persistent photoconductivity in GaN thin films," *Applied Physics Letters*, vol. 70, no. 15, pp. 1983–1985, 1997. [Online]. Available: http://dx.doi.org/10.1063/1.118799

[92] W. Y. Weng, T. J. Hsueh, S. J. Chang, S. B. Wang, H. T. Hsueh, and G. J. Huang, "A high-responsivity GaN nanowire UV photodetector," *IEEE Journal of Selected Topics in Quantum Electronics*, vol. 17, no. 4, pp. 996–1001, July 2011. [Online]. Available: http://doi.org/10.1109/JSTQE.2010.2060715

[93] M. Kočan, A. Rizzi, H. Lüth, S. Keller, and U. Mishra, "Surface potential at as-grown GaN(0001) MBE layers," *physica status solidi (b)*, vol. 234, no. 3, pp. 773–777, 2002. [Online]. Available: http://dx.doi.org/10.1002/1521-3951(200212)234:3⟨773::AID-PSSB773⟩3.0.CO;2-0

[94] H. M. Chen, Y. F. Chen, M. C. Lee, and M. S. Feng, "Persistent photoconductivity in n-type GaN," *Journal of Applied Physics*, vol. 82, no. 2, pp. 899–901, 1997. [Online]. Available: http://dx.doi.org/10.1063/1.365859

[95] J. Z. Li, J. Y. Lin, H. X. Jiang, M. A. Khan, and Q. Chen, "Persistent photoconductivity in a two-dimensional electron gas system formed by an AlGaN/GaN heterostructure," *Journal of Applied Physics*, vol. 82, no. 3, pp. 1227–1230, 1997. [Online]. Available: http://dx.doi.org/10.1063/1.365893

[96] V. V. Ursaki, I. M. Tiginyanu, P. C. Ricci, A. Anedda, S. Hubbard, and D. Pavlidis, "Persistent photoconductivity and optical quenching of photocurrent in GaN layers under dual excitation," *Journal of Applied Physics*, vol. 94, no. 6, pp. 3875–3882, 2003. [Online]. Available: http://dx.doi.org/10.1063/1.1604950

[97] R. S. Chen, H. Y. Tsai, Y. S. Huang, Y. T. Chen, L. C. Chen, and K. H. Chen, "Photoconduction efficiencies and dynamics in GaN nanowires grown by chemical vapor deposition and molecular beam epitaxy: A comparison study," *Applied Physics Letters*, vol. 101, no. 11, p. 113109, 2012. [Online]. Available: http://dx.doi.org/10.1063/1.4752230

[98] J. Z. Li, J. Y. Lin, H. X. Jiang, A. Salvador, A. Botchkarev, and H. Morkoc, "Nature of Mg impurities in GaN," *Applied Physics Letters*, vol. 69, no. 10, pp. 1474–1476, 1996. [Online]. Available: http://dx.doi.org/10.1063/1.116912

[99] G. Beadie, W. S. Rabinovich, A. E. Wickenden, D. D. Koleske, S. C. Binari, and J. A. F. Jr., "Persistent photoconductivity in n-type GaN," *Applied Physics Letters*, vol. 71, no. 8, pp. 1092–1094, 1997. [Online]. Available: http://dx.doi.org/10.1063/1.119924

[100] C. Johnson, J. Y. Lin, H. X. Jiang, M. A. Khan, and C. J. Sun, "Metastability and persistent photoconductivity in Mg-doped p-type GaN," *Applied Physics Letters*, vol. 68, no. 13, pp. 1808–1810, 1996. [Online]. Available: http://dx.doi.org/10.1063/1.116020

[101] D. J. Chadi and K. J. Chang, "Theory of the atomic and electronic structure of DX centers in GaAs and $Al_xGa_{1-x}As$ alloys," *Phys. Rev. Lett.*, vol. 61, pp. 873–876, Aug 1988. [Online]. Available: https://doi.org/10.1103/PhysRevLett.61.873

[102] D. V. Lang and R. A. LoGaN, "Large-lattice-relaxation model for persistent photoconductivity in compound semiconductors," *Phys. Rev. Lett.*, vol. 39, pp. 635–639, Sep 1977. [Online]. Available: https://doi.org/10.1103/PhysRevLett.39.635

[103] H. J. Queisser and D. E. Theodorou, "Decay kinetics of persistent photoconductivity in semiconductors," *Phys. Rev. B*, vol. 33, pp. 4027–4033, Mar 1986. [Online]. Available: https://doi.org/10.1103/PhysRevB.33.4027

[104] W. Rieger, R. Dimitrov, D. Brunner, E. Rohrer, O. Ambacher, and M. Stutzmann, "Defect-related optical transitions in GaN," *Phys. Rev. B*, vol. 54, pp. 17 596–17 602, Dec 1996. [Online]. Available: https://doi.org/10.1103/PhysRevB.54.17596

[105] A. P. Karmarkar, B. Jun, D. M. Fleetwood, R. D. Schrimpf, R. A. Weller, B. D. White, L. J. Brillson, and U. K. Mishra, "Proton irradiation effects on GaN-based high electron-mobility transistors with

Si-doped $Al_xGa_{1-x}N$ and thick GaN cap layers," *IEEE Transactions on Nuclear Science*, vol. 51, no. 6, pp. 3801–3806, Dec 2004. [Online]. Available: https://doi.org/10.1109/TNS.2004.839199

[106] X. Hu, A. P. Karmarkar, B. Jun, D. M. Fleetwood, R. D. Schrimpf, R. D. Geil, R. A. Weller, B. D. White, M. Bataiev, L. J. Brillson, and U. K. Mishra, "Proton-irradiation effects on AlGaN/AlN/GaN high electron mobility transistors," *IEEE Transactions on Nuclear Science*, vol. 50, no. 6, pp. 1791–1796, Dec 2003. [Online]. Available: https://doi.org/10.1109/TNS.2003.820792

[107] A. Ionascut-Nedelcescu, C. Carlone, A. Houdayer, H. J. von Bardeleben, J. L. Cantin, and S. Raymond, "Radiation hardness of gallium nitride," *IEEE Transactions on Nuclear Science*, vol. 49, no. 6, pp. 2733–2738, Dec 2002. [Online]. Available: https://doi.org/10.1109/TNS.2002.805363

A

Runsheet

Runsheet for the fabrication of radiation detectors based on GaN microwires

Responsible: Dirkjan Verheij

Process start: 08/03/2017

Process Finish: 29/03/2017

Step 1. Substrate preparation	Date: 08/03/2017

1.1 - **Substrate:** Silicon

Dimensions: x = 34 mm; y = 32 mm;

Thickness: 700μm

1.2 - **Procedure**

Clean substrate with acetone, rinse with water and dry with compressed air.

Step 2. TiW deposition	Date: 08/03/2017

2.1 - **Substrate:** Silicon

2.2 - **Equipment:** Nordiko 7000 (clean-room)

Metalization sequence: TiW 150 no etch

2.3 - **Conditions:**

Module	Power	Voltage	Current	Ar/N_2 flux	Pressure	Dep. rate
3 - DC PVD	0.5 kW	418 V	1.2 A	50/10 sccm	3 mTorr	5.5 Å/s

Step 3. Photolithography	Date: 10/03/2017

3.1 - **Substrate:** Silicon with 150 Å of TiW

3.2 - **Equipment and conditions:**

3.2.1 - **Vapour prime** (30 min, vapour prime oven)

Step 1. Heating at 130℃ in vacuum (10 Torr)

Step 2. HDMS spraying (5 min)

Step 3. Purge prime exhaust (5 min)

Step 4. Return to atmospheric pressure (3min)

3.2.2 - **Coating of PR** (SVG track - recipe 6/2)

Step 1. Dispense PR on the sample and spinning 800 rpm for 5 seconds

Step 2. Spin 2500 rpm for 30 seconds to obtain 1.45 μm thickness

Step 3. Soft bake 85˚C for 60 seconds

3.2.3 - **Exposure** (DWL 2.0)

Map: NWsensor Mask: NWsensor002 Number of dies: 9

AutoCAD drawing

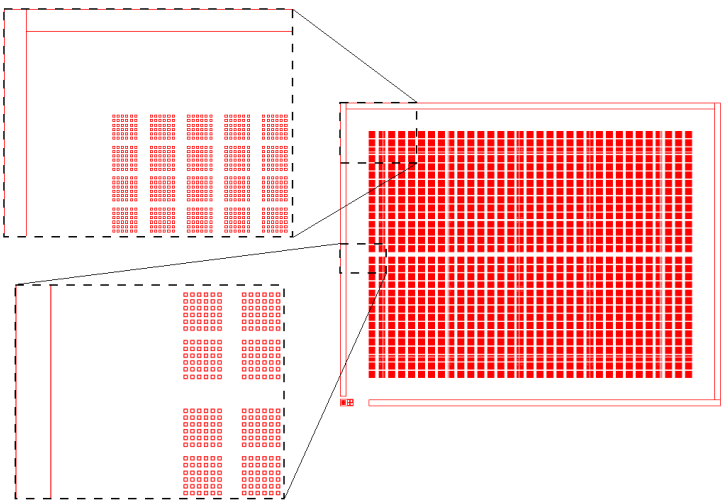

Conditions

Energy	Laser power	Focus
60 %	90 mW	35

3.2.4 - **Development** (SVG track 2 - recipe 6/2)

Step 1. Bake 110˚C for 60 seconds

Step 2. Cool for 30 seconds

Step 3. Developer for 60 seconds

Step 4. Metal etching - IBD etching	Date: 10/03/2017

4.1 - **Substrate:** Silicon with 150Å of TiW and 1.4μm of PR

4.2 - **Equipment:** Nordiko 3600 (clean-room)

4.3 - **Conditions:**

RF power	$Grid_1$ voltage	$Grid_1$ current	$Grid_2$ voltage	Ar flow	Etching time
192 W	724.3 V	104.3 mA	344.8 V	11.2 sccm	200 s

Step 5. PR strip	Date: 13/03/2017

5.1 - **Substrate:** Silicon with 150Å of TiW and 1.4μm of PR (after etching)

5.2 - **Equipment:** Wet bench (outside clean-room)

5.3 - **Conditions:**

Solvent	Temperature	Time
Microstrip	60˚C	4 hours

Step 6. SiO_2 deposition	Date: 13/03/2017

6.1 - **Substrate:** Silicon with a 150Å thick TiW grid

6.2 - **Equipment:** Alcatel (grey room)

6.3 - **Conditions:**

RF power	Pressure	Ar flow	Deposition rate
190 W	4.0 mTorr	20 sccm	11.97 Å/min

Step 7. GaN microwire dispersion	Date: 15/03/2017

7.1 - **Substrate:** Silicon with a 150Å thick TiW grid and 2000 Å of SiO_2

7.2 - **Procedure:**

Step 1. Immersion of a small piece of substrate with microwires into IPA

Step 2. Ultrasound treatment for 30 minutes

Step 3. Deposition of small droplets of the microwire solution onto the substrate

Step 4. Definition of the coordinates of good MWs for devices

Step 8. Photolithography	Date: 17/03/2017

8.1 - **Substrate:** Silicon with 150 Å of TiW, 2000 Å SiO_2 and GaN MWs

8.2 - **Equipment and conditions:**

8.2.1 - **Vapour prime** (30 min, vapour prime oven)

Step 1. Heating at 130℃ in vacuum (10 Torr)

Step 2. HDMS spraying (5 min)

Step 3. Purge prime exhaust (5 min)

Step 4. Return to atmospheric pressure (3min)

8.2.2 - **Coating of PR** (SVG track - recipe 6/2)

Step 1. Dispense PR on the sample and spinning 800 rpm for 5 seconds

Step 2. Spin 2500 rpm for 30 seconds to obtain 1.45 μm thickness

Step 3. Soft bake 85˘C for 60 seconds

8.2.3. **Pre-development** (SVG track 2 - recipe 2 for 20 seconds)

8.2.4 - **Exposure** (DWL 2.0)

Map: NWsensor Mask: NWsensorC1, NWsensorC2, NWsensorC3

Number of dies: 3

AutoCAD drawing

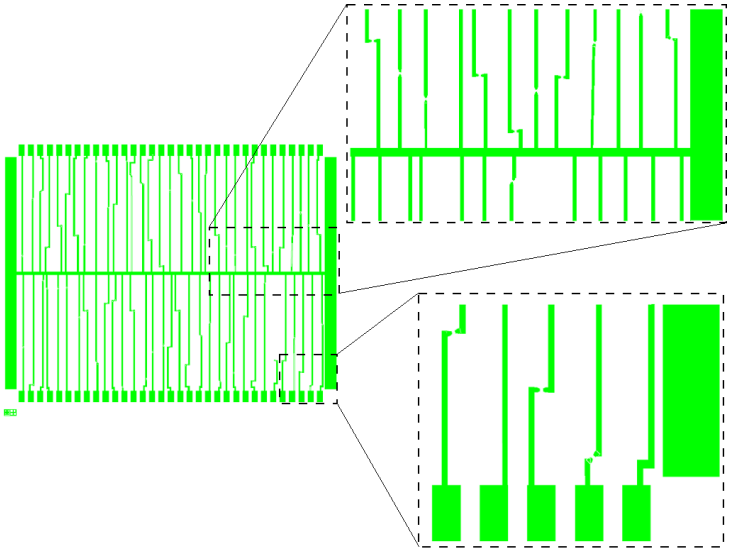

Conditions

Energy	Laser power	Focus
80 %	85 mW	70

8.2.5 - **Development** (SVG track 2 - recipe 6/2)

Step 1. Bake 110˘C for 60 seconds

Step 2. Cool for 30 seconds

Step 3. Developer for 60 seconds

Step 9. Contact deposition - Cr/Au	Date: 20/03/2017

9.1 - **Substrate:** Silicon with 150 Å of TiW, 2000 Å SiO_2, GaN MWs and PR

9.2 - **Equipment:** Alcatel (grey room)

9.3 - **Conditions:**

RF power	**Pressure**	**Ar flow**	**Deposition rate**
20 W	3.0 mTorr	20 sccm	55.6 Å/min

Step 10. Metal lift-off	Date: 22/03/2017

10.1 - **Substrate:** Silicon with 150 Å of TiW, 2000 Å SiO_2, GaN MWs and Cr/Au

10.2 - **Equipment:** Chemical workbench

10.3 - **Conditions:**

Solvent	Temperature	Time
Microstrip	60˚C	4 hours and 30 minutes

Step 11. Chip dicing and wire bonding	Date: 29/03/2017

11.1 - **Substrate:** Silicon with 150 Å of TiW, 2000 Å SiO_2, GaN MWs and Cr/Au contacts

11.2 - **Equipment:** Disco DAD 321 (dicing) and K&S 4526 Manual Bonding System (wire bonding)

B

Summary of the results for samples 210U, 216U and 229U

			Before irradiation	During irradiation	After irradiation
210U	R_{dark} (kΩ)		1.261 ± 0.003	-	11.91 ± 0.06
	$R_{uv_{led}}$ (kΩ)		1.189 ± 0.002	-	10.14 ± 0.05
	Δ_I (%)	bias = 3.5 V	6.69	-	17.15
		bias = -1.5 V	30.56	-	7.89
		bias = -5 V	0.81	-	10.28
216U	R_{dark} (kΩ)		2.28 ± 0.01	14.5 ± 0.5	22.1 ± 0.2
	$R_{uv_{led}}/R_{rad}$ (kΩ)		1.876 ± 0.005	11.5 ± 0.4	14.6 ± 0.2
	Δ_I (%)	bias = 3.5 V	20.73	23.41	51.52
		bias = -1.5 V	4.79	41.94	20.69
		bias = -5 V	-13.82	2.78	40.36
229U	R_{dark} (kΩ)		1.689 ± 0.006	-	16.3 ± 0.4
	$R_{uv_{led}}$ (kΩ)		1.535 ± 0.005	-	15.3 ± 0.3
	Δ_I (%)	bias = 3.5 V	14.26	-	25.21
		bias = -1.5 V	13.20	-	28.57
		bias = -5 V	10.82	-	10.37

Table B.1: Obtained resistances and current gain factors for three devices (210U, 216U and 229U) under different irradiation situations. Note that, for sample 216U, the excitation before and after the irradiation was done with the UV led source, while during the irradiation the protons are responsible for the generation of excess electrons. $R_{uv_{led}}$ corresponds thus to the former two while R_{rad} corresponds to the latter.

		Before irradiation	During irradiation		After irradiation
210U	I_{dark} (μA)	1497.23 ± 0.01	-		31.59 ± 0.02
	I_{uv} (μA)	1601.8 ± 0.3	-		24.930 ± 0.002
	τ_D (s)	0.61 ± 0.01	-		6.6 ± 0.1
	β	0.1828 ± 0.0004	-		0.1515 ± 0.0004
	Δ_I (%)	6.53 ± 0.02	-		26.71 ± 0.08
216U	I_{dark} (μA)	872.6 ± 0.1	-		145.23 ± 0.02
	I_{uv} (μA)	1121.1 ± 0.5	-		96.4 ± 0.3
	τ_D (s)	0.88 ± 0.01	-		0.55 ± 0.02
	β	0.1510 ± 0.0004	-		0.1591 ± 0.0009
	Δ_I (%)	22.17 ± 0.04	-		50.7 ± 0.5
			Short pulse	Long pulse	
229U	I_{dark} (μA)	1199.9 ± 0.1	39.76 ± 0.03	25.30 ± 0.02	-
	I_{uv}/I_{rad} (μA)	1368.8 ± 0.2	30.451 ± 0.002	20.869 ± 0.006	-
	τ_D (s)	3.97 ± 0.02	0.628 ± 0.009	2.55 ± 0.04	-
	β	0.2117 ± 0.0002	0.2293 ± 0.0008	0.296 ± 0.002	-
	Δ_I (%)	12.34 ± 0.01	30.6 ± 0.1	21.2 ± 0.1	-

Table B.2: Obtained fit parameters from transient I-V measurements for three devices (210U, 216U and 229U) under different irradiation situations. Note that, for sample 229U, the excitation source before the irradiation is the UV led while during the irradiation the protons are responsible for the generation of excess electrons. I_{uv} corresponds thus to the former while I_{rad} corresponds to the latter.